Nonlinear Lumped-Parameter Model of the Lumbar Intervertebral Disc: A Study on Viscoelastic Deformation and Three-Dimensional Modeling of the Spine

Kevin Michael Groth

Thesis submitted to the faculty of

Virginia Polytechnic Institute and State University

in partial fulfillment of the requirements for the degree of

Master of Science

In

Mechanical Engineering

Kevin P. Granata, Ph.D., Chair
Stefan Duma, Ph.D., Co-Chair
Moshe Solomonow, Ph.D., M.D.
Mary Kasarda, Ph.D.
Clay Gabler, Ph.D.

August 1, 2007

Blacksburg, Virginia

Keywords: ***Intervertebral Disc, Lumbar, Spine, Lumped-Parameter, Model, Nonlinear, Cyclic, Relaxation, Three-dimensional, Axial, Standard Model.***

Nonlinear Lumped-Parameter Model of the Lumbar Intervertebral Disc: A Study on Viscoelastic Deformation and Three-Dimensional Modeling of the Spine

Kevin Michael Groth

Abstract

Due to the mathematical complexity of current musculoskeletal spine models, there is a need for computationally-efficient models of the intervertebral disc (IVD). The aim of this study is to develop a mathematical model that will adequately describe the motion of the IVD under axial cyclic loading and three-dimensional quasi-static loading as well as maintain computational efficiency for use in future musculoskeletal spine models.

A viscoelastic standard nonlinear solid (SNS) model is introduced within this study. It was developed to predict the axial response of the human lumbar IVD subjected to low-frequency vibration. Nonlinear axial behavior of the SNS model was simulated by a strain-dependent elastic modulus on the standard linear solid (SLS) model.

The SNS model was able to predict the dynamic modulus of the IVD for frequencies of 0.01, 0.1, and 1 Hz. Furthermore, the model was able to quantitatively predict the load relaxation at a frequency of 0.01 Hz. However, model performance was unsatisfactory when predicting load relaxation and hysteresis at higher frequencies (0.1 Hz and 1 Hz). Results suggest that the standard solid model may require strain-dependent elastic and viscous behavior to represent the dynamic response to compressive strain.

The SNS model was expanded to a three-dimensional elastic model by adding a matrix of spring elements in parallel with the SNS model. The geometry and orientation of the added elements represent the regional variations in stiffness and physiologic fiber angle. Results suggest that lordotic posture may be advantageous when modeling the intervertebral joint (IVJ) behavior.

In Memory of

Kevin P. Granata, Ph.D.

Acknowledgments

God

I would like to thank god for granting me my life and providing me with the life experiences that have shaped me into the person that I am today.

My Family

I would like to thank my family for believing in me and supporting all of my efforts.

Dr. Kevin P. Granata

I would like to thank Dr. Kevin P. Granata for giving me an opportunity to demonstrate my will and determination to accomplish my goals. I would also like to thank him for all of his time, patience, and advice that he has provided throughout the years.

My Committee

I would like to thank Dr. Stefan Duma, Dr. Mary Kasarda, and Dr. Clay Gabler for their comments and editorial advice. I would also like to thank Dr. Moshe Solomonow for his professional advice and opinions toward the completion of my thesis.

My Friends

I would like to thank all of my friends outside of and within the field of engineering. They have provided me a social foundation that can not be replaced.

Faculty and Staff of Virginia Tech

I would like to thank all of my instructors at Virginia Tech for giving me a stable platform of knowledge that will continue to benefit me throughout my life and career. I would like to also thank the faculty of the Department of Mechanical Engineering and the Department of Engineering Science and Mechanics for providing me funding throughout my studies in graduate school.

Table of Contents

List of Figures

List of Tables

List of Equations

Nomenclature

Chapter 2

E	=	Modulus of Elasticity
E_1	=	Elastic Modulus of the Spring on the Kelvin Body of the Standard Model
E_2	=	Elastic Modulus of the Series Spring on the Standard Model
S	=	Total Stress
S_d	=	Stress of the Dashpot
S_s	=	Stress of the Spring
$\dot{S}$	=	Stress Rate
e	=	Total Strain
e_d	=	Strain of the Dashpot
e_s	=	Strain of the Spring
$\dot{e}$	=	Strain Rate
μ	=	Coefficient of Viscosity

Chapter 3

A_L	=	Area Under Loading Curve
A_{UL}	=	Area Under Unloading Curve
E_1	=	Elastic Modulus of the Spring on the Kelvin Body of the Standard Model
E_2	=	Elastic Modulus of the Series Spring on the Standard Model
$E(\omega)$	=	Dynamic Modulus
F	=	Axial Force
F_o	=	Initial Axial Force
F_f	=	Final Axial Force
H	=	Intervertebral Disc Height
K	=	Quasi-Static Axial Stiffness or Instantaneous Stiffness
R_i	=	Stress Relaxation Index
S	=	Stress
$\dot{S}$	=	Stress Rate
e	=	Strain
e_o	=	Cyclic Strain Amplitude (One Half Peak-to-Peak Strain)
e_1	=	Strain Required for Initial Preload
$\dot{e}$	=	Strain Rate
t	=	Time
t_o	=	Initial Time
f	=	Frequency
z	=	Axial Displacement
λ	=	Hysteresis Ratio
τ	=	Time Constant
μ	=	Viscosity Coefficient
ω	=	Input or Driving Frequency

Chapter 4

E	=	Modulus of Elasticity
E_{high}	=	High Stress Modulus of Elasticity
E_{low}	=	Low Stress Modulus of Elasticity
F	=	IVJ Loads (6 x 1)
$K(z)$	=	Displacement Dependent Stiffness Matrix (6 x 6)
L	=	Length of Fiber
P	=	Polar Point
X	=	IVJ Displacement (6 x 1)
b_p	=	Perpendicular Distance from the Insertion Point to the Polar Point
dr	=	Disc Bulge
h	=	Disc Height
h_1	=	Initial Disc Height
h_2	=	New Disc Height
i	=	Inferior
l_{10}	=	Initial Fiber Length
l_2	=	New Fiber Length after Calculating for Bulge
l_{20}	=	New Fiber Length before Calculating for Bulge
r_p	=	Intersecting Vector
r_1	=	Initial Radius of Cylinder
r_2	=	New Radius of Cylinder
s	=	Superior
x	=	x-coordinate axis
y	=	y-coordinate axis
z	=	z-coordinate axis
θ	=	Angle Between Polar Point and Insertion Point
α	=	Polar Angle
e	=	Strain
e_o	=	Critical Strain
ϕ	=	Fiber Angle
ψ	=	Curve Parameter

Chapter 1: Introduction

1.1 Motivation and Significance

It has been estimated that as high as 70% of the population experiences low back pain (LBP) during their lifetime (Andersson 1981). Furthermore, LBP has had a significant economic impact on both industry and society (Spengler et al. 1986). While low back pain is most likely multi-factorial in origin, evidence has revealed that there is a strong association with LBP and certain work-related physical factors (i.e. heavy physical work, repetitive lifting, whole body vibration, and static awkward postures) (Bernard 1997; Jensen and Bendix 1992; Kelsey and White 1980; Kittusamy and Buchholz 2004; van Deursen et al. 1999; Wilder et al. 1988). These findings suggest that there is a link between intervertebral joint (IVJ) mechanics and tissue damage leading to LBP. Therefore, it is necessary to research the mechanics of the IVJ when subjected to quasi-static and dynamic loading.

Musculoskeletal spine models have become a very important tool for predicting the mechanics of the human ligamentous spine (Arjmand and Shirazi-Adl 2006; Franklin and Granata 2006; Kiefer et al. 1997; Shirazi-Adl and Parnianpour 1993; Shirazi-Adl and Parnianpour 1996). However, due to the mathematical complexity of the active components of these models, there is a need for more computationally-efficient models of the intervertebral disc (IVD) and IVJ (Kiefer et al. 1997; Shirazi-Adi and Parnianpour 1996; Shirazi-Adl and Parnianpour 1993). The present study addresses this need by improving upon current lumped-parameter models of the IVD and expanding this model to describe three-dimensional behavior of the human lumbar IVJ.

This study is an initial attempt at modeling a very complex joint. As a result, this study is limited to the tissues and conditions discussed within. Continuation of this work will add more toward an overall description of the dynamic and three-dimensional behavior of the spine.

1.2 Hypotheses

1) Can a SNS model be developed and used to predict the viscoelastic response of the IVJ subjected to prolonged axial loading and to low-frequency vibration?

2) Can a three-dimensional lumped-parameter model of the IVD be used to describe the elastic three-dimensional behavior of the IVJ?

1.3 Specific Aims

1) Development of a dynamic lumped-parameter IVD model to study axial cyclic stress relaxation. Specifically,

    a) Is the model able to predict the cyclic stress relaxation?
    b) Is the model able to predict the dynamic modulus?

c) Is the model able to predict the hysteresis?

2) Development of a three-dimensional lumped-parameter model to study elastic behavior of the IVD. Specifically,

   a) Can the model describe the external forces caused by quasi-static IVJ tissue deformation?
   b) Does physiologic posture better model the external forces caused by IVJ tissue deformation?

Chapter 2: Literature and Review

2.1 Function and Anatomy

The spine is a complex network of bone, cartilage and muscles. The primary function of the spine is to protect the spinal cord, transfer loads and stabilize the torso. (Keller et al. 1987). The following sections detail the functional anatomy of the vertebral column.

2.1.1 Regions of the Spinal Column. The spinal column is divided into five distinct regions which include the cervical, thoracic, lumbar, sacral and coccygeal (Fig. 2.1.1). The cervical region, or neck, of the spine has seven vertebrae (C1-C7) that extend from the superior end of the thoracic region to the inferior portion of the head. The thoracic region, or upper back, has twelve vertebrae (T1-T12) that extend from the superior portion of the lumbar region to the inferior portion of the cervical region. The lumbar region, or lower back, has five vertebrae (L1-L5) that extend from the sacrum to the inferior portion of the thoracic region. The sacrum and coccyx are at the most distal regions of the spine (Martini 2004). The lumbar region is the primary focus of the research presented in this paper.

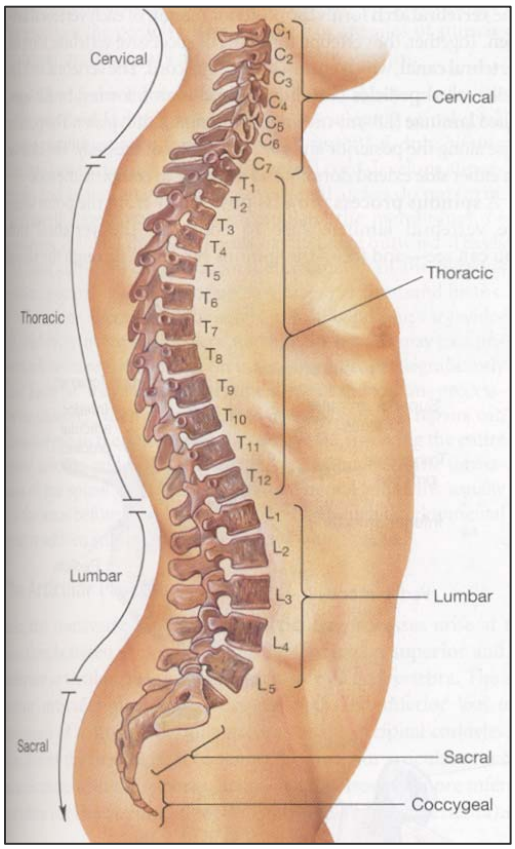

Figure 2.1.1. Five regions of the vertebral column. These regions are the cervical, thoracic, lumbar, sacral, and coccygeal regions (Martini 2004).

2.1.2 Intervertebral Joint. The intervertebral joint (IVJ) is composed of an intervertebral disc (IVD) sandwiched between two adjacent vertebrae. The IVD is composed of a gelatinous core called the nucleus pulposus and a tough outer layer of fibrocartilage called the annulus fibrosus (Fig. 2.1.2). In addition to the IVD, many ligaments attach and bind the adjacent vertebrae to help stabilize the joint. The anterior and posterior longitudinal ligaments respectively connect the anterior and posterior surfaces of the adjacent vertebral bodies. The ligamentum flavum connects the laminae of adjacent vertebrae (Martini 2004) and the capsular ligament connects the apophyseal joint of adjacent vertebra (Adams et al. 1980). The interspinous and supraspinous ligaments are the connecting ligaments of the spinous process (Martini 2004). At the limit of flexion the interspinous and supraspinous ligaments will sprain first. However, the capsular ligaments and the IVD seem to offer the most resistance to flexion (Adams et al. 1980). Although the ligaments are an important component to the IVD, they have not directly been included in the model presented in this research paper. Future studies should consider inclusion of the ligaments, see Chapter 4 for more details.

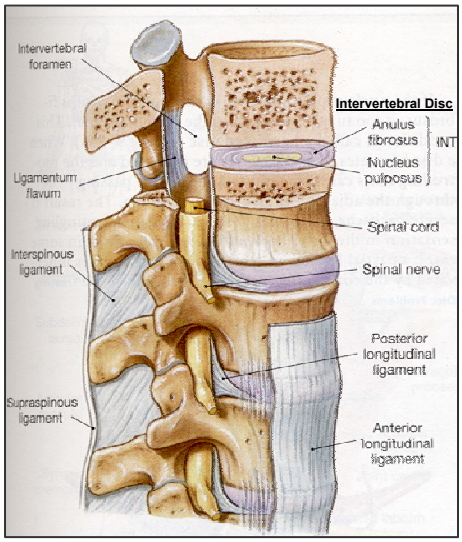

Figure 2.1.2. Intervertebral joint anatomy. The IVJ is composed of an IVD sandwiched between two adjacent vertebrae. Many ligaments interconnect adjacent vertebrae to help stabilize the spine (Martini 2004).

2.1.3 Vertebrae. The vertebra is the bony portion of the IVJ. Each vertebra consists of a vertebral body, posterior processes, and a vertebral foramen (Fig. 2.1.3). The articular processes are connected to the vertebral body by the pedicle and protrude to the posterior portion of the vertebrae. The processes and the pedicle form the vertebral foramen. The adjacent vertebrae and the vertebral foramen create the vertebral canal in which the spinal chord is housed. The inferior and superior articular processes have a smooth concave surface, called the articular facet, and are the contact points of all adjacent vertebrae (Martini 2004). The articular facets joint interaction was not directly included in the model presented in this paper. Future studies should consider the inclusion of the articular facets, see Chapter 4 for more details.

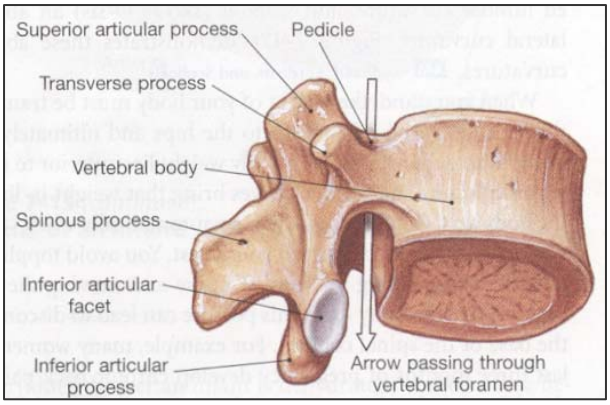

Figure 2.1.3. Vertebra anatomy. The vertebra is the bony portion of the IVJ. It consists of a vertebral body, posterior processes, and a vertebral foramen (Martini 2004).

2.1.4 Intervertebral Disc. The human spinal column contains 23 IVDs (Keller and Nathan 1999). The IVD is connected to the endplates of each adjacent vertebrae of the spine and is composed of a tough fibrocartlidge outer ring called the annulus fibrosus. This ring surrounds and prevents its gel like inner core, the nucleus pulposus, from escaping (Jayson 1987).

Ground substance is the gel like extracellular matrix within the IVD. Ground substance contains mostly water, and attracts water because it contains glycosaminoglycans (a polyanion or highly negatively charged ions). These glycosaminoglycans are then covalently bonded to protein resulting in what is called a proteoglycan. Because the ground substance has a higher concentration of ions within it, the ground substance has a higher osmotic pressure than surrounding body fluids and attracts water from them. Ground substance is very weak in shear because it is mostly made of water. However, ground substance, when contained, allows the tissue to support high compressive loads (Jayson 1987).

The annulus fibrosus encapsulates the nucleus pulposus (Fig. 2.1.4.A). The annulus fibrosus can be thought of as the walls of a pressure vessel and consists of concentric lamellae of highly oriented Type I and Type II collagen fibers. The lamella fibers are diagonally oriented to the transverse plane with a mean fiber angle between 30 and 150 degrees that varies in the circumferential and radial directions (Holzapfel et al. 2005). Furthermore, the lamella fibers in adjacent concentric layers are perpendicularly oriented to one another while lamella within the same layer are parallel (Fig. 2.1.4.B) (Jayson 1987). The water content of the annulus gradually decreases from 80% in the inner lamella to 60% in the outer lamella. However, the collagen content increases from 5% to 30%, respectively. Furthermore, the human annulus contains twice as much Type II collagen as Type I. Nevertheless, the proportion of Type I to Type II collagen increases from the inner lamella to the outer. Moreover, the inner annulus is connected to the cartilage endplates of the vertebrae; however, the outer annulus is connected directly to the bone. In addition to collagen, the IVD contains a small amount of elastin (Jayson 1987).

The nucleus pulposus is a soft, elastic, and gelatinous core encapsulated by the annulus fibrosus. It contains a high percentage of ground substance, giving the IVD some resiliency and allowing it to absorb shock (Martini 2004). Occupying about 30-60% of the cross-sectional area of the IVD (Markolf and Morris 1974; Shirazi-Adl et al. 1984), the nucleus contains randomly dispersed collagen fibrils that very few in number relative to the annulus. Through out the life of the IVD, the nucleus pulposus loses much of it water content, becoming a much more fibrotic tissue (Jayson 1987; Martini 2004). Further evidence has revealed that as the IVD ages it becomes stiffer or less flexible (Iatridis et al. 1997).

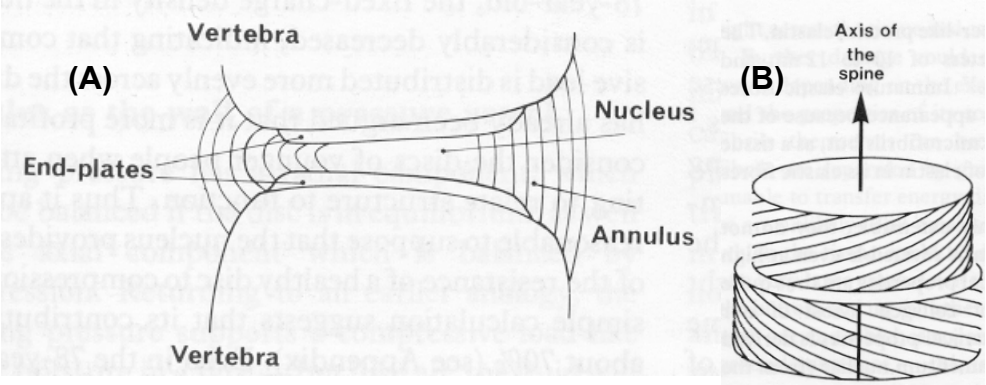

Figure 2.1.4. Intervertebral disc anatomy. (A) The IVD is composed of a tough fibrocartilage ring called the annulus fibrosus and a gel-like inner core called the nucleus pulposus. (B) The lamella fibers are diagonally oriented to the transverse plane. Furthermore, the lamella fibers in adjacent concentric layers are perpendicularly oriented to one another while lamella within the same layer are parrallel (Jayson 1987).

2.2 Motion of the Intervertebral Joint

The IVJ is a six degree of freedom system. Each vertebra is able to translate and rotate about all axes of the body coordinate system (Fig. 2.1.5). These motions are often coupled to one another. In other words, when a body is rotating or translating about one axis, this motion will produce simultaneous rotation or translation about another axis (Jayson 1987). During the rotation of a rigid body there is a hypothetical line called the instantaneous center of rotation (ICR) that does not move. However, because of the coupled motion interaction between rotation and translation the center of rotation changes throughout the motion of the joint (Bogduk et al. 1995; Jayson 1987). Attempts at measuring the ICR of the lumbar spine have been reported (Pearcy and Bogduk 1988; Yoshioka et al. 1990); however, several limitations exist and need to be carefully considered when analyzing ICR measurements (Chen and Katona 1999; Panjabi et al. 1982; Russell et al. 1990).

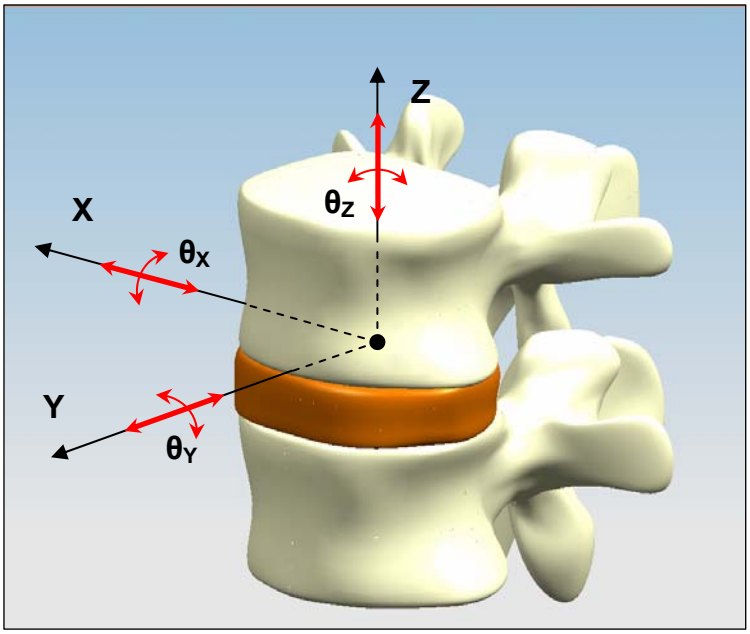

Figure 2.1.5. Body coordinate system of the IVJ. Note that the body coordinate system is defined to be at the superior side and center of each IVD.

2.3 Viscoelastic Properties of the Intervertebral Joint

The IVJ is a viscoelastic material (Jayson 1987) and therefore exhibits creep characteristics under constant stresses, and stress relaxation under constant strains (Martin et al. 1998). Creep within the spine is believed to be caused by the rearrangement of collagen fibers, proteoglycans and water within the IVD, spinal ligaments, and zygapophyseal joint capsules of the IVJ (Oliver and Twomey 1995). However, Koeller *et al.* (1984) proposed that creep of the IVD was mainly due to the stressed annular fibers, and not to fluid flow. A common creep characteristic found in the IVJ during creep testing is an initial increase in stiffness followed by a plateau region or equilibrium state (Keller et al. 1987; Lockett 1972). The increase in stiffness is associated with the nonlinear viscoelastic properties of the IVD (Lockett 1972). Burns *et al.* (1984) noted that the higher magnitudes of the strain observed in lumbar specimens compared to thoracic specimens indicates that the lumbar spine exhibits more creep. Moreover, cyclic axial creep deformation is age dependent; increasing with older specimens (Koeller et al. 1986). Similarly, it has been determined that flexion creep deformation increases with both load and age (Twomey and Taylor 1982). During unloaded recovery, the IVJ will return to its original height as long as it has not reached the elastic limit (Keller et al. 1987). However, hysteresis recovery was shown to have a slower recovery time for older specimens (Twomey and Taylor 1982).

2.4 Viscoelastic Modeling Basics

In traditional viscoelastic mechanics, springs and dashpots are considered to be the building blocks for most viscoelastic structures. Springs account for the elastic behavior of the structure, and dashpots account for the viscous behavior of the structure. For example, when a constant force is applied to a spring and to a dashpot, the spring will undergo a constant deformation and the dashpot will undergo a constant rate of deformation. However, when the force is removed, the spring's deformation is completely recovered; but, the dashpot's deformation is permanent. Recall that the stress-strain relationship for a spring, S_s , and dashpot, S_d , can be described respectively as,

$$S_s = e_s \cdot E \,, \tag{2.1}$$

$$S_d = \dot{e}_d \cdot \mu \,, \tag{2.2}$$

where e is the strain of the spring, E is the modulus of elasticity, μ is the coefficient of viscosity while $\dot{e}$ represent the rate of change of strain with respect to time. By arranging the springs and dashpots in various arrangements, theoretical models can be constructed to describe empirical results (Ozkaya 1991). The following subsections will briefly describe some of the most common arrangements of springs and dashpots and explain their function.

2.4.1 Maxwell Model. The Maxwell model, or viscoelastic fluid element, consists of a dashpot and a spring in series (Ozkaya 1991) (Fig. 2.4.1). When stress, S, is applied during a creep experiment, an instantaneous displacement is seen along the spring. After the initial change in the displacement of the spring, the dashpot begins to deform linearly with time until the force is released. When the force is released the spring returns instantaneously back to its original length; however, the dashpot remains permanently deformed.

When strain, e, is applied during a stress relaxation experiment, initially there is a large stress response caused by the dashpot. As the dashpot begins to deform over time, the stress of the spring relaxes nonlinearly. After the strain is released, the stress continues to decrease until no stress is seen by the system.

Figure 2.4.1. Maxwell model.

The total stress, S , of the Maxwell model is defined by,

$$S = S_d = S_s \,, \tag{2.3}$$

where S_d is the stress of the dashpot and S_s is the stress of the spring. Similarly, we can define the total strain, e , of this system as

$$e = e_d + e_s , \tag{2.4}$$

where e_d is the strain of the dashpot and e_s is the strain of the spring. Substituting these stress and strain relationships into the equation for the total strain of the system, we can describe the overall stress-strain behavior of the Maxwell model with the following differential equation,

$$\dot{e} = \dot{e}_d + \dot{e}_s = \frac{\dot{S}}{E} + \frac{S}{\mu} , \tag{2.5}$$

where E is the modulus of elasticity and μ is the coefficient of viscosity while $\dot{S}$ and $\dot{e}$ represent the rate of change of stress and strain with respect to time.

2.4.2 Kelvin-Voight Model. The Kelvin-Voight (a.k.a. Kelvin Body) model is a two-parameter lumped-parameter model that has been used to describe the behavior of viscoelastic solids such as the IVJ. (Burns et al. 1984; Keller et al. 1987; Lucas et al. 1999; Ozkaya 1991). This model consists of a spring and dashpot in parallel (Fig. 2.4.2). When a constant stress is applied during a creep experiment, the dashpot initially resists the stress; however, as time continues the spring and dashpot begin to deform exponentially with the spring taking a greater share of the load. When the stress is released, the dashpot slows the response of the spring until the system finally reaches equilibrium at its initial length.

When a strain is applied during a stress relaxation experiment, an infinite and instantaneous stress response occurs at the dashpot. Therefore, the Kelvin-Voight model can not realistically describe the stress relaxation response because an infinite stress would be required to overcome the dashpot's infinite resistance (Throne 1988).

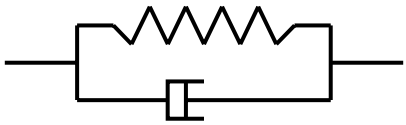

Figure 2.4.2. Kelvin-Voight model.

The total stress, S, of the system is defined by,

$$S = S_s + S_d , \tag{2.6}$$

where S_d is the stress of the dashpot and S_s is the stress of the spring. The total strain, e, of this system is defined by

$$e = e_s = e_d \,, \tag{2.7}$$

where e_d is the strain of the dashpot and e_s is the strain of the spring. The stress-strain relationship of the total system is described by the following differential equation,

$$S_T = e \cdot E + \dot{e} \cdot \mu \,, \tag{2.8}$$

where E is the modulus of elasticity and μ is the coefficient of viscosity while $\dot{e}$ represents the rate of change of strain with respect to time.

2.4.3 Standard Linear Solid Model. The standard linear solid (SLS) model is a three-parameter model that is used to describe many biological materials (Lucas et al. 1999; Ozkaya 1991). The arrangement consists of a Kelvin body in series with a spring (Fig 2.4.3). It has been used extensively to model the creep characteristics of the IVD subjected to axial loads (Burns et al. 1984; Keller and Nathan 1999; Keller et al. 1987; Li 1994; Li et al. 1995). Experimental evidence has revealed that the SLS model is best at representing the creep deformation of the IVD (Burns et al. 1984).

When a stress is applied to this system, there is an instantaneous deformation of the springs. The dashpot and springs then begin to deform as a function of time. As the stress is released, the spring in series returns to initial length while the dashpot slows the spring in parallel until the system reaches equilibrium, at which both springs and the dashpot are returned to their initial lengths.

When strain is applied to the system, the springs and dashpot produce a large instantaneous stress. Over time the dashpot deforms and stress in the system begins to relax. As the strain is released, the spring in series exhibits a large drop off ; however, the dashpot slows the spring in parallel until equilibrium is reached. A more detailed description of the SLS model is provided in Chapter 3.

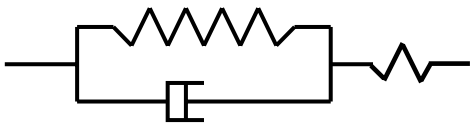

Figure 2.4.3. Standard linear solid (SLS) model.

The stress-strain relationship can be written as,

$$p_1 \dot{S} + S = q_1 \dot{e} + q_0 e \,. \tag{2.9}$$

where S is the stress, e is the strain, while $\dot{S}$ and $\dot{e}$ represent the rate of change of stress and strain with respect to time (Li 1994; Li et al. 1995). Model coefficients can be derived from material properties,

$$p_1 = \frac{\mu}{E_1 + E_2}; \qquad q_1 = \frac{\mu \cdot E_2}{E_1 + E_2}; \qquad q_0 = \frac{E_1 \cdot E_2}{E_1 + E_2} \tag{2.10}$$

where E_1 is the elastic modulus of the Kelvin body, E_2 is the elastic modulus of the spring in series with the Kelvin body, and μ is the viscosity coefficient of the Kelvin body (Li 1994; Li et al. 1995).

2.5 Current Intervertebral Joint and Disc Models

2.5.1 Lumped-Parameter Models. Lumped-parameter models are simplified mathematical models that describe physical systems. The parameters within these models represent all the variables within a material as single scalar values. The following section details lumped-parameter models of the IVJ (Burns et al. 1984; Holmes and Hukins 1996; Kaleps et al. 1984; Keller et al. 1987; Li et al. 1995).

Burns et al. (1984). This study was one of the first investigations into the analytical methods for describing the creep behavior observed in the IVJ. Within this study, 47 human IVDs were subjected to a constant axial compressive stress. Using two (Kelvin-Voight model), three-parameter (SLS model), and four-parameter solid models to describe the creep behavior of the disc, they found that the three-parameter and four-parameters models represented the creep characteristics the best with an average error of 2.314% and 4.446%, respectively. Moreover, it was shown that the three-parameter SLS model was better at predicting the strain behavior for experimental testing times greater than 1 minute, whereas the four-parameter model was better at predicting strain behavior for experimental testing times less than 1 minute. Although the two-parameter model did not perform as well as the three-parameter and four-parameter models, it was suggested that it may be useful for degenerated discs.

Kaleps et al. (1984). As a continuation to the Burn's *et al.* (1984) study, Kaleps *et al.* studied the long term creep response of 54 Rhesus monkey IVDs. Using a two and three-parameter solid model, they confirmed that the two-parameter model does not adequately predict the creep response of normal IVDs. Furthermore, the study quantitatively showed that the three-parameter model demonstrates excellent results in describing compressive creep behavior of a healthy IVJ. The collective average error was only 1.363%.

Keller et al. (1987). In this study the viscoelastic creep behavior of 18 human lumbar motion segments were used to develop a creep model based on the three-parameter SLS model. Material properties for the model were determined using a linearization method based on Taylor series expansion of the strain solution. The SLS model was in good agreement with the experimental data versus the theoretical strain predictions, wherein the average error was less than 1%. In addition, the study found that the older and more degenerated discs had lower material coefficients suggesting that the joints were less stable. No correlation was found between the creep characteristics of the IVJ and disc height, disc area, segmental level, or sex. However, the bone mineral content and the material coefficients correlated very well.

Li et al. (1995). This investigation addressed the limitations of the SLS model when the IVD was subjected to prolonged loading and low-frequency vibration in axial compression. Through this investigations Li *et al.* determined that the SLS model was able to qualitatively simulate the effects of disc level and degeneration on the ability of an IVD to resist long lasting creep and low-frequency vibration. However, the model could not quantitatively predict dissipation of energy or dynamic loads of an IVD subjected to cyclic loading.

Holmes et al. (1996). Within this study load relaxation was measured in 12 human lumbar spine segments. From this data a linear load relaxation model was created out of two Maxwell elements in parallel and fitted to the experimental data. From Fourier transforms of the load relaxation data, Holmes *et al.* was able to deduce that the stiffness of the IVJ increases with frequency. However, there was a gradual loss in the viscous behavior of the IVJ. The overall conclusion from this study was that the IVJ does not function as a shock absorber when loading frequencies are above 1 Hz.

2.5.2 Finite Element Models. Finite element modeling is the most popular method used in spine biomechanics to model the tissue properties, the complex loading, and the geometry of the IVJ (Natarajan et al. 2004). These models have been used extensively to determine the stress and strain placed on the vertebral bodies, IVDs and facet joints of the spine (Argoubi and Shirazi-Adl 1996; Campbell-Kyureghyan 2004; Kasra et al. 1992; Shirazi-Adl 1989; Shirazi-Adl et al. 1986; Shirazi-Adl et al. 1984; Wang et al. 1997; Yang and King 1984). The following section details several common finite element models of the IVJ.

Shirazi et al. (1984). A three-dimensional finite element model of the lumbar (L1-L2) IVD was developed for the purpose of studying the response of the disc to quasi-static compressive forces. The finite element code is based on updated Langrangian formulation and accounts for both geometric and material nonlinearities associated with the IVD. Analysis revealed that the annulus fibers are not subject to rupture during pure compressive loads. The following paragraphs will briefly describe the geometry and material properties associated with this model.

Geometrically, the IVD was based on measurements taken from a lumbar (L2-L3) specimen of a 29-year-old woman. The height of the disc was assumed to be 11.0 mm over the entire cross-sectional area. Lateral and sagittal diameters were measured to be 49.2 mm and 34.0 mm respectively and the cross-sectional area of the disc was 1371 mm^2. The nucleus cross-sectional area was 632 mm^2. Furthermore, the annulus was measured to be 1.2 times thicker in the anterior and lateral regions of the disc compared to the posterior portion of the disc. The posterior surface of the disc was considered to be flat to account for this variation. The annulus fibers were arranged in eight layers and were modeled as axial elements. The elements formed a crisscross pattern to one another with an average angle of 29° to horizontal plane of the disc. Furthermore, a fiber content of 19% was distributed amongst the eight layers. Based on previous literature, the collagen fibers of the annulus were assumed to have a cross-sectional area ratio of 1.0, 0.78, 0.62, and 0.47 from the outer layers to the inner layers, respectively.

The nucleus pulposus was modeled as an incompressible, inviscid fluid, and the annulus fibrosus was modeled as a matrix of collagen fibers embedded in ground substance. The ratios of elastic constant for the fibers were 1.0, 0.90, 0.75, and 0.65 from the outer layers to the inner layers, respectively. Furthermore, the elastic modulus and shear modulus of the ground substance were assumed to be 4.2 MPa and 1.6 MPa, respectively.

Shirazi et al. (1987). Expanding on the previously published three-dimensional finite element model, this study used the model to predict the strain in the disc fibers. Tensile strains of 10% were calculated during maximum symmetric loading. Furthermore, lateral bending and twisting increased the tensile strains to above 20%. The highest strains were seen to occur at the inner most layer of the annulus in the posterolateral region of the IVD.

Natarajan et al. (1999). Within this study, a three-dimensional finite element model was created for the purpose of testing the influence of IVD geometry. Three disc heights (5.5 mm, 8.5 mm, and 10.5 mm) and three disc areas (1060 mm^2, 1512 mm^2, and 1885 mm^2) were used in the analysis. A compressive preload of 400 N was applied while the IVD was subjected to four different moments (flexion, extension, lateral, and torsion) and three forces (axial, anterior and posterior shear). Results indicate that the IVDs with a small disc area to height ratio were more likely to have higher annular stresses, larger disc bulge and larger motions. Furthermore, IVDs are more flexible when disc height increases.

Wang et al. (2000). A viscoelastic finite element model of the L2-L3 motion segment was developed to determine the role of loading rate on the spine. Compressive and shear loads were applied to the top of the vertebrae to simulate flexion movements. Three speeds of flexion were tested (0.3, 1, and 3 second durations). Results indicated that the higher loading rates increased the peak intradiscal pressure, bending moment, total ligament force, and annulus posterolateral stress.

Campbell-Kyureghyan et al. (2004). Campbell-Kyureghan *et al.* understood the need for a more computationally efficient IVD model to study the dynamics of the human ligamentous spine (Campbell-Kyureghyan 2004). The model simulates the large displacements, dynamics, and cyclic flexion bending behavior of the spine. The IVD model consists of two types of elements: truss elements and beam elements. The truss elements represented ligaments and the annulus fibers of the disc. The beam element represented the nucleus. The results indicated that larger forces, creep, and energy dissipation were predicted at the lower segmental levels of the spine. In addition, higher bending velocities and higher bending frequencies contributed to an increase in creep and energy dissipation.

2.5.3 Poroelastic Models. Poroelastic models are a variation in finite element modeling where the fluid flow characteristics are taken into consideration. In recent years, these models have been applied to the IVD (Argoubi and Shirazi-Adl 1996; Cheung et al. 2003; Lee and Teo 2004; Riches et al. 2002; Simon et al. 1985). These models suggest that the loading and stress distribution is dependent on the fluid flow

interaction and deformation of the IVD. The following section details some recent studies in poroelastic modeling of the IVD.

Simon et al. (1985). This study was the first study to model the IVD as a poroelastic structure. The model was developed from rhesus spinal motion segment data and was used to study the creep deformation and impact response of normal and degenerated discs. Results indicate that the fluid phase of the IVD is significantly important in the mechanical response of the IVD. Furthermore, the fluid component's role was quantified and shown to significantly contribute to transient stress concentrations in the cancellous bones of the IVJ.

Argoubi et al. (1996). Within this study, a nonlinear three-dimensional poroelastic IVD model was developed to study creep deformation. Specifically, they studied the role of facets, strain-dependent permeability, boundary pore pressure, and coupled rotations. The geometry of the model was based on a human lumbar (L2-L3) motion segment. The fluid and solid phases were considered to be incompressible. The annulus was modeled as a composite structure made of collagenous fibers and annulus bulk. Results indicated that during creep deformation the axial displacement increases, pore pressure decreases, compressive stress of the annulus bulk increases, fiber layer slacken, and the facet load increases. Furthermore, the strain-dependent permeability and boundary pore pressure increases the stiffness of the IVD.

Riches et al. (2002). A one-dimensional poroelastic model was developed within this study. This model assumes a power-law relationship between porosity and permeability. Furthermore, a linear relationship between the osmotic potential and solidity is included. The model was subjected to 5 cyclic loads of compression for 20 minutes each. Results suggested that a one-dimensional model can approximate the fluid characteristics of the IVD when subjected to cyclic creep deformation.

Cheung et al. (2003). The model developed in this study assumes that the IVD structure (L4-5) is composed of an incompressible porous solid and an incompressible fluid (Cheung et al. 2003). The resulting viscoelastic behavior was modeled using momentum exchange between the permeability dependent porous solid and the fluid phase. The model was subjected to quasi-static and vibrational loading and the response of the fluid flow and stress was analyzed. Results revealed that fluid flow and deformation of the IVD were dependent on the frequency of loading. This suggests that cyclic loading increases the fluid exchange of the IVD.

Lee et al. (2004). A three-dimensional poroelastic finite element model of the lumbar (L2-L3) IVJ was developed to study spinal instabilities. Using this finite element model, a holding task was simulated by loading the joint with a constant compressive load of 1600 N and anterior shear load of 200 N. The role of the facet joints and ligaments were assessed. Results indicated that the facets and ligaments play a major role in resisting anterior shear loads and removal of them would have adverse effects on spinal stability causing further disc degeneration.

2.5.4 Stability Models. There are few papers that have modeled intrinsic mechanical stability of the IVJ (Crisco and Panjabi 1992; Lucas and Bresler 1961). Current research on stability of the spine has led to the use of complex dynamic multi-segment spine models complete with musculature (Arjmand and Shirazi-Adl 2006; Franklin and Granata 2006; Kiefer et al. 1997). The following section will describe some of these models in detail.

Lucas et al. (1961). This study was the first attempt at modeling the intrinsic stability of the spine. The model assumed that the human thoracolumbar spine devoid of all musculature behaved like a one-dimensional modified elastic rod. Using Euler's theory of buckling, Lucas *et al.* was able to theoretically predict the critical buckling load of the spine in the lateral direction. This model was validated through experimental measurements. The predicted buckling loads ranged from 16.8-25.4 N, while the experimental values ranged from 19.1-25.7 N.

Crisco et al. (1992). The spine was modeled as an Euler column restrained in the coronal plane. A single torsional spring was used to model the elastic lateral flexion behavior observed in the IVD. Stiffness data was obtained from experimental measurements made from cadaveric specimens. A linear and exponential model was used to model the elastic behavior seen in each specimen. The linear model was found to be more stable, predicted a buckling load of 67 N, whereas the exponential model predicted a buckling load of 11 N. Moreover, the greatest buckling motion was predicted at the L5-S1 joint. The linear model predicted the post buckling behavior at 100 N to be 40°, while the exponential model predicted the post buckling motion to less than 5°.

Kiefer et al. (1997). The complete thoracolumbar spine was modeled to help identify the mechanisms that may affect the compressive load bearing capacity in neutral postures. The IVD was modeled as a Timenshenko beam element with transverse shear deformation and an Euler beam element with no transverse shear deformation, while the vertebrae were modeled as rigid bodies. The material properties remained constant for each IVD (Young's Modulus: Lumbar discs, E = 7 MPa; Thoracic Discs, E=35 MPa; and Shear Modulus, G=3 MPa); however, the geometry was varied by segmental level. Musculature was added based on kinematic conditions of the spine.

Arjmand et al. (2006). The complete thoracolumbar spine was modeled as a sagittally symmetric beam and rigid body model complete with musculature. The model was developed to determine muscle forces, spinal loads, and stability margins for isometric forward flexion tasks. The model was similar to Keifer's *et al.* model in that it consisted of six deformable beam elements which represent the IVDs of the lumbar region (T12-S1) and a single body, made up of seven rigid elements, which represents the thoracic region (T1-T12). A gravity load of was eccentrically located at different segmental levels of the spine, while an external load was applied to a rigid element attached to the T3 vertebra for some cases. The muscle model consisted of a total of 56 muscles. Results indicated that the stability increased while in a flexion posture due to greater passive stiffness and extensor muscle activity.

Franklin et al. (2006). A three-dimensional 18 degree of freedom multi-segment dynamic model of the thoracolumbar spine complete with musculature was developed to research reflex gain, co-contraction, and stability of the spine. The model consisted of 6 rigid bodies representing five lumbar vertebrae and one thoracic segment. The IVDs were unique in that they were represented by several Kelvin body models in parallel. The stiffness and damping ratio of the IVDs were assigned a constant value of 50 Nm/rad and 100 s^{-1}, respectively. The muscle model consisted of 90 muscles utilizing a centroid line approach. Results indicated that reflexes allow the spine to stabilize with less antagonistic co-contraction. Furthermore, increased reflex delay and decreased reflex gain requires greater antagonistic co-contraction to maintain spinal stability.

Chapter 3:
The Viscoelastic Standard Nonlinear Solid Model

This chapter presents:

- The development of a novel method to model the axial cyclic relaxation of the human intervertebral disc (IVD) by modifying the standard linear solid (SLS) model to be a nonlinear solid model (SNS model).
- A strain-dependent relationship for the instantaneous modulus, $E_2(e)$, of the IVD which is determined from experimental stiffness data obtained from the literature (Gardner-Morse and Stokes 2004).
- The calibration of the constant parameters (E_1 and μ) for the SNS model based on experimental load relaxation results reported in the literature (Holmes and Hukins 1996).
- A comparative analysis on the SNS model's performance based on experimental data obtained from the literature (Li et al. 1995).

3.1 Introduction

Although the etiology of low back pain (LBP) is not completely understood, evidence has revealed that prolonged static awkward postures (i.e. sitting) may be a contributing factor to LBP (Jensen and Bendix 1992; Kelsey and White 1980; Kittusamy and Buchholz 2004; van Deursen et al. 1999; Wilder et al. 1988). Moreover, studies have suggested that there is an increased risk of LBP when the spine is exposed to seated low frequency (<6 Hz) vibration (e.g. vibration when operating trucks, buses, etc.) (Kelsey and Hardy 1975; Pope et al. 1999; Wilder et al. 1982). These findings suggest that there is a link between intervertebral joint (IVJ) dynamics and tissue damage leading to LBP. Therefore, it is necessary to further research the dynamics of the IVJ when subjected to prolonged loading and low-frequency vibration.

Musculoskeletal spine models have become a very important tool for predicting the mechanics of the human ligamentous spine (Arjmand and Shirazi-Adl 2006; Franklin and Granata 2006; Kiefer et al. 1997; Shirazi-Adi and Parnianpour 1996; Shirazi-Adl and Parnianpour 1993). However, due to the mathematical complexity of these models, there is a need for more computationally-efficient models of the intervertebral disc (IVD) (Kiefer et al. 1997; Shirazi-Adi and Parnianpour 1996; Shirazi-Adl and Parnianpour 1993). The present study addresses this need by improving upon current lumped-parameter models of the IVD.

Several studies have successfully modeled the creep characteristics of the human IVD using the three-parameter viscoelastic standard linear solid (SLS) model (Burns et al. 1984; Keller et al. 1987; Li 1994; Li et al. 1995). Burns *et al*. (Burns et al. 1984) tested several rheological models and concluded that the SLS model best simulates the creep response of the IVD. However, when the model is subjected to low-frequency vibration the model has several limitations. In particular, the model underestimates the

stress relaxation, the dynamic modulus, and the hysteresis of the human lumbar IVD (Li 1994; Li et al. 1995).

The standard nonlinear solid (SNS) model introduced within the present study modifies the SLS model by adding a nonlinear component. It is proposed that modeling the nonlinear mechanical behavior of the human lumbar IVD will better capture the dynamic response of the IVJ under compressive loads. It has been shown that the IVD experiences a nonlinear stress behavior when subjected to axial strain (Berkson et al. 1979; Edwards et al. 1987; Gardner-Morse and Stokes 2004; Markolf 1972; Panjabi et al. 1976; Tencer et al. 1982). The nonlinear behavior is associated with an increase in stiffness as the IVJ is compressed (Gardner-Morse and Stokes 2004). Further experimental evidence reveals that the stiffness of the IVJ increases after cyclic loading (Johannessen et al. 2004). Because the parameters of the SLS model are strain independent, the model cannot account for the nonlinear behavior of the IVD.

The primary goal of the present study is to develop a novel method of modeling the behavior of the IVD using the SNS model (Fig. 3.1.1). A secondary goal is to determine whether the SNS model could be used to predict the response of the IVD subjected to prolonged axial loading and to low-frequency vibration. Specifically, we test whether the SNS model can predict the cyclic stress relaxation, the dynamic modulus, and the hysteresis of a lumbar motion segment using experimental load deformation and stress relaxation curves obtained from the literature (Gardner-Morse and Stokes 2004; Holmes and Hukins 1996).

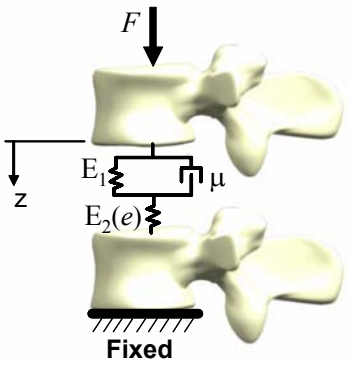

Figure 3.1.1. Standard nonlinear solid (SNS) model. The arrangement of the standard model consists of a Kelvin body in series with a spring. The SNS model in the present study differs from the SLS model in that it replaces the series spring's constant modulus with a strain-dependent modulus.

3.2 Methods

3.2.1 The Standard Nonlinear Solid (SNS) Model. Linear elastic springs (Hooke Body) and linear viscous elements (dashpots or Newton Body) are considered to be the building blocks for most traditional viscoelastic systems. By organizing the springs and dashpots in various arrangements, theoretical models can be constructed to describe empirical results (Ozkaya 1991). The Kelvin (a.k.a. Kelvin-Voight) body is

considered to be one of the simplest arrangements that describes the viscoelastic behavior of the IVD (Keller et al. 1987). The arrangement of the Kelvin body consists of a spring and dashpot in parallel. However, Burns *et al.* (1984) determined that the SLS model is better when representing the creep characteristics of the IVD subjected to a prolonged axial load.

The arrangement of the SLS model consists of a Kelvin body in series with a spring (Fig. 3.1.1). As detailed in Chapter 2, this model can be represented by the following differential equation:

$$p_1\dot{S} + S = q_1\dot{e} + q_0 e \tag{3.1}$$

where S is the IVD stress, e is the IVD strain, while $\dot{S}$ and $\dot{e}$ represent the rate of change of stress and strain with respect to time. Model coefficients are derived from material properties by the following equations,

$$p_1 = \frac{\mu}{E_1 + E_2};\ q_1 = \frac{\mu \cdot E_2}{E_1 + E_2};\ q_0 = \frac{E_1 \cdot E_2}{E_1 + E_2}, \tag{3.2}$$

where E_1 is the elastic modulus of the Kelvin body, E_2 is the elastic modulus of the spring in series with the Kelvin body, and μ is the viscosity coefficient of the Kelvin body (Li 1994; Li et al. 1995). The elastic modulus, E_2, is also known as the instantaneous elastic modulus because during initial loading the IVJ experiences an instantaneous deformation that is proportional to this modulus (Keller et al. 1987).

The SNS model in the present study differs from the SLS model in that it replaces the series spring's constant intantaneous elastic modulus, E_2, with a strain-dependent elastic modulus where the elastic modulus is a linear function of strain, $E_2(e)$. Substituting the strain-dependent modulus, $E_2(e)$, into the model coefficients (Eq. 3.2) of the standard model yields,

$$p_1 = \frac{\mu}{E_1 + E_2(e)};\ q_1 = \frac{\mu \cdot E_2(e)}{E_1 + E_2(e)};\ q_0 = \frac{E_1 \cdot E_2(e)}{E_1 + E_2(e)} \tag{3.3}$$

3.2.2. Strain-Dependent Elastic Modulus of the SNS Model. The strain-dependent elastic modulus of the IVJ was modeled from experimental load deformation data obtained from the literature (Gardner-Morse and Stokes 2004). Gardner-Morse's *et al.* (2004) study was chosen on the basis of being the most comprehensive experimental stiffness data currently available for human lumbar motion segments. Within this study, Gardner-Morse *et al.* recorded the load deformation behavior of eight female human

lumbar motion segments (L2-L3 and L4-L5) under an axial compressive preload of 0, 250, and 500 N. Specimens were subjected to four sawtooth-waveform axial displacements (±0.35 mm) for 87 seconds and a least squares regression routine was used to determine the axial stiffness at each preload (Table 3.2.1). Because the data was recorded over a relatively short time duration, it was assumed that the data represents the instantaneous elastic modulus of the SNS model.

Table 3.2.1. Gardner-Morse *et al*. (2004) reported stiffness coefficients. The * denotes values calculated from reported results. Values in ( ) denotes standard deviation.

Axial Preload, F [N]	Stiffness, K [N/mm]	Strain, e [%]*	Modulus, E_2 [MPa]*
0	438 (92)	0	3.36
250	1700 (67)	1.65	13.03
500	2420 (158)	2.32	18.55

Intervertebral disc geometry was used to normalize the stiffness coefficients and calculated displacements so that they could be reported as elastic moduli and strains, respectively. The average disc height, disc lateral width, and disc anterior-posterior width were reported as 8.9 mm, 45.5 mm and 32.5 mm, respectively. The area of the disc (1161 mm^2) was assumed to be the shape of a simple ellipse.

Once the strains and corresponding elastic moduli were determined, the values were plotted and a linear least squares regression was applied to determine a relationship (Eq. 3.4) that describes how the IVD's intantaneous elastic modulus, E_2, changes with strain, e (Fig. 3.2.1.A).

$$E_2(e) = 641.4\,e + 3.14 \tag{3.4}$$

The strain-dependent instantaneous modulus was used to describe the nonlinear stress behavior of the IVJ (Fig. 3.2.1.B) and the nonlinear stress behavior appears to be similar to other experimental and theoretical studies (Berkson et al. 1979; Lin et al. 1978; Shirazi-Adl et al. 1984; Tencer et al. 1982).

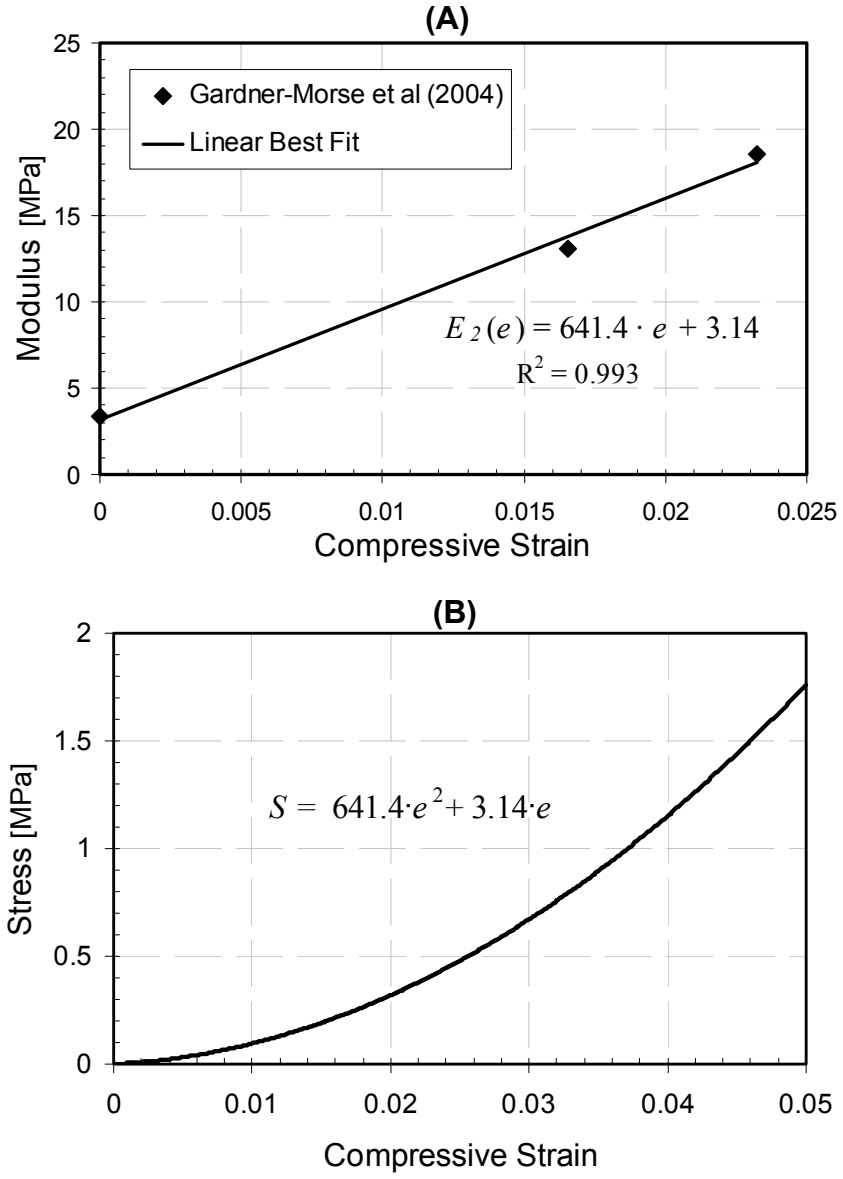

Figure 3.2.1. Instantaneous elastic response of the IVD. (A) Relationship for how the elastic modulus, $E_2(e)$, changes with axial compressive strain, e, was found through a linear least squares regression. (B) The IVD experiences a nonlinear stress when subjected to compressive strain input. The nonlinear stress is due to an increase in stiffness as the IVJ is compressed.

3.2.3 Constant Parameters of the SNS Model. The constant parameters (E_1 and μ) for the Kelvin body of the SNS model (Eqs. 3.1 & 3.3) were calibrated by minimizing the sum of the squared error between the predicted stress (Eq. 3.5) and the experimental results from Holmes's *et al.* (1996) stress relaxation experiment on a male lumbar (L3-L4) motion segment (Fig. 3.2.2). Calibrated parameters are reported in the results section (Table 3.3.1). Predicted stress relaxation was determined by solving the

SLS model (Eqs. 3.1 & 3.2) analytically for relaxation conditions, in which the applied strain, *e*, remained constant and the initial conditions were set as $S(t_o) = S_o$.

$$S = e \cdot q_o + (S_o - e \cdot q_o) \cdot exp(\frac{-t + t_o}{p_1}) \tag{3.5}$$

The constant applied strain, e = 0.0417, was determined by displacing the series spring of the SNS model, (Eq. 3.4), until the initial stress, S_o = 1.25 MPa, was reached (Fig. 3.2.1.B). The applied strain resulted in a constant instantaneous modulus of E_2 = 29.97 MPa. Initial stress, S_o, was determined by normalizing the reported maximum force value (2050 N) on the stress relaxation experiment (Holmes and Hukins 1996) and dividing the value by the area of the disc.

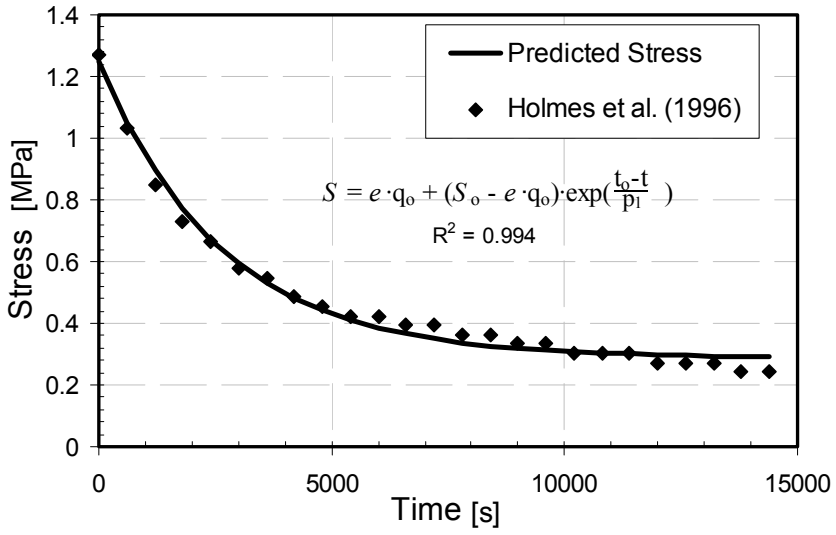

Figure 3.2.2. Stress relaxation of the IVD. The constant parameters ($E_1$and μ) for the Kelvin body of the SNS model were determined by least squares regression with the experimental stress relaxation response of a lumbar IVD. Note that the experimental values used were estimated from graphical results reported within Holmes *et al.* (1996).

3.2.4 Cyclic Deformation of the SNS Model. The SNS model with calibrated parameters (E_1, $E_2(e)$, and μ) was used to predict the IVJ response to cyclic axial displacement. For comparison, the SLS model used by Li *et al.* (Li 1994; Li et al. 1995) was also investigated. The input displacement function used to simulate strain was

$$e = e_o(1 - cos(\omega \cdot t)) + e_1 \tag{3.6}$$

where e_o is the cyclic strain amplitude equal to one-half of the peak to peak strain input (100 μm/disc height), e_1 is the strain required to reach the desired preload, and $\omega = 2\pi f$ is the driving frequency where f is the desired frequency of vibration (Li 1994; Li et al. 1995).

Applying the calibrated parameters (E_1, $E_2(e)$, and μ) to the SNS model (Eqs. 3.1 & 3.3), the cyclic relaxation of the IVD was solved for a frequency of 0.01, 0.1, and 1 Hz (Fig. 3.2.3; Appendix B, Figs. B.1.1 & B.1.2). The cyclic relaxation cannot be solved analytically because of the strain-dependent stiffness in the nonlinear spring. Therefore, a numerical approach was implemented using an ordinary differential equation solver (ODE23; Matlab 7.0).

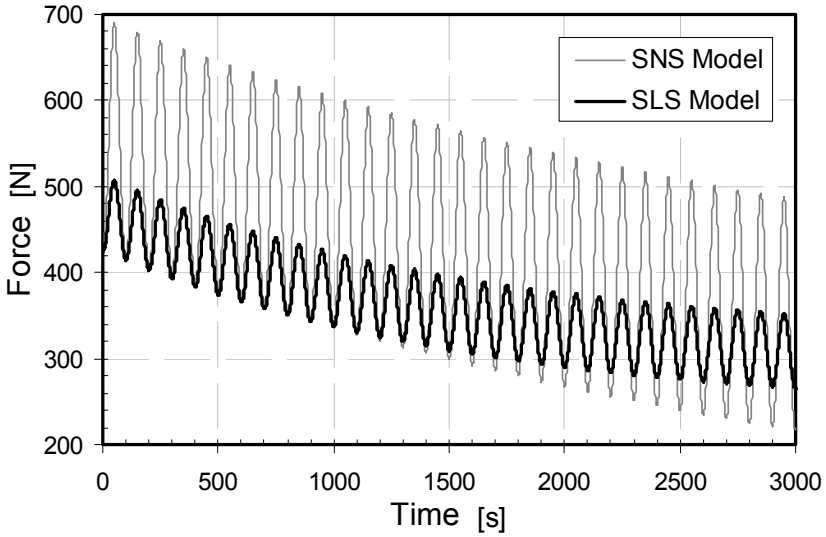

Figure 3.2.3. Cyclic relaxation of the IVD models subjected to a frequency of 0.01 Hz. Note the increase in peak to peak force of the SNS model compared to the SLS model.

3.2.5 Response to Cyclic Deformation. The response of the SNS model to cyclic deformation was used to quantify the load relaxation, the dynamic modulus, and the hysteresis of the IVD. Load relaxation index, R_i, was computed as the change in force from the initial value, F_o, to the force following the 30th cycle, F_f (Li 1994; Li et al. 1995).

$$R_i = \frac{F_o - F_f}{F_o} \tag{3.7}$$

The dynamic modulus, $E(\omega)$, was defined as the ratio of apparent stress vs. strain during the 30th cycle of the stress relaxation experiment.

$$E(\omega) = \frac{S}{e} \tag{3.8}$$

where S is the peak to peak stress and e is the peak to peak strain estimated for each driving frequency, ω (Li 1994; Li et al. 1995).

The hysteresis loop was characterized by the loading and unloading paths on a load deformation curve. The area within the hysteresis loop is the energy dissipated during one cycle of displacement. Because this area depends on the energy input, the hysteresis, λ, for one cycle of displacement was defined as the following ratio:

$$\lambda = \frac{A_L - A_{UL}}{A_L} \tag{3.9}$$

where A_L is the area under the loading curve and A_{UL} is the area under the unloading curve (Koeller et al. 1984; Li 1994; Li et al. 1995).

3.3 Results

Based on a high R^2 value of 0.993, a linear relationship (Eq. 3.4) adequately described the change in the instantaneous elastic modulus, $E_2(e)$, with axial strain, e, of the IVD (Fig. 3.2.1.A). The elastic modulus, E_1, and viscosity coefficient, μ, for the Kelvin body of the SNS model was determined to be 8.96 MPa and 102.3 GPa·s^{-1}, respectively. The model's fit to the stress relaxation experimental data (Holmes and Hukins 1996) had an average error of 6.1% and a maximum error of 20.6% (Li 1994; Li et al. 1995). The time constant ($\tau = \mu / E_1$) for the SNS model was calculated to be 190 minutes. Table 3.3.1 compares the SNS model's results with previously reported values for the three-parameter SLS model. Note that previous studies (Burns et al. 1984; Keller et al. 1987; Li et al. 1995) obtained parameters from creep data whereas current results were estimated from stress relaxation data.

Table 3.3.1. Comparison of parameters found for the three-parameter standard model. Note that previous studies obtained parameters from creep data whereas current results were estimated from stress relaxation data. * See discussion for details.

Reference	Degeneration	E_1 [MPa]	E_2 [MPa]	μ [GPa s]	τ [min]
Adjusted* Burns *et al.* (1984)	~	6.65	2.51	~	~
Keller *et al.* (1987)	~	6.26	1.61	5.41	14.4
Li *et al.* (1995)	Combined	7.62	5.06	19.6	42.8
	Mild	9.25	6.35	27.4	49.3
	Severe	6.63	4.29	15.0	37.7
Present Study	~	8.96	Eq. (3.4)	102	190

The SNS model predicted the relaxation index to be 0.49, 0.07, and 0.01 for frequencies of 0.01, 0.1, and 1 Hz, respectively. The SLS model predicted the relaxation index to be 0.38, 0.08, and 0.01, respectively. The experimental values for the relaxation index were determined by Li *et al.* (1995) to be 0.51, 0.19, and 0.1, respectively (Table 3.3.2). The SNS model underestimated the relaxation by 3.92, 63.1, and 90.0%, respectively. The SLS model underestimated the relaxation by 25.5, 57.8 and 90.0%, respectively. Moreover, accuracy of both the SLS and SNS model declined as frequency increased. The cyclic relaxation at a frequency of 0.01 Hz for the SLS model and SNS model are shown in Fig. 3.2.3. See Appendix B, for cyclic relaxation of the IVD models subjected to frequencies of 0.1 and 1 Hz (Figs. B.1.1 & B.1.2).

The SNS predicted the dynamic modulus to be 10.8, 16.5, and 17.4 MPa for frequencies of 0.01, 0.1, and 1 Hz, respectively. The SLS model predicted the dynamic modulus to be 3.33, 4.71, and 5.02 MPa, respectively. The experimental values for dynamic modulus were determined by Li *et al.* (1995) to be 10.5, 14.3 and 15.5 MPa, respectively (Table 3.3.2).

The SNS model underestimates the hysteresis ratio by 91.2, 98.7, and 99.6% for frequencies of 0.01, 0.1, and 1 Hz, respectively. The SLS model underestimates the hysteresis ratio of the IVD by 95.0, 98.7, and 99.6%, respectively. Furthermore, the calculated hysteresis ratio decreased with increasing frequency, over the range of 0.01 to 1.0 Hz (Table 3.3.2).

Table 3.3.2. Comparison of the SNS model response. The * indicates an attempt at replication of Li *et al.* (Li 1994; Li et al. 1995) model as reported in the literature and was used to create similar conditions of the present model. Values in ( ) denotes standard deviation.

Input Frequency	Present Study		Li *et al*. (1995)	
	SNS	SLS*	Experiment	SLS
	Relaxation Index, R_i [AU]			
0.01 Hz	0.49	0.38	0.51 (0.05)	0.40 (0.07)
0.1 Hz	0.07	0.08	0.19 (0.05)	0.08 (0.02)
1 Hz	0.01	0.01	0.1 (0.04)	0.01 (0.00)
	Dynamic Modulus, $E(\omega)$ [MPa]			
0.01 Hz	10.8	3.33	10.5 (3.80)	~
0.1 Hz	16.5	4.71	14.3 (5.03)	~
1 Hz	17.4	5.02	15.5 (5.47)	~
	Hysteresis, λ [%]			
0.01 Hz	0.7	0.4	8.0 (5.0)	~
0.1 Hz	0.1	0.1	8.0 (4.0)	~
1 Hz	0.04	0.04	11.0 (5.0)	~

3.4 Discussion

Many studies have noted that the IVD experiences nonlinear stress when subjected to a linear strain input (Berkson et al. 1979; Edwards et al. 1987; Gardner-Morse and Stokes 2004; Markolf 1972; Panjabi et al. 1976; Tencer et al. 1982). The nonlinear behavior of the IVD is characterized by an increase in stiffness as the IVJ is compressed. Therefore, nonlinear models should be considered when modeling phemonological behavior of the IVD.

A SNS model was introduced and developed in the present study to better represent the cyclic relaxation characteristics of the IVD. Parameters of the SNS model were estimated from load deformation and stress relaxation data (Gardner-Morse and Stokes 2004; Holmes and Hukins 1996). We quantified the performance of the SNS model subjected to cyclic displacements by calculating the load relaxation, the dynamic modulus, and the hysteresis.

The constant elastic modulus, E_1, and the viscosity coefficient, μ, of the Kelvin body were compared to previously reported parameters of the standard model (Table 3.3.1). Note that previous results (Burns et al. 1984; Keller et al. 1987; Li et al. 1995) were obtained through a least squares fit to experimental creep deformation data while in the present study the parameters were estimated from experimental stress relaxation data. Furthermore, it is important to note that Burns *et al.* (Burns et al. 1984) used the motion segments height and not disc height when calculating strain resulting in lower strain values and higher material properties. Therefore, Keller *et al.* (Keller et al. 1987) adjusted the values to more closely match realistic magnitudes of material properties using estimated disc heights.

The elastic modulus, E_1, was comparable to previously published parameters (Burns et al. 1984; Keller et al. 1987; Li 1994; Li et al. 1995). However, the viscosity coefficient, μ, was much larger than any of the values previously reported for creep deformation experiments (Keller et al. 1987; Li 1994; Li et al. 1995). The large viscosity coefficient resulted in a large time constant, indicating that the IVJ takes longer to reach equilibrium. According to Li *et al.* (1995), a large time constant also suggests the IVD has mild degeneration. However, Holmes *et al.* (Holmes and Hukins 1996) did not report the level of degeneration of the disc. One reason for the discrepancy between the current results and the results from others could be due to the extended length (4 hours) of the stress relaxation experiment. Fung *et al.* (Fung 1993) acknowledged that the relaxation constant can be affected by the length of the experiment.

The cyclic load relaxation at the end of the 30^{th} cycle was predicted by the SNS model for a frequency of 0.01 Hz. However, neither SLS nor the SNS model accurately predicted relaxation at higher frequencies (0.1 and 1 Hz) (Table 3.3.2). The underestimation of relaxation is likely attributed to the model's prediction of a decrease in hysteresis at higher frequencies. The decrease in hysteresis may be attributed to the constant viscosity coefficient of the SNS model. Conversely, Li *et al.* (1995) determined experimentally that the hysteresis does not change with frequency. This suggests that the

viscosity parameter may also be strain and/or rate dependent (i.e. μ may change with load or frequency).

The permeability of biological tissues has been described as having a dependence on strain. Tissue permeability decreases as compressive strain increases due to the drag force increasing as the interstitial spaces decrease in size (Lee and Teo 2004). In shear stress relaxation tests, Iatridis *et al.* (1997b) noted that the relaxation spectrum varied with frequency thereby describing the viscous effects as linearly increasing with frequency. An increase in viscosity at higher frequencies would suggest that the ground substance within the nucleus pulposus may have thixotropic properties (Fung 1993). Furthermore, increasing frequency increases the rate of change of the IVD's fluid volume (Cheung et al. 2003). The rate of change in fluid volume may explain a change in the viscous characteristics of the IVD. These studies support the need for a strain- and/or frequency-dependent viscosity coefficient; however, this was beyond the scope of the present study. Future studies should investigate how a strain- or frequency-dependent viscosity parameter could improve prediction of the hysteresis and relaxation of the IVD.

Although the cyclic relaxation can not be predicted for the higher frequencies, the dynamic moduli determined by the SNS model was within the standard deviation reported by Li *et al.*(1995) for frequencies of 0.01, 0.1, and 1 Hz; therefore, the SNS model was in good agreement with the experimental observations (Li et al. 1995). This indicates that the SNS model does well at all frequencies tested when predicting the force magnitude. However, because only one compressive preload was applied to the SNS model at the start of cyclic displacement, future investigations should be performed to assess how the model performs at different levels of preload.

Finite element modeling is the most popular method used in spine biomechanics to model the tissue properties, the complex loading, and the geometry of the IVJ (Natarajan et al. 2004). These models have been used extensively to determine the stress and strain placed on the vertebral bodies, IVDs, and facet joints of the spine (Argoubi and Shirazi-Adl 1996; Kasra et al. 1992; Shirazi-Adl 1989; Shirazi-Adl et al. 1986; Shirazi-Adl et al. 1984; Wang et al. 1997; Yang and King 1984). Furthermore, poroelastic models are also being developed to investigate the creep and fluid flow characteristics of the IVD (Arjmand and Shirazi-Adl 2006; Cheung et al. 2003; Laible et al. 1993; Lee and Teo 2004; Natarajan et al. 2004; Riches et al. 2002). Although these IVD models help explain many details about the disc's response to loading, they can be computationally expensive.

Current research on stability of the spine has led to the use of complex dynamic multi-segment spine models complete with musculature (Arjmand and Shirazi-Adl 2006; Franklin and Granata 2006; Kiefer et al. 1997). Tissue models expressed as phenomenological SLS or SNS ordinary differential equations are more compatible with the requirements of the dynamic musculoskeletal simulations. Therefore, we chose to develop a SNS model which focuses on the rheological motion and passive external forces of the spine. It is important to note that the SNS model is only applicable to axial loading of the IVD. Ongoing research is expanding these analyses to a multi-dimensional simulation of IVD behavior and implementing it into a dynamic multi-segment model of

the lumbar spine. Three-dimensional analyses will have to include the combined properties of IVD, ligament, and facet joint interactions. Quasi-linear and bi-exponential viscoelastic modeling techniques were beyond the scope of the present study; however, these techniques should be investigated in future studies (An and Draughn 2000; Solomonow et al. 2003; Solomonow et al. 2000).

Several limitations for the current analyses must be considered. The parameters for this study were determined from two different experimental studies. Gardner-Morse *et al.* (2004) used female lumbar (L2-L3 and L4-L5) motion segments while Holmes *et al.* (1996) used a male lumbar (L3-L4) motion segment. To help reduce gender differences, segmental height differences, and protocol differences of the two experimental data sets, the experimental values for force, displacement, and stiffness were normalized using reported values of IVD geometry. However, Holmes *et al.* (Holmes and Hukins 1996) did not report a value for the area of the disc for the male lumbar (L3-L4) specimen used for the stress relaxation data. Therefore, the area (1650 mm^2) reported by Li *et al.* (Li 1994) was used to normalize the force values. This value is comparable to the average value of other male lumbar discs found in the literature (Burns et al. 1984; Edwards et al. 1987; Keller et al. 1987).

Gardner-Morse's *et al.* (2004) study was chosen on the basis of being the most comprehensive experimental stiffness data currently available for human lumbar motion segments. However, stiffness coefficients were reported for only three different preloads. Therefore, a linear regression was chosen to model the strain-dependent elastic modulus. Stiffness coefficients reported at more preloads would better describe the strain-dependent behavior of the IVD. Furthermore, Holmes *et al.* (1996) experimental study was chosen because it is the most recent axial stress relaxation experiment of the IVD and falls within physiological limits of past research (Markolf and Morris 1974). However, the experimental data from the stress relaxation curve were estimated from graphical results, thereby increasing the error associated with the current study.

Despite these limitations, this paper presents a novel method for modeling the IVD by introducing the SNS model. Additionally, the dynamic modulus was accurately predicted at all frequencies and therefore, we feel confident that the values used and the reported results are within reason. However, a more thorough experimental validation of the SNS model is required to fine tune the parameters and to confirm the findings within this study.

3.5 Acknowledgement

Chapter 3 was supported in part by grants R01 AR46111 from NIAMS of the National Institute of Health and R01 OH07352 from NIOSH of the Centers of Disease Control. The authors would like to thank Dr. Michael Madigan for his valuable help and contributions.

Chapter 4:
Three-dimensional Lumbar Spine Model

This chapter presents:

- The development of a novel method to three-dimensionally model the quasi-static force deformation of the human intervertebral joint (IVJ) by adding a matrix of springs in parallel with the series spring of the SNS model presented in Chapter 3.
- A method to calculate the insertion points of the lamella fibers within the annulus of the intervertebral disc (IVD) based on physiologic data reported within the literature (Gardner-Morse and Stokes 2004; Holzapfel et al. 2005).
- A novel method to model the mean annular bulge due to axial compression.
- The performance of the current three-dimensional model is compared to experimentally predicted data (Gardner-Morse and Stokes 2004).

4.1 Introduction

The SNS model, which was previously discussed in Chapter 3, was expanded to a three-dimensional elastic (quasi-static) lumbar spine model. This model consists of a sacrum (S1), five lumbar vertebrae (L1-L5), one thoracic vertebra (T12) and six intervertebral discs (IVDs) (Fig. 4.1.1). The framework of the three-dimensional spine model is based on Franklin *et al.* (2006); however, the physiologic dimensions, vertebral orientation, and IVJ models have been modified within the present study.

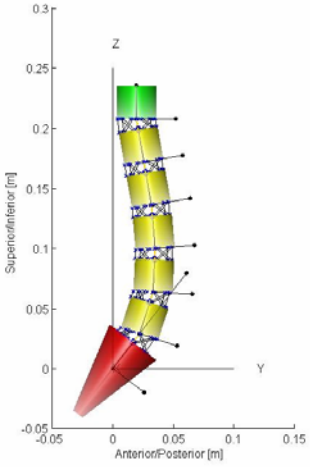

Figure 4.1.1. Three-dimensional lumbar spine model. The framework of the three-dimensional spine model is based on Franklin *et al.* (2006); however, the physiologic dimensions, vertebral orientation, and IVJ models have been modified within the present study.

Each IVD is composed of a matrix of deformable bodies in parallel, while all the vertebrae are modeled as rigid bodies (Franklin and Granata 2006). However, unlike Franklin's *et al.* (2006) IVJ model, each IVJ is able to translate and rotate in all three

dimensions allowing the model to have a total of 36 degrees of freedom (DOF). Furthermore, nonlinear force deformation of the fiber matrix is described by nonlinear strain-dependent modulus parameters and regional variations in geometry and orientation. The matrix of deformable bodies is composed of one element that represents the nucleus and 24 elements that represent the lamella fibers within the annulus pulposus of the disc (Fig. 4.1.2). The nucleus has been modeled as a deformable body that exhibits nonlinear stiffness when it is subjected to axial compression and the lamella fibers, which are distributed along two concentric layers, are modeled as deformable bodies that primarily exhibit nonlinear stiffness when subjected to tension. Furthermore, the fibers effective area has been optimized to experimental data (Gardner-Morse and Stokes 2004) of intact human lumbar specimens such that the fibers represent the regional variations in stiffness of the IVJ. Hence, the current model indirectly models the ligament and facet joint interaction of the IVJ. Furthermore, the insertion points of the lamella fibers have been calculated so that the physiologic fiber angle reported in the literature (Holzapfel et al. 2005) is maintained. The following sections will detail the development as well as the performance of this model.

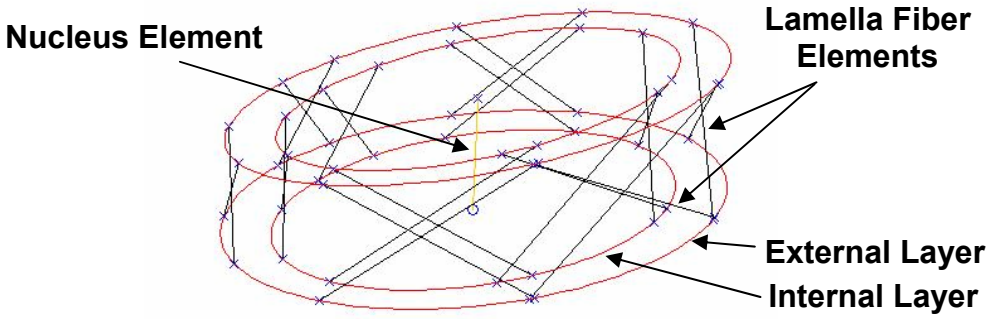

Figure 4.1.2. The IVD model. Twenty-four lamella fiber elements are distributed along two concentric layers and the nucleus element is the axial element located at the center of the IVD.

4.2 Geometry of the Spine Model.

4.2.1 Intervertebral Joint. The lateral and anterior-posterior (A-P) width of the IVD and vertebrae used in the model was 45.5 mm and 32.5 mm, respectively. Approximating the IVD as an ellipse, the cross sectional area of the disc is 1161.4 mm^2 (Gardner-Morse and Stokes 2004). The nucleus area was approximated to be 60% of the cross sectional area of the disc, 696.84 mm^2 (Markolf and Morris 1974; Shirazi-Adl et al. 1984). The IVD and vertebral heights were 8.9 mm and 27.4 mm, respectively (Gardner-Morse and Stokes 2004). Four distinct fiber regions (Dorsal Internal (Di), Dorsal External (De), Ventral Internal (Vi), and Ventral External (Ve)) were represented in the model (Fig. 4.2.1). Fiber layer 1 (external layer) was located on the outer edge of the IVD, while fiber layer two (internal layer) was located at a distance of 3.9 mm from the outer edge of the disc (Holzapfel et al. 2005). The initial length of each lamella fiber and the geometric properties used in our model can be compared to other studies (Tables 4.2.1 & 4.2.2).

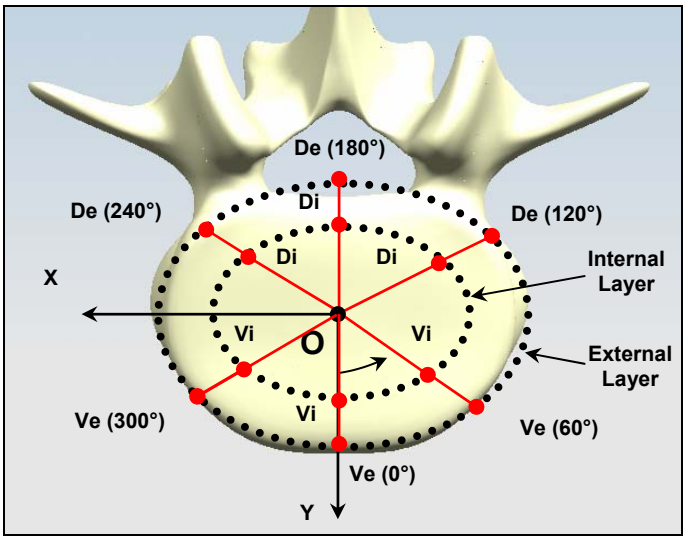

Figure 4.2.1. Fiber regions. Four distinct fiber regions were represented in the model. These were Ventro external (Ve), Ventro internal (Vi), Dorsal external (De) and Dorsal internal (Di).

Table 4.2.1. Initial IVD fiber lengths in millimeters.

Fiber #	Fiber Position	Current Study				Experimental [Holzapfel 2005]
		L2-L3		L4-L5		L1-L2
		Posture 1	Posture 2	Posture 1	Posture 2	*In Vitro*
		Length [mm]	Length [mm]	Length [mm]	Length [mm]	Length [mm]
1	Ve (60°)	18.1	18.0	20.1	19.9	18.4 (4.3)
2	De (120°)	12.7	13.5	9.6	12	~
3	De (180°)	10.3	11.3	6.5	9.9	11.2 (3.9)
4	De (240°)	13.1	13.5	10.8	12.0	~
5	Ve (300°)	18.6	18.0	21.5	19.9	18.4 (4.3)
6	Ve (0°)	23.6	23.1	28.3	26.9	~
7	Ve (60°)	18.6	18.0	21.5	19.9	18.4 (4.3)
8	De (120°)	13.1	13.5	10.8	12.0	~
9	De (180°)	10.3	11.3	6.5	9.9	11.2 (3.9)
10	De (240°)	12.7	13.5	9.6	12.0	~
11	Ve (300°)	18.1	18.0	20.1	19.9	18.4 (4.3)
12	Ve (0°)	23.6	23.1	28.3	26.9	~
13	Vi (60°)	17.5	17.4	18.8	18.7	12.1 (2.2)
14	Di (120°)	13.1	13.7	10.6	12.5	~
15	Di (180°)	10.7	11.5	7.9	10.4	10.0 (2.3)
16	Di (240°)	13.5	13.7	11.7	12.5	~
17	Vi (300°)	17.9	17.4	20.1	18.7	12.1 (2.2)
18	Vi (0°)	22.1	21.7	25.3	24.3	~
19	Vi (60°)	17.9	17.4	20.1	18.7	12.1 (2.2)
20	Di (120°)	13.5	13.7	11.7	12.5	~
21	Di (180°)	10.7	11.5	7.9	10.4	10.0 (2.3)
22	Di (240°)	13.1	13.7	10.6	12.5	~
23	Vi (300°)	17.5	17.4	18.8	18.7	12.1 (2.2)
24	Vi (0°)	22.1	21.7	25.3	24.3	~

Table 4.2.2. Geometric properties of the IVD.

Reference:	Level	Disc Height [mm]	Lateral Diameter [mm]	Sagittal Diameter [mm]	Disc Area [mm^2]	Nucleus Area [mm^2]
Experimental Studies:						
Burns *et al*. [1984]	S1-L1(9)	~	~	~	1808	~
Keller *et al.* [1987]	L1-L2 (4)	9.2	~	~	1664	~
	L2-L3 (3)	10.7	~	~	1903	~
	L3-L4 (6)	10	~	~	2195	~
	L4-L5 (2)	12.6	~	~	1606	~
Li *et al.* [1995]	Lumbar(8)	9.64	~	~	1650	~
Edwards *et al*. [2001]	L2-L3 (3)	8.8	~	~	1320	~
	L4-L5 (6)	9.9	~	~	1396	~
Izambert *et al.* [2003]	L1-L2 (6)	7.42	~	~	1257	~
	L2-L3 (1)	9.5	~	~	1442	
	L3-L4 (1)	10	~		1519	~
Gardner-Morse *et al*. [2004]	L2-L3 & L4-L5 (8)	8.9 ~	45.5 ~	32.5 ~	1161 ~	~ ~
Finite Element Studies:						
Shirazi Adl *et al*. [1984]	L2-L3	11.0	49.2	34.0	1371	632
Campbell *et al.* [2004]		10.0	~	~	1371	632
Present Study	T12-S1	8.9	45.5	32.5	1161	697

4.2.2 Posture. Currently, there are two postures that can be set for this model. However, if desired more postures can easily be added (i.e. scoliosis) at a later date (Franklin and Granata 2006). Posture '1' is the normal lordotic posture of the spine during quiet standing while posture '2' is a vertical posture. Radiographic measurements are the gold standard for determining the angle of inclination of the vertebrae. Therefore, radiographic measurements obtained from the literature were used to describe the normal lordotic posture used in this study (Table 4.2.3) (Chen 2000). Angle of inclination is referenced to the transverse plane. Furthermore, lateral and axial angles of inclination have all been assumed to be zero.

Table 4.2.3. Physiologic angle of inclination of each vertebral level. Measurements are referenced from the sagittal plane in the anatomical posture (Chen 2000).

Vertebral Level	Posture 1 Angle of Inclination (Degrees)	Posture 2 Angle of Inclination (Degrees)
S1	-37.5	0
L5	-17.8	0
L4	-2.8	0
L3	4.9	0
L2	9.9	0
L1	9.7	0

4.3 Modeling the Nucleus

The nucleus was modeled as the instantaneous spring of the viscoelastic standard nonlinear solid (SNS) model. The nonlinear behavior of the nucleus was simulated by a strain-dependent elastic modulus. The instantaneous modulus of the SNS model was estimated from experimental load deformation data. Furthermore, it was shown that axial stiffness is not significantly different between L2-L3 and L4-L5 segmental levels (Gardner-Morse and Stokes 2004). Therefore, the nucleus model was assumed to be the same for each segmental level. Details of this model are discussed in Chapter 3.

4.4 Modeling the Lamella Fibers

A single lamella fiber is considered to be the "elementary structural unit" of the annulus fibrosus (Holzapfel et al. 2005). Each lamella fiber is made up of highly oriented collagen fiber bundles and a non-fibrous matrix of ground substance. Although several studies have oriented the collagen fiber bundles with a mean angle of 30° (Campbell-Kyureghyan 2004; Shirazi-Adl et al. 1984), recent research indicates that the orientation of the collagen bundles has a distinct mean angle between 30° and 150° that varies in the circumferential and radial directions (Holzapfel et al. 2005). Moreover, the lamellae in adjacent concentric layers are perpendicularly oriented to one another. Because the lamella is considered to be "the elementary structure," we chose to use it as the building block for the annulus of the IVD model. The following sections will detail how the orientation of the fibers were modeled and calculated.

4.4.1 Position and Orientation of Lamella Fibers. To estimate the position and orientation of each lamella fiber, the inferior and superior portion of the IVD were approximated to be the shape of an ellipse of equal dimensions (Fig. 4.4.1.A). Using the elliptical geometry, coordinates of any circumferential position (a.k.a. polar points) can then be found by creating an infinite length vector originating at the origin of the ellipse, rotating this vector by any given polar angle, α, and calculating the intersection point, P, between the vector and the ellipse (Fig. 4.4.1.B & 4.4.1.C).

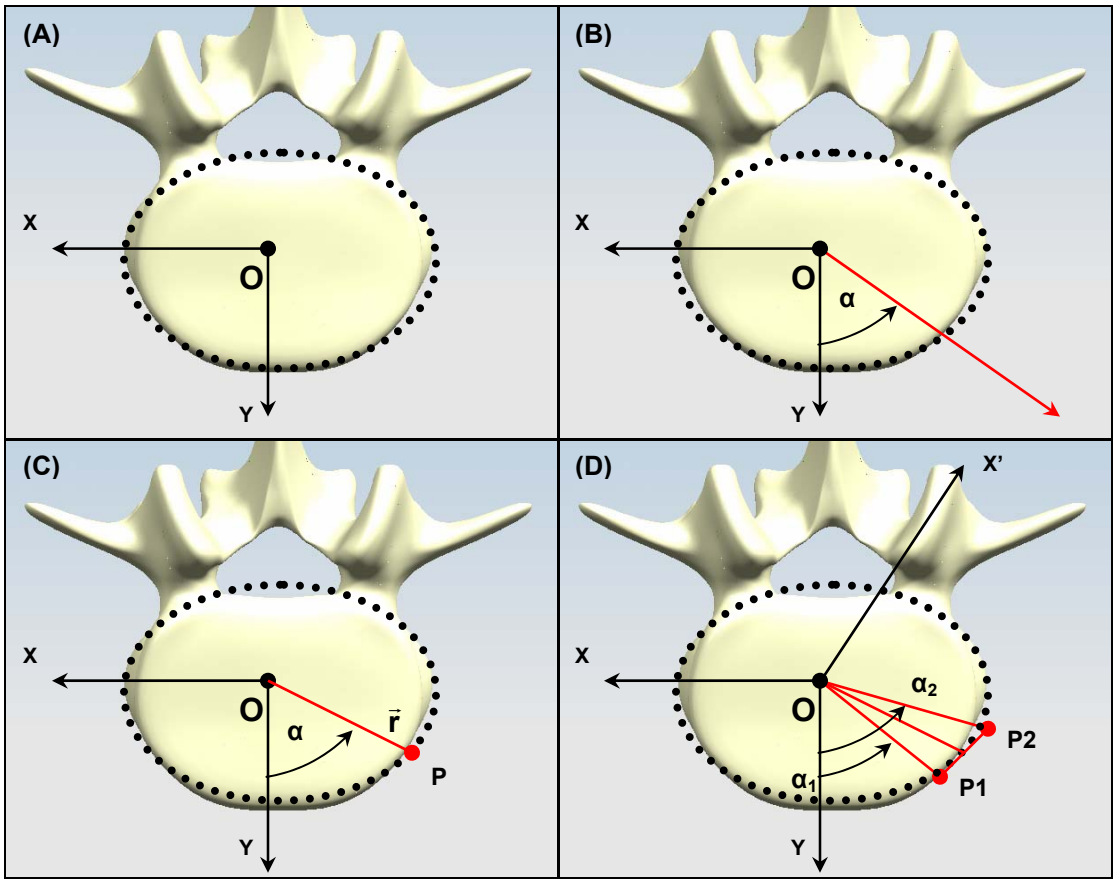

Figure 4.4.1. Calculation of insertion points. The transverse view of the inferior vertebral body is shown. The dotted ellipse approximates the shape of IVD.

Once each polar point is calculated within the body coordinate system for both the inferior and superior portion of the IVD, the polar points are transformed into absolute coordinates so that the points are representative of a user supplied posture. After placing the polar points into the proper posture, calculation of the disc height, *h*, at each polar point is possible and is calculated using the distance formula between two points (Fig. 4.4.2). The distance formula was calculated as,

$$h = \sqrt{(Ps_x - Pi_x)^2 + (Ps_y - Pi_y)^2 + Ps_z - Pi_z)^2}\,, \qquad (4.1)$$

where *P* denotes polar point, *s* denotes superior, *i* denotes inferior, and the subscripts *x,y,z* denotes the coordinate axes.

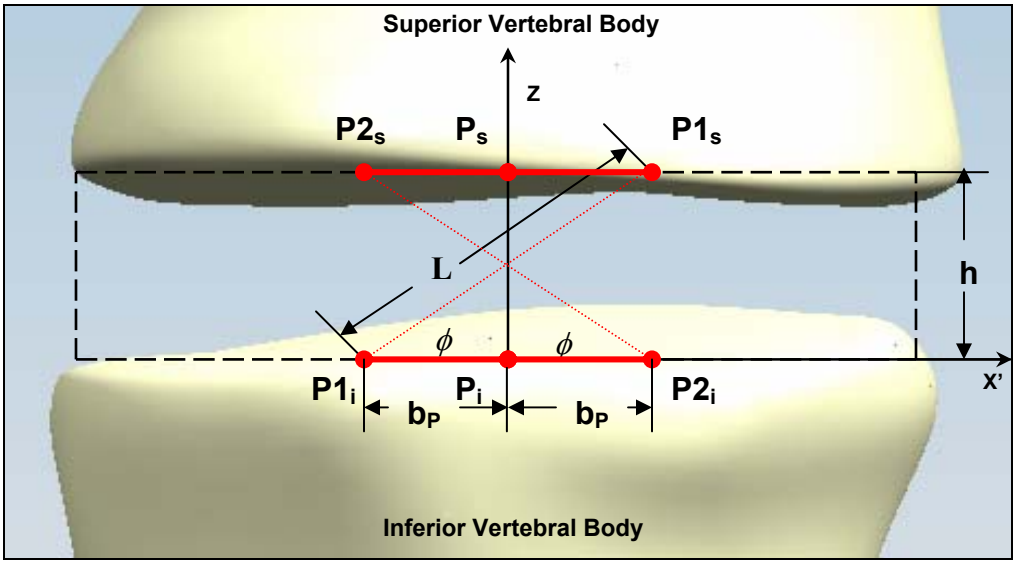

Figure 4.4.2. Calculation of the lamella fiber angle and orientation. Oblique view of the superior and inferior vertebral body is shown. Calculation of lamella fiber position and orientation can be found by knowing the height of the disc, h, length of the fiber, L, and fiber angle, ϕ, at each polar point, *P*.

The absolute fiber angle, ϕ, at each polar point is calculated using the following empirical relationship (Holzapfel et al. 2005).

$$|\phi| = 23.2 + 0.130 \cdot \alpha \qquad (4.2)$$

where α is the polar angle at each polar point (Fig. 4.4.3).

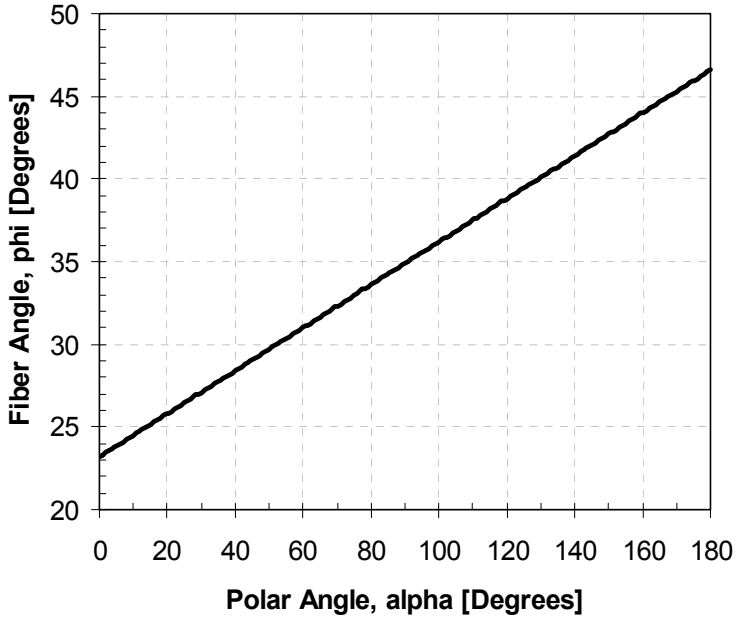

Figure 4.4.3. Absolute fiber angle for each polar point. The absolute fiber angle is approximated as a linear function (Holzapfel et al. 2005).

Once the disc height and the fiber angle at each polar point is calculated, the length, L, of each fiber is calculated using the trigonometric relationship,

$$L = \frac{h}{sin(\phi)}, \tag{4.3}$$

where h is the height at each polar point and ϕ is the fiber angle at the polar point.

Knowing the length of the fiber and the fiber angle at each polar point, we can calculate the perpendicular distance of the insertion points to the polar point as,

$$b_P = \frac{L \cdot cos(\phi)}{2}, \tag{4.4}$$

where L is the fiber length and ϕ is the fiber angle.

Using the perpendicular distance between the insertion point and the polar point the angle, θ, is calculated as

$$\theta = atan(\frac{b_p}{mag(r_p)}) \tag{4.5}$$

where b_p is the perpendicular distance between the insertion point and the polar point and $mag(r_p)$ is the magnitude of the intersecting vector, r_p.

Using this angle, we can calculate the insertion points by adding or subtracting the angle, θ, from the polar angle, α, as follows (Fig. 4.4.1.D).

$$\begin{aligned} \alpha_1 &= \alpha - \theta \\ \alpha_2 &= \alpha + \theta \end{aligned} \tag{4.6}$$

This procedure was repeated for all polar points and layers. Appendix A.2 provides details on how to run the Matlab program, *element_pos_orient.m*, that determines the insertion points of the elements.

4.4.2 Lamella Fiber Model. The orientation of the collagen fiber bundles allows the lamellae to primarily resist tensile forces (Holzapfel et al. 2005). Therefore, we chose to model the lamella fiber as a nonlinear cable element. This means that under the critical strain the element will slacken. To capture the nonlinear stress-strain behavior of the lamellae fibers we used a ligament model found within the literature (Campbell-Kyureghyan 2004). The following mathematical model describes how the modulus, E, changes with the strain of the element:

$$E = [1 + tan(\psi(e - e_o))][(E_{high} - E_{low})/2] + E_{low} \tag{4.7}$$

where ψ is the curve parameter, e is the fiber strain, e_o is critical fiber strain, E_{high} is the high stress modulus, and E_{low} is the low stress modulus. The modulus parameters were determined from literature (Holzapfel et al. 2005) (Table 4.4.1). The curve parameter and critical strain were determined through a least squares curve fit to Holzapfel's *et al.* experimental data (Fig. 4.4.4).

Table 4.4.1. Fiber element modulus parameters.

Position	E_{low} [MPa]	E_{high} [MPa]	ψ	e_o
De	8.01	64.8	41.8	0.074
Di	3.8	31.2	32.0	0.234
Ve	5.96	77.6	91.4	0.018
Vi	3.79	27.5	25.0	0.090

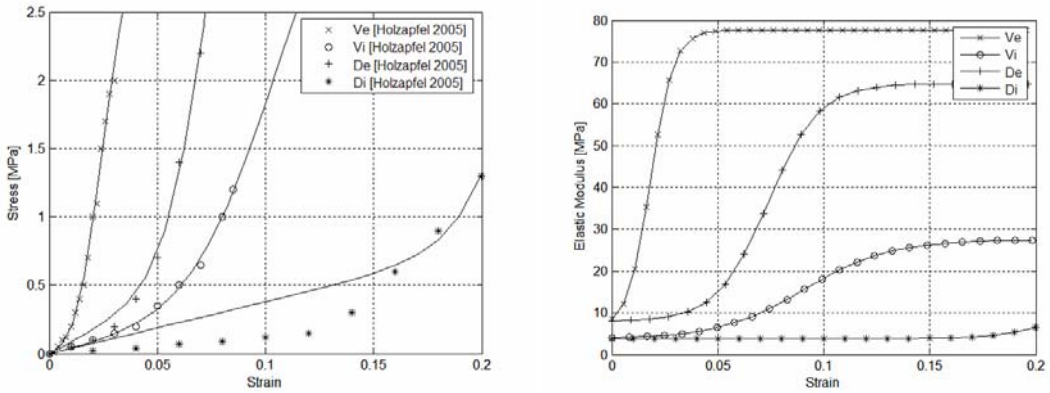

Figure 4.4.4. Nonlinear fiber elements. The nonlinear stress of the each lamella fiber element is described by a change in modulus as a function of strain. Modulus parameters for the fiber elements were obtained from the literature (Holzapfel et al. 2005). A least squares curve fit applied to the experimental data to determine the curve parameter, ψ, and critical strain, e_o.

4.4.3 Estimating Intervertebral Disc Bulge. Bulging of the IVD occurs during normal and extreme *in vivo* motions and loads to the spine (Reuber et al. 1982; Wenger and Schlegel 1997). When building a model of the IVD, it is useful to understand how much the IVD bulges so that the apparent strain in the lamella fibers can be approximated. Bulging of the IVD due to an axial compressive load was estimated by assuming that the IVD is an incompressible fluid within a cylinder of radius, r_1 (Fig. 4.4.5).

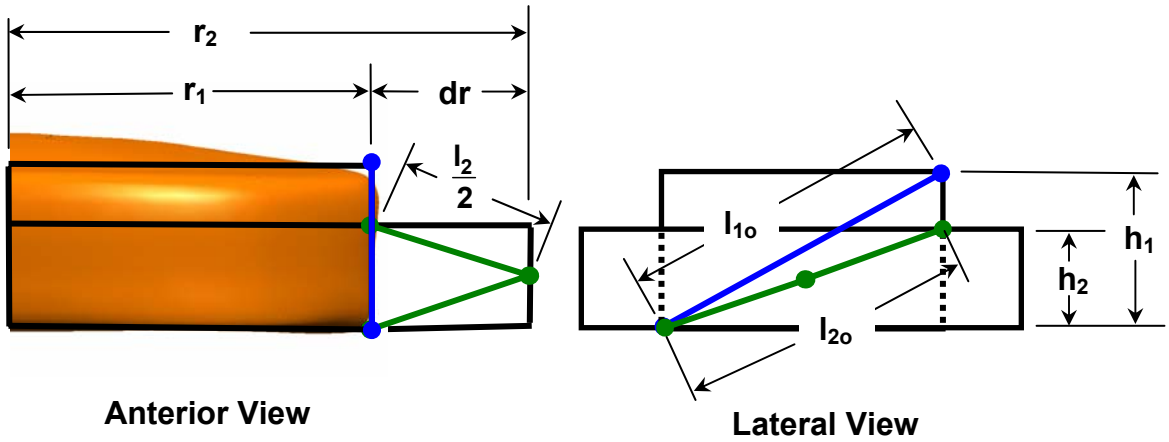

Figure 4.4.5. Fiber Bulge. Bulging of the IVD was estimated by assuming that the IVD was an incompressible fluid and was calculated from the dimensions of the IVD.

The incompressible fluid assumption requires that the volume remains constant. Therefore, any change in height of the IVD will result in a change in radius which is governed by the following equation,

$$V = 2\pi r_1^{\,2} h_1 = 2\pi r_2^{\,2} h_2, \qquad (4.8)$$

where r_1 is the initial radius of the IVD, h_1 is the initial height of the IVD, r_2 is the new radius of the IVD, and h_2 is the new height of the IVD. Rearranging the equation we can determine the new radius, r_2, given a change in height of the IVD as,

$$r_2 = \sqrt{\frac{r_1^2 h_1}{h_2}}. \tag{4.9}$$

The disc bulge, *dr*, is then calculated as the change in radius,

$$dr = r_2 - r_1 = r_1\left(\sqrt{\frac{h_1}{h_2}} - 1\right). \tag{4.10}$$

To estimate the new fiber length, l_2, due to the disc bulge, Pythagorean's Theorem was applied and the following relationship was developed,

$$l_2 = 2 \cdot \left[dr^2 + \left(\frac{l_{20}}{2}\right)^2 \right]^{1/2}, \tag{4.11}$$

where l_{20} is the new fiber length before calculating for the bulge. Results are comparable to experimental measurements (Table 4.4.2).

Table 4.4.2. Estimation of IVD bulge.

Axial Compressive Force [N]	Mean Annular Bulge [mm]		
	Reuber *et al.* (1982)	Wenger *et al.* (1997)	Current Study
400	0.295	~	0.24
800	0.445	~	0.39
2500	~	0.67	0.79

4.4.4 Optimization of Effective Area. Experimental 6x6 stiffness matrices at three different preloads and two segmental levels (L2-L3 & L4-L5) were obtained from the literature (Gardner-Morse and Stokes 2004). Experimental predictions of IVD force behavior was based on a change in stiffness of the IVD as a function of axial displacement for each of the six degrees of freedom by applying a linear curve fit to the experimental data (Fig. 4.4.6) (Appendix B, Fig. B.2.1). With linear stiffness approximations known for each preload displacement, experimental predictions of intervertebral joint (IVJ) loads, *F,* was approximated using a displacement dependent variation of Hooke's law,

$$F = K(z)X, \tag{4.12}$$

where *K(z)* is a 6x6 axial displacement dependent stiffness matrix and *X* is a 6x1 displacement vector. Hooke's law allowed us to predict the nonlinear force response of the IVJ when subjected to a change in displacement for all six degrees of freedom. Once

the force in all six degrees of freedom could be predicted, the present IVJ model could be tuned.

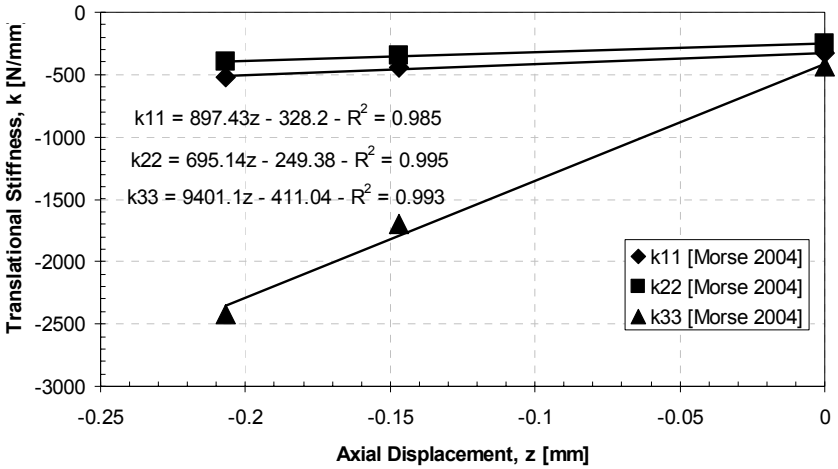

Figure 4.4.6. Predicting the nonlinear response of the IVJ. The nonlinear response of the IVJ was predicted by applying a linear curve fit to the experimental stiffness data found in the literature (Gardner-Morse and Stokes 2004).

Effective area of each lamella fiber element of the IVD was tuned through least squares optimization by applying rotational displacements (±5°) along each of the three body coordinate axes for three set preload displacements (0 mm, 0.1033 mm, and 0.2066 mm). The optimization routine compared the current fiber model's load output to the experimentally predicted load output and determined an effective area at each preload by minimizing the sum of the square differences for each degree of freedom. A linear regression was then used to account for the increase in effective area as a function of preload displacements (Fig.4.4.7) (Appendix B, Fig. B.2.2-B.2.4). Moreover, the rotational displacements chosen, allowed the fibers to stretch to their normal physiological limit (Jayson 1987). Furthermore, the effective areas found for each element accounted for the regional variations in stiffness of the IVD as well as the increase in stiffness with axial load.

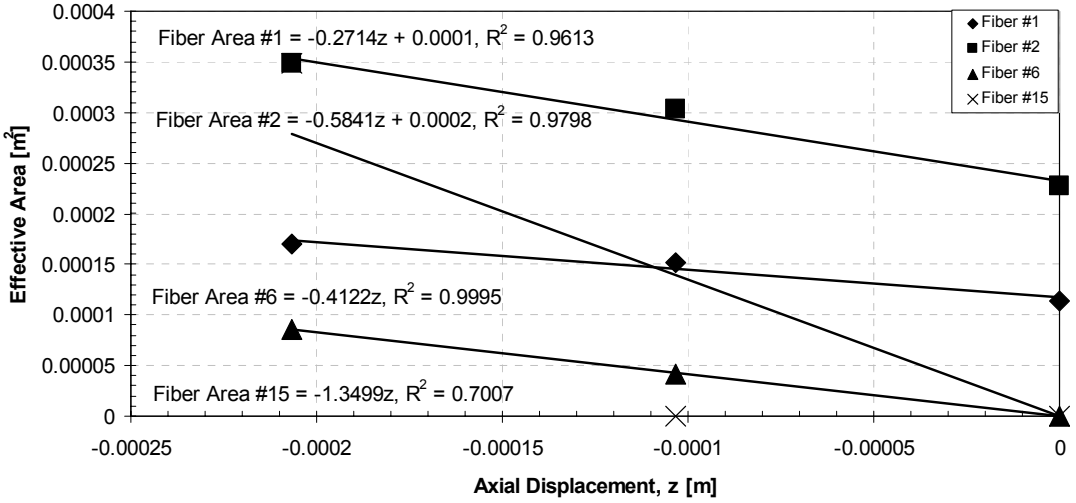

Figure 4.4.7. Modeling the effective area of the IVJ as function of preload displacement (Posture 1, L2-L3). As the IVJ is compressed, the effective area of the IVJ increases due to increased contact area with the facet joints. The increase in effective area was modeled by optimizing elemental fiber area with change in preload displacement. Note: for simplicity, symmetric fibers are not shown.

4.5 Results

The experimental validation of the three-dimensional model was beyond the scope of this study; however, the model's performance is compared to Gardner-Morse's *et al.* (2004) experimental data which was predicted from the literature. The following subsections display the model's response to various physiological motions under three preload conditions, two postures and two segmental levels. In addition, root mean square (RMS) error is used to compare the models response to experimentally predicted data as well as to compare to differences in modeling postures.

4.5.1 Model's Response. When the IVD model is subjected to axial compression, the length of the nucleus and fiber elements decrease. The strain-dependent modulus within each of these elements causes the characteristic nonlinear behavior of the IVD (Fig. 4.5.1.A). Furthermore, regional variations in stiffness result in a nonlinear coupled flexion response (Fig. 4.5.1.B).

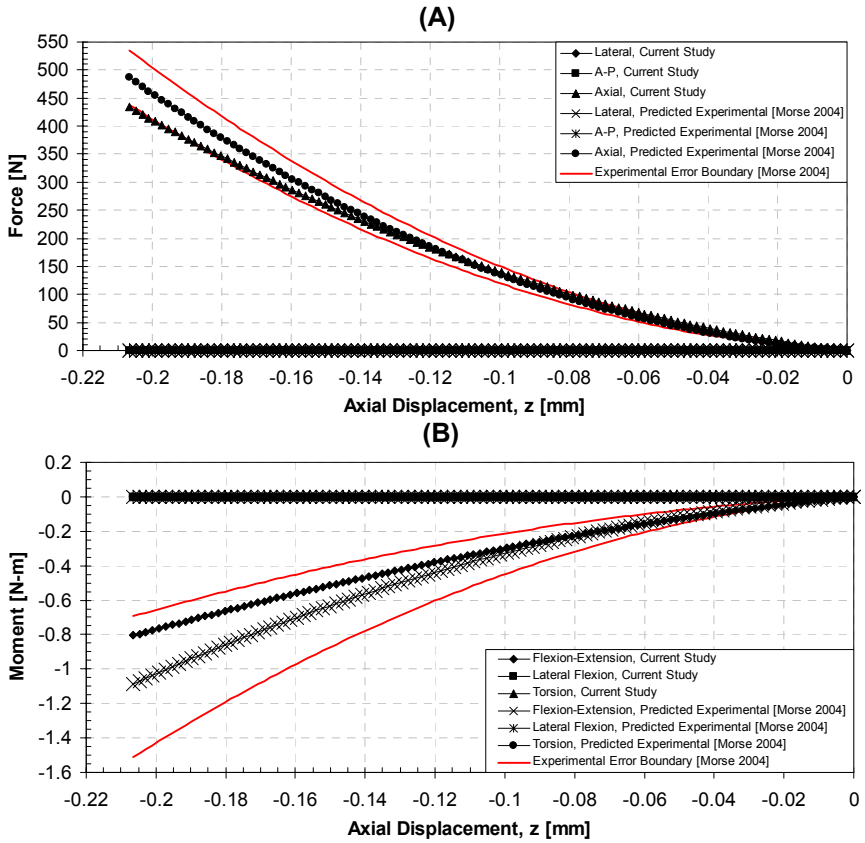

Figure 4.5.1. Three-dimensional model's response to axial compression (Posture 1, L2-L3). (A) The IVD model's response to axial compression represents the nonlinear behavior of the IVD. (B) A nonlinear coupled flexion response is predicted for axial compression of the IVD due to regional variation of the IVJ. Note the experimental error boundary was calculated from the standard deviation of the stiffness coefficients reported in the literature (Gardner-Morse and Stokes 2004).

During flexion and extension, the IVD undergoes a combination of axial and anterior-posterior shearing forces (Fig. 4.5.2.). The combination of these forces produces a net moment around the lateral axis. All flexion-extension figures for a range of preload displacements, postures, and segmental levels can be found in Appendix B.

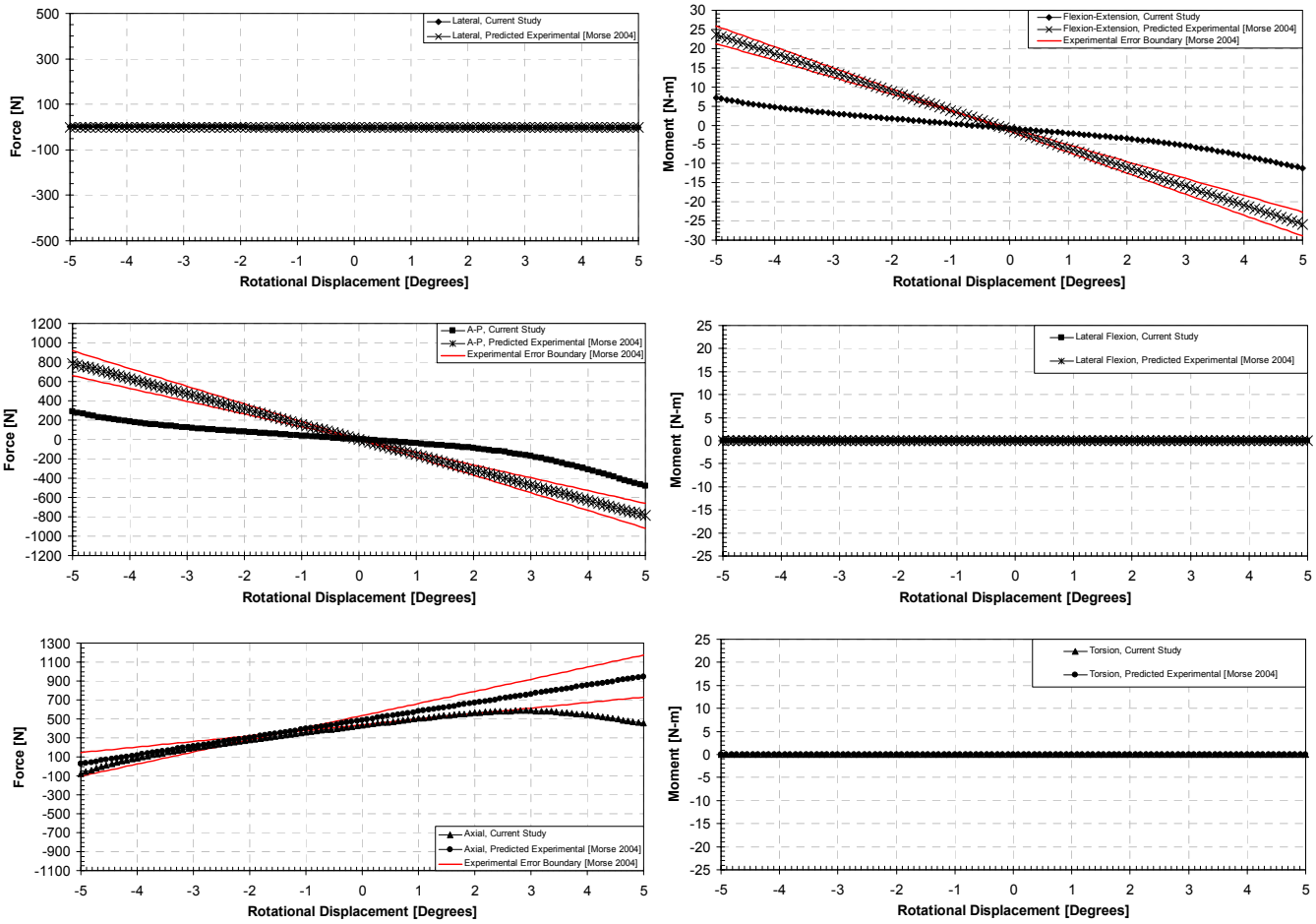

Figure 4.5.2. Three-dimensional model's response to flexion/extension under a preload displacement of 0.2066 mm (Posture 1, L2-L3).

For lateral flexion, the model's prediction shows that the IVD primarily experiences a combination of axial and lateral shearing force (Fig. 4.5.3). However, at larger ranges of motion the IVD also experiences small amounts of torsion and flexion/extension (Appendix B). The combination of these forces produces a net moment around the anterior-posterior axis. Furthermore, a stiffening of the lamella fibers is evident as the lateral rotation of the IVD increases. All lateral flexion response figures for a range of preload displacements, postures, and segmental levels can be found in Appendix B.

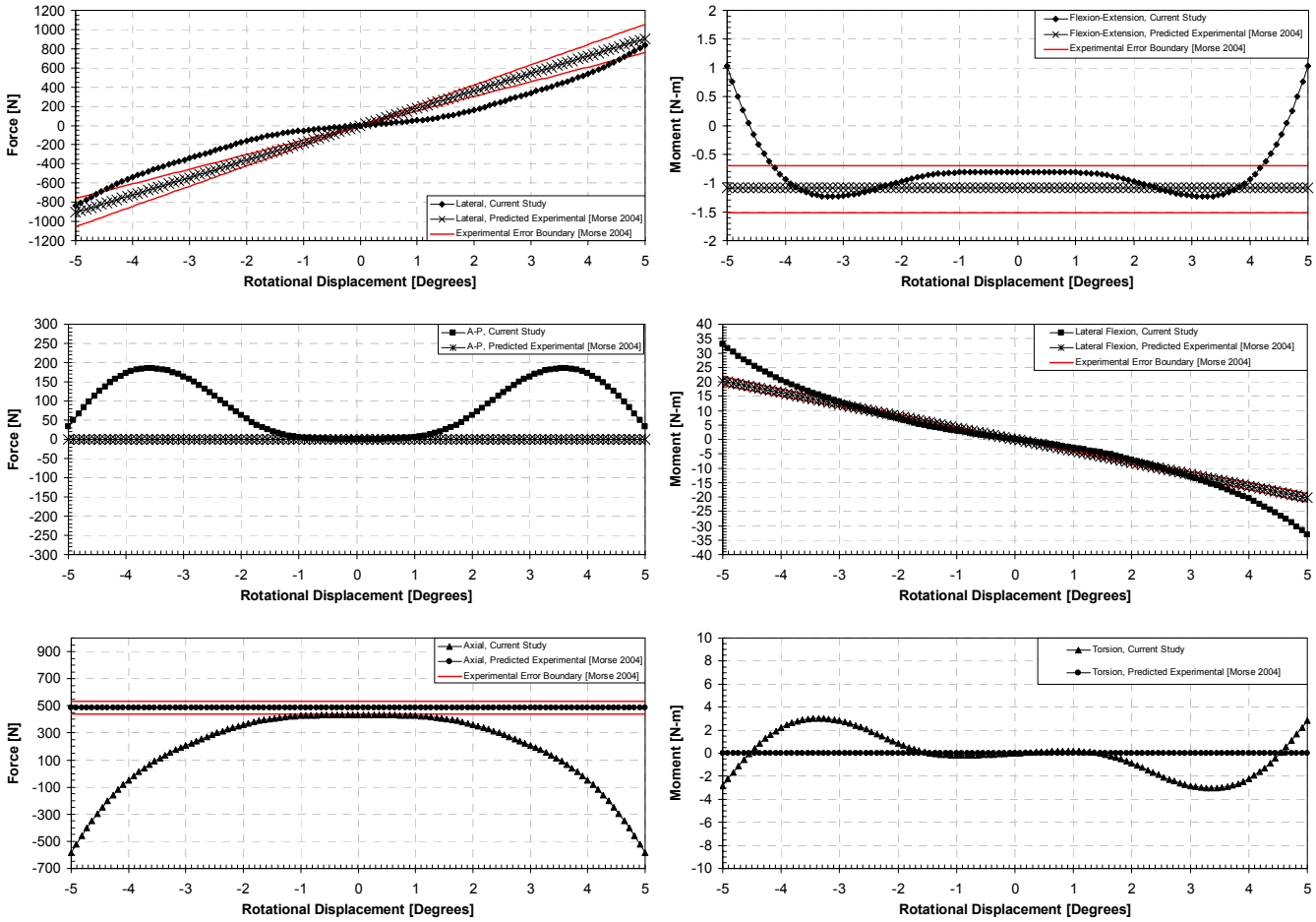

Figure 4.5.3. Three-dimensional model's response to lateral flexion under a preload displacement of 0.2066 mm (Posture 1, L2-L3).

In torsion, the model's prediction shows that the IVD primarily experiences a combination of axial and lateral shearing forces (Fig. 4.5.3). Furthermore, the IVD experiences small amounts of anterior-posterior shearing forces, lateral flexion, and extension-flexion at larger ranges of motion (Appendix B). The combination of these forces produces a net moment around the axial axis in each of the respective coordinate directions. Furthermore, a stiffening effect is evident as the IVD is rotationally displaced. All torsion response figures for a range of preload displacements, postures, and segmental levels can be found in Appendix B.

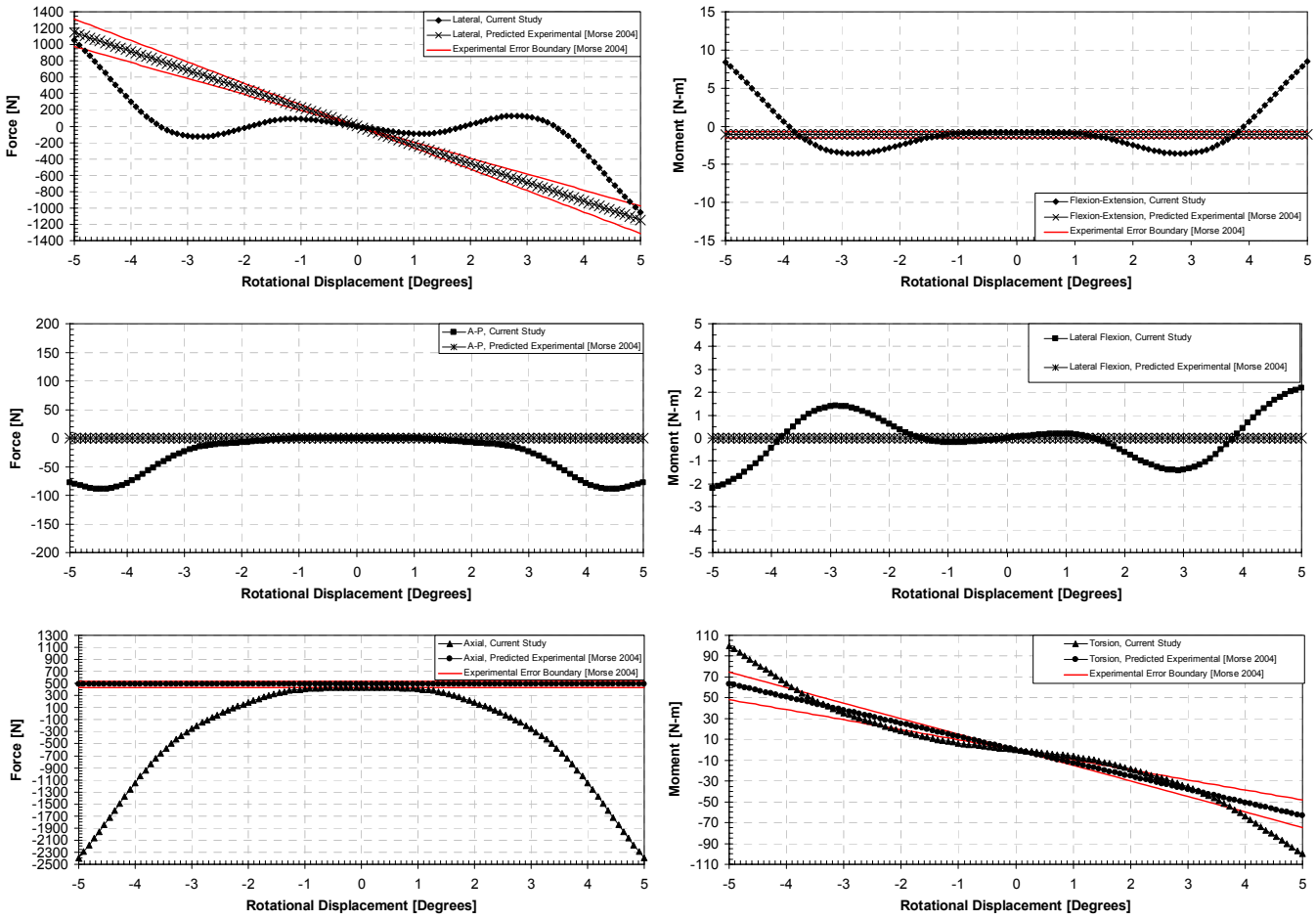

Figure 4.5.4. Three-dimensional model's response to torsion under a preload displacement of 0.2066 mm (Posture 1, L2-L3).

4.5.2. Model Comparison. Root mean square (RMS) error was used to compare the current study's response to the experimentally predicted response and posture differences (Tables 4.5.1. & 4.5.2) (Appendix C, Tables C.1 & C.2). The RMS error was calculated for two ranges of motion, three loading conditions, three preload displacements, two postures and two segmental levels. Caution should be exercised when comparing loading conditions, preload displacements, and segmental levels because different sets of experimental data were used when optimizing the effective area for each condition. Furthermore, when comparing to the experimentally predicted data, the linear range of motion is more likely to demonstrate the model's ability to predict the three-dimensional behavior of the IVJ. The linear range of motion is approximately 20% of the physiological range of motion and was used by Gardner-Morse *et al.* when determining the stiffness at each level of preload (Gardner-Morse and Stokes 2004).

When the L2-L3 joint is subjected to axial compression, the sum of the RMS force errors for posture '1' and '2' are 18.99 N and 27.5 N, respectively and the sum of the RMS moment errors are 0.112 N-m and 0.553 N-m, respectively. A similar but more pronounced trend is seen when the L4-L5 joint is subjected to axial compression. For this condition the sum of the RMS force errors are 19.57 N and 59.0 N, respectively and the sum of the RMS moment errors are 0.107 N-m and 0.987 N-m, respectively.

When the L2-L3 joint is subjected to extension-flexion within the full range of motion, the sum of the RMS force error for posture '1' and '2' are 1048 N and 3170 N, respectively and the sum of the RMS moment errors are 28.2 N-m and 22.2 N-m, respectively. For the L4-L5 joint the sum of the RMS force errors are 1635 N and 4250 N, respectively and the sum of the RMS moment errors are 44.7 N-m and 30.8 N-m, respectively.

Within the linear range of motion, the sum of the RMS force errors for the L2-L3 joint decrease to 238 N and 359 N, respectively and the sum of the RMS moment errors decrease to 6.22 N-m and 4.04 N-m, respectively. For the L4-L5 joint the sum of the RMS force errors are 312 N and 513 N, respectively and the sum of the RMS moment errors are 9.96 N-m and 7.89 N-m, respectively.

When the L2-L3 joint is subjected to lateral flexion within the full range of motion, the sum of the RMS force error for posture '1' and '2' are 1809 N and 1427 N, respectively and the sum of the RMS moment errors are 20.0 N-m and 14.9 N-m, respectively. For the L4-L5 joint the sum of the RMS force errors are 2304 N and 2600 N, respectively and the sum of the RMS moment errors are 28.1 N-m and 53.2 N-m, respectively.

Within the linear range of motion, the sum of the RMS force errors for the L2-L3 joint decrease to 383 N and 298 N, respectively and the sum of the RMS moment errors decrease to 2.89 N-m and 5.33 N-m, respectively. For the L4-L5 joint the sum of the RMS force errors are 370 N and 426 N, respectively and the sum of the RMS moment errors are 7.60 N-m and 6.72 N-m, respectively.

When the L2-L3 joint is subjected to torsion within the full range of motion, the sum of the RMS force error for posture '1' and '2' are 4536 N and 4020 N, respectively and the sum of the RMS moment errors are 43.8 N-m and 33.36 N-m, respectively. For the L4-L5 joint the sum of the RMS force errors are 4385 N and 4093 N, respectively and the sum of the RMS moment errors are 43.3 N-m and 41.0 N-m, respectively.

Within the linear range of motion, the sum of the RMS force errors for the L2-L3 joint decrease to 337 N and 275 N, respectively and the sum of the RMS moment errors decrease to 10.7 N-m and 12.5 N-m, respectively. For the L4-L5 joint the sum of the RMS force errors are 315 N and 379 N, respectively and the sum of the RMS moment errors are 12.8 N-m and 15.6 N-m, respectively.

Table 4.5.1. Root mean square error over the physiologic range of motion (L2-L3).

Loading Condition	Preload Displacement [mm]	Root Mean Square (RMS) Error (L2-L3)					
		Lateral [N]		A-P [N]		Axial [N]	
		Posture 1	Posture 2	Posture 1	Posture 2	Posture 1	Posture 2
Axial Compression	0 – 0.2066	0	0	0.09	0	18.99	27.5
Extension/Flexion (±5°)	0	0	0	172	206	93.2	902
	0.1033	0	0	227	251	106	807
	0.2066	0	0	287	304	163	700
Lateral Flexion (±5°)	0	83.4	74.3	62.1	42.0	380	269.8
	0.1033	118	103	85.1	57.1	388	311.9
	0.2066	164	143	111	71.1	418	355
Torsion (±5°)	0	357	418	32.7	0	882	760
	0.1033	431	473	40.0	0	1042	867
	0.2066	505	536	45.6	0	1201	966
		Extension/Flexion [N-m]		Lateral Flexion [N-m]		Torsion [N-m]	
Axial Compression	0 – 0.2066	0.112	0.553	0	0	0	0
Extension/Flexion (±5°)	0	9.06	8.34	0	0	0	0
	0.1033	9.39	7.49	0	0	0	0
	0.2066	9.83	6.46	0	0	0	0
Lateral Flexion (±5°)	0	0.769	0.286	4.65	1.93	1.47	1.10
	0.1033	0.629	0.649	4.56	3.10	1.57	1.61
	0.2066	0.560	.926	4.13	3.63	1.72	1.72
Torsion (±5°)	0	3.01	3.94	0.887	1.05	7.94	4.88
	0.1033	3.10	3.72	0.900	1.19	10.9	6.26
	0.2066	3.12	3.47	0.988	1.20	13.0	7.65

Table 4.5.2. Root mean square error over the linear range of motion (L2-L3).

Loading Condition	Preload Displacement [mm]	Root Mean Square (RMS) Error (L2-L3)					
		Lateral [N]		A-P [N]		Axial [N]	
		Posture 1	Posture 2	Posture 1	Posture 2	Posture 1	Posture 2
Axial Compression	0 – 0.2066	0	0	0.09	0	18.99	27.5
Extension/Flexion (±1°)	0	0	0	46.8	51.2	6.43	59.7
	0.1033	0	0	57.9	62.2	3.99	64.2
	0.2066	0	0	68.8	72.6	54.5	49.1
Lateral Flexion (±1.5°)	0	64.2	53.7	14.1	8.95	18.4	12.5
	0.1033	86.6	75.5	11.2	7.21	11.8	30
	0.2066	109	97.7	8.18	5.16	60.2	7.99
Torsion (±1°)	0	89.7	82.0	0.828	0	16.8	16.8
	0.1033	83.1	73.8	0.408	0	10.27	28.5
	0.2066	76.6	65.6	0.250	0	59.2	8.48
		Extension/Flexion [N-m]		Lateral Flexion [N-m]		Torsion [N-m]	
Axial Compression	0 – 0.2066	0.112	0.553	0	0	0	0
Extension/Flexion (±1°)	0	1.99	1.19	0	0	0	0
	0.1033	2.07	1.33	0	0	0	0
	0.2066	2.16	1.52	0	0	0	0
Lateral Flexion (±1.5°)	0	0.0498	0.041	0.459	0.914	0.191	0.133
	0.1033	.0274	0.54	0.707	1.03	0.109	0.259
	0.2066	0.273	0.869	0.951	1.14	0.127	0.396
Torsion (±1°)	0	0.144	0.107	0.0280	0.131	2.91	2.99
	0.1033	0.068	0.581	0.079	0.217	3.36	3.41
	0.2066	0.249	0.896	0.138	0.303	3.78	3.82

4.6 Discussion

As an expansion to the SNS model reported in Chapter 3, a sagittally symmetric three-dimensional elastic (quasi-static) lumped-parameter model of the IVJ was developed by adding two concentric layers of strain-dependent springs (lamella fibers) in parallel with the axial instantaneous spring of the SNS model. These elements were added such that they represent the physiologic orientation, fiber angle, and nonlinear stiffness associated with the IVJ.

The geometry of the three-dimensional IVD model was based off of the experimental measurements made by Gardner-Morse *et al.* (2004). The geometry used was very comparable to other experimental and theoretical studies (Table 4.2.1) (Burns et al. 1984; Campbell-Kyureghyan 2004; Edwards et al. 2001; Gardner-Morse and Stokes 2004; Keller et al. 1987; Li et al. 1995; Shirazi-Adl et al. 1984). Furthermore, the fiber lengths were comparable to the *in vitro* experimentally measured fiber lengths (Table 4.2.2) (Holzapfel et al. 2005). For the L2-L3 joint, the ventral internal (Vi) region was the

only region that did not fall within the standard deviation of the *in vitro* measured fiber lengths of the L1-L2. The deviation in fiber lengths is most notably due to the variation in the contours of the surface of the vertebral endplate; however, within our study we assumed that the endplate surface was flat. Although the experimental data did not agree with the L4-L5 fiber lengths, we can expect that there would be an increase in fiber length in the ventral region and the decrease in length in the dorsal region when compared to the L2-L3 due to an increase in relative vertebral inclination of the L4-L5 joint. Regional variation in orientation and fiber angle also revealed that the fiber elements in the posterior region are shorter than those in the anterior region. Therefore, for the same range of rotational displacements, larger strains are seen in the posterior fiber elements resulting in a faster response of the strain-dependent behavior relative to anterior fiber elements. This was especially apparent for the vertical posture.

Bulging of the IVD due to an axial compressive load was estimated by assuming that the IVD is an incompressible fluid within a cylinder. This assumption was based on previous IVD models in which they modeled the nucleus pulposus as an incompressible fluid (Shirazi-Adl 1989; Shirazi-Adl et al. 1986; Shirazi-Adl et al. 1984). The model seems to compare well to previously reported annular bulges found within the literature (Table 4.4.2) (Reuber et al. 1982; Wenger and Schlegel 1997).

To predict experimental load deformation data, Gardner-Morse *et al.* (2004) experimental 6x6 stiffness matrix data was obtained from the literature and a linear regression was used to model the change in stiffness with preload displacement. Gardner-Morse *et al.* (2004) experimentally reported this trend to be highly significant ($p<0.01$). After determining how the stiffness changes with preload displacement, we predicted the three-dimensional IVD behavior with a displacement dependent variation of Hooke's law. This allowed us to approximate the collinear and coupled load interactions associated with various displacement and rotations of the IVJ. While Hooke's law can not fully describe IVJ behavior within the entire physiologic range, within the linear range it provides a good guideline for building a three-dimensional IVJ model.

The current study was compared to the experimentally predicted data by applying a least squares optimization routine. The optimization routine allows us to tune the regional variations in stiffness of the IVJ by changing the effective area of the lamella fibers at each of the three different preloads. As expected, an increase in preload displacements increased the effective area due to an increase in contact area of the facet joint. A linear regression was applied to our model to account for the increase in effective area at higher preload displacements.

The sum of the RMS error associated with each loading condition was used to compare posture differences to experimentally predicted data within the linear range of motion. Results from the three-dimensional response of IVD indicate that the lordotic posture is better at predicting the axial compressive response of the IVJ. For the L2-L3 joint, the lordotic posture was best at predicting the collinear and coupled forces associated in anterior-posterior directions and the collinear and coupled moments associated lateral flexion, and torsion. However, the sum of the RMS error associated

with force and moments for the other loading conditions were within the same order of magnitude. For the L4-L5 joint, the lordotic posture was best at predicting all of the collinear and coupled forces. When predicting the collinear and coupled moments, the lordotic posture was best at predicting torsion only. However, the sum of RMS error indicates that the posture differences for flexion/extension and lateral flexion are within 2 N-m of each other. These results suggest that normal lordotic posture is better at predicting the three-dimensional behavior of the IVD.

Several limitations must be addressed before considering this analysis. Experimental evidence shows that the intact specimens have a bilinear load-displacement relationship for flexion-extension, A-P shear and axial displacements (Gardner-Morse and Stokes 2004). However, the bilinear behavior was not predicted because the experimental stiffness coefficients were linearized. Furthermore, tension of the IVD was not modeled in this study. Moreover, only quasi-static external displacements can be considered because rate dependence has yet to be included within this model. Facet joint and vertebral ligament interaction was not directly included. However, it was modeled indirectly through optimization of the effective area. The model's response to extension and flexion suggest that facet joint interaction should be included within this model. Ligaments are also an important component to the IVJ. Although, they have not directly been included in the model presented in this research paper, future studies may want to include the ligaments.

Despite these limitations, an efficient and novel method for modeling the three-dimensional behavior of the IVJ has been presented. This model describes the regional variation in angle and length of the lamella fibers. Additionally, a simple model for describing the fiber bulge has been presented. Results suggest that modeling the IVJ with a normal lordotic posture may be advantageous. However, a more thorough experimental validation of the three-dimensional model is required to fine tune the parameters and to confirm the findings within this study.

Chapter 5: Conclusion

The present study provides a novel method for modeling the viscoelastic deformation and the three-dimensional behavior of the IVJ using nonlinear lumped-parameter models. These models were developed to help satisfy a need for computationally-efficient models of the IVD for use in musculoskeletal spine models.

The SNS model was able to predict the dynamic modulus of the IVD at all frequencies tested. Furthermore, the SNS model was able to quantitatively predict the load relaxation at a frequency of 0.01 Hz. However, model performance was unsatisfactory when predicting load relaxation and hysteresis at higher frequencies (0.1 Hz and 1 Hz). These results suggest that the standard solid model of the lumbar IVD may require strain-dependent elastic and viscous behavior to represent the dynamic response to compressive strain.

The SNS model was expanded to three-dimensions by adding two concentric layers of nonlinear lumped-parameter annulus fibers in parallel with the axial element. Each fiber geometry and orientation represents the regional variations in stiffness and the physiologic fiber angle reported in the literature, respectively. Results suggest that normal lordotic posture may be important when modeling IVJ behavior.

The most pronounced limitation within this study is the lack of experimental data to verify the results presented in this study. Therefore, extensive experimental validation is required and encouraged before any future investigations are performed. Furthermore, this study is an initial attempt at modeling a very complex joint. As a result, this study is limited to the tissues and conditions discussed within. However, further studies will add more toward an overall description of the dynamic and three-dimensional behavior of the spine. The final paragraphs highlight important limitations of this study that should be considered for future work.

Although the current study indirectly models the ligament and facet joint interaction of the IVJ, the results showed that the flexion/extension moment was underestimated for all postures and segmental levels within the linear range of motion. The need was even more pronounced when the spine was oriented in its normal lordotic posture. Therefore, the three-dimensional model would greatly benefit by adding ligaments and facet joints. Several researchers have suggested various methods and the importance of modeling the facet joint interaction of the IVJ (Gardner-Morse and Stokes 2004; Shirazi-Adl 1994; Shirazi-Adl et al. 1986; Yang and King 1984). Moreover, it has been shown experimentally that at the limit of flexion the capsular ligaments offer a considerable amount of resistance (Adams et al. 1980).

Stability in the general sense is often demonstrated by causing a small disturbance to the equilibrium position of a system, such as a ball rolling on a surface. If the ball is disturbed and it returns to its equilibrium position then the system is said to be stable. If the ball rolls away the system is said to be unstable (Pilkey and Wunderlich 1994; Reeves et al. 2007).

However, for the purposes of studying the instabilities of the spinal column, a better example of instability can be seen in the buckling of a column. In this problem, it is important to determine a characteristic that defines the point at which the column in equilibrium is no longer stable. The characteristic that best defines the point of instability is known as the critical load or buckling load (Pilkey and Wunderlich 1994). The buckling load of a column tends to be significantly smaller than the failure load of the material (Crisco and Panjabi 1992). However, at the critical load, a very small disturbance in applied force (i.e. lateral force) will cause the structure to become unstable and as a consequence will cause a large displacement in relation to the applied load. Clinically, instabilities to the spinal column have led to hyperextension of the soft tissues in the spine which can results in injury (Reeves et al. 2007). Therefore, it is paramount that researchers rigorously work on defining the stability of the spine.

Several studies have revealed the importance of muscles in stabilizing the spine (Crisco and Panjabi 1991; Franklin and Granata 2006; Moorhouse and Granata 2007) Bogduk, Bergmark, Moorhouse 2007, Franklin 2007]. However, the stabilizing role of the IVD within these models has nearly been neglected. Only a few studies have attempted modeling passive mechanical stability of the IVJ (Crisco and Panjabi 1992; Lucas and Bresler 1961; Wilder 1985). Therefore, future work should focus on testing passive mechanical stability of the IVD and whole ligamentous spine. The author recommends testing stability using Jacobian matrix theory (Franklin and Granata 2006).

Evidence demonstrates that dynamic lifting is three times more likely to contribute to LBP compared with static awkward posture (Bigos et al. 1986). The three-dimensional model within this study is limited because it does not include the dynamic components that are important in estimating the motion of the spine due to creep deformation and bending. Furthermore, it has been suggested that creep during flexion postures may increase risk of low back pain by contributing to disturbance in neuromuscular control (Solomonow et al. 1999). Therefore, damping should be added to the fibers and a detailed muscle model should be added to assess IVJ dynamics.

References

Adams, M. A., Hutton, W. C., and Stott, J. R. (1980). "The resistance to flexion of the lumbar intervertebral joint." *Spine*, 5(3), 245-53.

An, Y. H., and Draughn, R. A. (2000). *Mechanical testing of bone and the bone-implant interface*, CRC Press, Boca Raton, Fla.

Andersson, G. B. (1981). "Epidemiologic aspects on low-back pain in industry." *Spine*, 6(1), 53-60.

Argoubi, M., and Shirazi-Adl, A. (1996). "Poroelastic creep response analysis of a lumbar motion segment in compression." *J Biomech*, 29(10), 1331-9.

Arjmand, N., and Shirazi-Adl, A. (2006). "Model and in vivo studies on human trunk load partitioning and stability in isometric forward flexions." *J Biomech*, 39(3), 510-21.

Berkson, M. H., Nachemson, A., and Schultz, A. B. (1979). "Mechanical-Properties of Human Lumbar Spine Motion Segments .2. Responses in Compression and Shear - Influence of Gross Morphology." *Journal of Biomechanical Engineering-Transactions of the Asme*, 101(1), 53-57.

Bernard, B. P. (1997). "Musculoskeletal Disorders and Workplace Factors: A Critical Review of Epidemiologic Evidence for Work-Related Musculoskeletal Disorder of the Neck, Upper Extremity, and Low Back." National Institute for Occupational Safety and Health.

Bigos, S. J., Spengler, D. M., Martin, N. A., Zeh, J., Fisher, L., Nachemson, A., and Wang, M. H. (1986). "Back injuries in industry: a retrospective study. II. Injury factors." *Spine*, 11(3), 246-51.

Bogduk, N., Amevo, B., and Pearcy, M. (1995). "A biological basis for instantaneous centres of rotation of the vertebral column." *Proc Inst Mech Eng [H]*, 209(3), 177-83.

Burns, M. L., Kaleps, I., and Kazarian, L. E. (1984). "Analysis of compressive creep behavior of the vertebral unit subjected to a uniform axial loading using exact parametric solution equations of Kelvin-solid models--Part I. Human intervertebral joints." *J Biomech*, 17(2), 113-30.

Campbell-Kyureghyan, N. H. (2004). "Computational Analysis of the Time-Dependant Biomechanical Behavior of the Lumbar Spine," Dissertation, Ohio State University.

Chen, J., and Katona, T. R. (1999). "The limitations of the instantaneous centre of rotation in joint research." *J Oral Rehabil*, 26(4), 274-9.

Chen, Y. L. (2000). "Predicting the vertebral inclination of the lumbar spine." *Ergonomics*, 43(6), 744-51.

Cheung, J. T., Zhang, M., and Chow, D. H. (2003). "Biomechanical responses of the intervertebral joints to static and vibrational loading: a finite element study." *Clin Biomech (Bristol, Avon)*, 18(9), 790-9.

Crisco, J. J., 3rd, and Panjabi, M. M. (1991). "The intersegmental and multisegmental muscles of the lumbar spine. A biomechanical model comparing lateral stabilizing potential." *Spine*, 16(7), 793-9.

Crisco, J. J., and Panjabi, M. M. (1992). "Euler Stability of the Human Ligamentous Lumbar Spine. Part 1: Theory." *Clinical Biomechanics*, 7, 19-26.

Edwards, W. T., Hayes, W. C., Posner, I., White, A. A., 3rd, and Mann, R. W. (1987). "Variation of lumbar spine stiffness with load." *J Biomech Eng*, 109(1), 35-42.

Edwards, W. T., Ordway, N. R., Zheng, Y., McCullen, G., Han, Z., and Yuan, H. A. (2001). "Peak stresses observed in the posterior lateral anulus." *Spine*, 26(16), 1753-9.

Franklin, T. C., and Granata, K. P. (2006). "Role of reflex gain and reflex delay in spinal stability-A dynamic simulation." J Biomech.

Fung, Y. C. (1993). *Biomechanics : mechanical properties of living tissues*, Springer-Verlag, New York.

Gardner-Morse, M. G., and Stokes, I. A. (2004). "Structural behavior of human lumbar spinal motion segments." *J Biomech*, 37(2), 205-12.

Holmes, A. D., and Hukins, D. W. (1996). "Analysis of load-relaxation in compressed segments of lumbar spine." *Med Eng Phys*, 18(2), 99-104.

Holzapfel, G. A., Schulze-Bauer, C. A., Feigl, G., and Regitnig, P. (2005). "Single lamellar mechanics of the human lumbar anulus fibrosus." *Biomech Model Mechanobiol*, 3(3), 125-40.

Iatridis, J. C., Setton, L. A., Weidenbaum, M., and Mow, V. C. (1997). "Alterations in the mechanical behavior of the human lumbar nucleus pulposus with degeneration and aging." *J Orthop Res*, 15(2), 318-22.

Jayson, M. I. V. (1987). *The Lumbar spine and back pain*, Churchill Livingstone, Edinburgh ; New York.

Jensen, C. V., and Bendix, T. (1992). "Spontaneous Movements with Various Seated-Workplace Adjustments." *Clinical Biomechanics*, 7(2), 87-90.

Johannessen, W., Vresilovic, E. J., Wright, A. C., and Elliott, D. M. (2004). "Intervertebral disc mechanics are restored following cyclic loading and unloaded recovery." *Ann Biomed Eng*, 32(1), 70-6.

Kaleps, I., Kazarian, L. E., and Burns, M. L. (1984). "Analysis of compressive creep behavior of the vertebral unit subjected to a uniform axial loading using exact parametric solution equations of Kelvin-solid models--Part II. Rhesus monkey intervertebral joints." *J Biomech*, 17(2), 131-6.

Kasra, M., Shirazi-Adl, A., and Drouin, G. (1992). "Dynamics of human lumbar intervertebral joints. Experimental and finite-element investigations." *Spine*, 17(1), 93-102.

Keller, T. S., and Nathan, M. (1999). "Height change caused by creep in intervertebral discs: a sagittal plane model." *J Spinal Disord*, 12(4), 313-24.

Keller, T. S., Spengler, D. M., and Hansson, T. H. (1987). "Mechanical behavior of the human lumbar spine. I. Creep analysis during static compressive loading." *J Orthop Res*, 5(4), 467-78.

Kelsey, J. L., and Hardy, R. J. (1975). "Driving of motor vehicles as a risk factor for acute herniated lumbar intervertebral disc." *Am J Epidemiol*, 102(1), 63-73.

Kelsey, J. L., and White, A. A., 3rd. (1980). "Epidemiology and impact of low-back pain." *Spine*, 5(2), 133-42.

Kiefer, A., Shirazi-Adl, A., and Parnianpour, M. (1997). "Stability of the human spine in neutral postures." *Eur Spine J*, 6(1), 45-53.

Kittusamy, N. K., and Buchholz, B. (2004). "Whole-body vibration and postural stress among operators of construction equipment: a literature review." *J Safety Res*, 35(3), 255-61.

Koeller, W., Funke, F., and Hartmann, F. (1984). "Biomechanical behavior of human intervertebral discs subjected to long lasting axial loading." *Biorheology*, 21(5), 675-86.

Koeller, W., Muehlhaus, S., Meier, W., and Hartmann, F. (1986). "Biomechanical properties of human intervertebral discs subjected to axial dynamic compression--influence of age and degeneration." *J Biomech*, 19(10), 807-16.

Laible, J. P., Pflaster, D. S., Krag, M. H., Simon, B. R., and Haugh, L. D. (1993). "A poroelastic-swelling finite element model with application to the intervertebral disc." *Spine*, 18(5), 659-70.

Lee, K. K., and Teo, E. C. (2004). "Poroelastic analysis of lumbar spinal stability in combined compression and anterior shear." *J Spinal Disord Tech*, 17(5), 429-38.

Li, S. (1994). "Response of Human Intervertebral Discs to Prolonged Axial Loading and Low Frequency Vibration," University of Illinois at Chicago, IL.

Li, S., Patwardhan, A. G., Amirouche, F. M., Havey, R., and Meade, K. P. (1995). "Limitations of the standard linear solid model of intervertebral discs subject to prolonged loading and low-frequency vibration in axial compression." *J Biomech*, 28(7), 779-90.

Lin, H. S., Liu, Y. K., and Adams, K. H. (1978). "Mechanical response of the lumbar intervertebral joint under physiological (complex) loading." *J Bone Joint Surg Am*, 60(1), 41-55.

Lockett, F. J. (1972). *Nonlinear viscoelastic solids*, Academic Press, London, New York,.

Lucas, D. B., M.D., , and Bresler, B., M.S. (1961). "Stability of the Ligamentous Spine." University of California: Biomechanics Laboratory, San Francisco.

Lucas, G. L., Cooke, F. W., and Friis, E. (1999). *A primer of biomechanics*, Springer, New York.

Markolf, K. L. (1972). "Deformation of the thoracolumbar intervertebral joints in response to external loads: a biomechanical study using autopsy material." *J Bone Joint Surg Am*, 54(3), 511-33.

Markolf, K. L., and Morris, J. M. (1974). "The structural components of the intervertebral disc. A study of their contributions to the ability of the disc to withstand compressive forces." *J Bone Joint Surg Am*, 56(4), 675-87.

Martin, R. B., Sharkey, N. A., and Burr, D. B. (1998). *Skeletal tissue mechanics*, Springer, New York.

Martini, F. H. (2004). "Fundamentals of Anatomy and Physiology." Benjamin Cummings, San Francisco, CA.

Moorhouse, K. M., and Granata, K. P. (2007). "Role of reflex dynamics in spinal stability: Intrinsic muscle stiffness alone is insufficient for stability." *J Biomech*, 40(5), 1058-65.

Natarajan, R. N., Williams, J. R., and Andersson, G. B. (2004). "Recent advances in analytical modeling of lumbar disc degeneration." *Spine*, 29(23), 2733-41.

Oliver, M. J., and Twomey, L. T. (1995). "Extension creep in the lumbar spine." *Clin Biomech (Bristol, Avon)*, 10(7), 363-368.

Ozkaya, N., Nordin, M. (1991). *Fundamentals of Biomechanics: Equilibrium, Motion, and Deformation*, Van Nostrand Reinhold, New York, NY.

Panjabi, M. M., Brand, R. A., Jr., and White, A. A., 3rd. (1976). "Mechanical properties of the human thoracic spine as shown by three-dimensional load-displacement curves." *J Bone Joint Surg Am*, 58(5), 642-52.

Panjabi, M. M., Goel, V. K., Walter, S. D., and Schick, S. (1982). "Errors in the center and angle of rotation of a joint: an experimental study." *J Biomech Eng*, 104(3), 232-7.

Pearcy, M. J., and Bogduk, N. (1988). "Instantaneous axes of rotation of the lumbar intervertebral joints." *Spine*, 13(9), 1033-41.

Pilkey, W. D., and Wunderlich, W. (1994). *Mechanics of structures : variational and computational methods*, CRC, Boca Raton.

Pope, M. H., Wilder, D. G., and Magnusson, M. L. (1999). "A review of studies on seated whole body vibration and low back pain." *Proceedings of the Institution of Mechanical Engineers Part H-Journal of Engineering in Medicine*, 213(H6), 435-446.

Reeves, N. P., Narendra, K. S., and Cholewicki, J. (2007). "Spine stability: the six blind men and the elephant." *Clin Biomech (Bristol, Avon)*, 22(3), 266-74.

Reuber, M., Schultz, A., Denis, F., and Spencer, D. (1982). "Bulging of lumbar intervertebral disks." *J Biomech Eng*, 104(3), 187-92.

Riches, P. E., Dhillon, N., Lotz, J., Woods, A. W., and McNally, D. S. (2002). "The internal mechanics of the intervertebral disc under cyclic loading." *J Biomech*, 35(9), 1263-71.

Russell, G. G., Raso, V. J., Hill, D., and McIvor, J. (1990). "A comparison of four computerized methods for measuring vertebral rotation." *Spine*, 15(1), 24-7.

Shirazi-Adi, A., and Parnianpour, M. (1996). "Stabilizing role of moments and pelvic rotation on the human spine in compression." *J Biomech Eng*, 118(1), 26-31.

Shirazi-Adl, A. (1989). "Strain in fibers of a lumbar disc. Analysis of the role of lifting in producing disc prolapse." *Spine*, 14(1), 96-103.

Shirazi-Adl, A. (1994). "Nonlinear stress analysis of the whole lumbar spine in torsion--mechanics of facet articulation." *J Biomech*, 27(3), 289-99.

Shirazi-Adl, A., Ahmed, A. M., and Shrivastava, S. C. (1986). "A finite element study of a lumbar motion segment subjected to pure sagittal plane moments." *J Biomech*, 19(4), 331-50.

Shirazi-Adl, A., and Parnianpour, M. (1993). "Nonlinear response analysis of the human ligamentous lumbar spine in compression. On mechanisms affecting the postural stability." *Spine*, 18(1), 147-58.

Shirazi-Adl, A., and Parnianpour, M. (1996). "Stabilizing role of moments and pelvic rotation on the human spine in compression." *J Biomech Eng*, 118(1), 26-31.

Shirazi-Adl, S. A., Shrivastava, S. C., and Ahmed, A. M. (1984). "Stress analysis of the lumbar disc-body unit in compression. A three-dimensional nonlinear finite element study." *Spine*, 9(2), 120-34.

Simon, B. R., Wu, J. S., Carlton, M. W., Kazarian, L. E., France, E. P., Evans, J. H., and Zienkiewicz, O. C. (1985). "Poroelastic dynamic structural models of rhesus spinal motion segments." *Spine*, 10(6), 494-507.

Solomonow, M., Hatipkarasulu, S., Zhou, B. H., Baratta, R. V., and Aghazadeh, F. (2003). "Biomechanics and electromyography of a common idiopathic low back disorder." *Spine*, 28(12), 1235-48.

Solomonow, M., He Zhou, B., Baratta, R. V., Lu, Y., Zhu, M., and Harris, M. (2000). "Biexponential recovery model of lumbar viscoelastic laxity and reflexive muscular activity after prolonged cyclic loading." *Clin Biomech (Bristol, Avon)*, 15(3), 167-75.

Solomonow, M., Zhou, B. H., Baratta, R. V., Lu, Y., and Harris, M. (1999). "Biomechanics of increased exposure to lumbar injury caused by cyclic loading: Part 1. Loss of reflexive muscular stabilization." *Spine*, 24(23), 2426-34.

Spengler, D. M., Bigos, S. J., Martin, N. A., Zeh, J., Fisher, L., and Nachemson, A. (1986). "Back injuries in industry: a retrospective study. I. Overview and cost analysis." *Spine*, 11(3), 241-5.

Tencer, A. F., Ahmed, A. M., and Burke, D. L. (1982). "Some static mechanical properties of the lumbar intervertebral joint, intact and injured." *J Biomech Eng*, 104(3), 193-201.

Throne, J. L., Progelhof, R.C. (1988). *Engineering Properties of Polymers*, Hanser Publishers, Sherwood Technologies, Inc.

Twomey, L., and Taylor, J. (1982). "Flexion creep deformation and hysteresis in the lumbar vertebral column." *Spine*, 7(2), 116-22.

van Deursen, L. L., Patijn, J., Durinck, J. R., Brouwer, R., van Erven-Sommers, J. R., and Vortman, B. J. (1999). "Sitting and low back pain: the positive effect of rotatory dynamic stimuli during prolonged sitting." *European Spine Journal*, 8(3), 187-193.

Wang, J. L., Parnianpour, M., Shirazi-Adl, A., Engin, A. E., Li, S., and Patwardhan, A. (1997). "Development and validation of a viscoelastic finite element model of an L2/L3 motion segment." *Theoretical and Applied Fracture Mechanics*, 28(1), 81-93.

Wenger, K. H., and Schlegel, J. D. (1997). "Annular bulge contours from an axial photogrammetric method." *Clin Biomech (Bristol, Avon)*, 12(7-8), 438-444.

Wilder, D. G. (1985). "On Loading of the Human Lumbar Intervertebral Motion Segment," Dissertation, University of Vermont, Burlington, VT.

Wilder, D. G., Pope, M. H., and Frymoyer, J. W. (1988). "The biomechanics of lumbar disc herniation and the effect of overload and instability." *J Spinal Disord*, 1(1), 16-32.

Wilder, D. G., Woodworth, B. B., Frymoyer, J. W., and Pope, M. H. (1982). "Vibration and the human spine." *Spine*, 7(3), 243-54.

Yang, K. H., and King, A. I. (1984). "Mechanism of facet load transmission as a hypothesis for low-back pain." *Spine*, 9(6), 557-65.

Yoshioka, T., Tsuji, H., Hirano, N., and Sainoh, S. (1990). "Motion characteristic of the normal lumbar spine in young adults: instantaneous axis of rotation and vertebral center motion analyses." *J Spinal Disord*, 3(2), 103-13.

Appendix A: How to Run the Programs

A.1. SNS Model Programs

The following programs were used to determine the material properties, solve the SNS model, and compare the solution of the SNS to the SLS model.

A.1.1. Calculating Strain-Dependent Modulus. The Matlab program *Morse_Stiff_Stress.m* was written to normalize the experimental stiffness data, determine the strain-dependent modulus, and plot the instantaneous stress response of the IVD (Mat. Code A.1.1).

Matlab Code A.1.1. *Morse_Stiff_Stress.m*

```
%Kevin Groth
%Virginia Tech
%Fall 2006
%Plots Gardner-Morse et al. [2004] Normalized Stiffness Coefficients and Stress
close all; clear all; clc
H = 8.9;
area = 1161;
z=[0; 0.1471; 0.2066];
e=z/H;
k2=[438; 1700; 2420];
E2=(k2.*H)./area;
plot(e,E2,'x')
[P,f]=polyfit(e,E2,1)
MSf=[e,E2]
figure
plot(e,E2,'xk')
xlabel('Compressive Strain, e ')
ylabel('Elastic Modulus, E_2 [N/mm^2]')
legend('Gardner-Morse et al. (2004)')
grid on
corrcoef([e,E2])
e=0:0.0001:.05
E2=P(1).*e+P(2)
S=e.*E2
figure
plot(e,S);
xlabel('Strain, e')
ylabel('Stress, S [MPa]')
MSs=[e',S']
csvwrite('Morse_Stokes_Fit.csv',MSf)
csvwrite('Morse_Stokes_Stress.csv',MSs)
break
```

A.1.2. Calculating the Constant Parameters. The program *Opt_Relax_Coef.m* determines the constant parameters of the SNS. This program optimizes the model parameters between the predicted stress (Eq. 3.5) and Holmes *et al.* experimental stress relaxation experiment by calling on the function *Fun_Relax.m* (Mat. Codes A.1.2 & A.1.3) (Holmes and Hukins 1996). To visualize the results from the optimization you can use *Plot_Relax.m* (Mat. Code A.1.4).

Matlab Code A.1.2. *Opt_Relax_Model_Coef.m*

```
%Kevin Groth
%Virginia Tech
%Fall 2006
%Optimization of material property parameters for the stress relaxation experiment
close all;clear all;clc
[So,Po]=posture(1);
[V,IVD,NUC,Or,dOr,RBV,dRBV,COM,dCOM,Gl,Gr,IVD_prop,H,NIVD,NL,NF,NP,Xi,Xs,IVDo,IVDa,dIVDa,IVD
L,dIVDL,NUCo,NUCa,dNUCa,NUCN,dNUCN]=para(So,Po);
[Holmes]=xlsread('Holmes_relax.xls');
area=IVD_prop(12);
%Define parameters for optimization
Co=[1;1];                                          %Initial guess
lb=[-1E6;-1E6];                                    %Lower bound
ub=[];                                              %Upper bound
options=optimset('Display','iter','LargeScale','off','MaxIter',1E6,'MaxFunEvals',1E4,'TolFun',1E-
6,'TolX',1E-6);          % Sets optimization options
[C,fval]=fmincon(@fun3_norm,Co,[],[],[],[],lb,ub,[],options,area,H,Holmes)
%%%%%%%%%End of Program%%%%%%%%%%%%%%%%%%%%%%%%%%%%%%
```

Matlab Code A.1.3. *Fun_Relax.m*

```
%Kevin Groth
%Virginia Tech
%Fall 2006
%Function for optimization of material property parameters for the stress relaxation
%experiment
function [f]=Fun_Relax(C,area,H,Holmes)
eo=0.0417;      % Strain that causes the S= 2050/.00165 [Pa]
t1=0;
t=Holmes(:,1);
P =1.0e+002 *[6.41378109529765   0.03150455252881];
E1=C(1)*10^6;
E2=(P(1)*eo+P(2))*10^6;
u=C(2)*10^9;
b=u;
so=E2*eo;
p1=(u./(E1+E2));
qo=(E1.*E2)./(E1+E2);
q1=(E2.*u)./(E1+E2);
s1=eo.*qo+exp(p1.^(-1).*((-1).*t+t1)).*((-1).*eo.*qo+so);
area=.001650;
s2=Holmes(:,2)/area;
f=(sum((s1-s2).^2));
%%%%%%%%%End of Program%%%%%%%%%%%%%%%%%%%%%%%%%%%%%%
```

Matlab Code A.1.4. *Plot_Relax..m*

```
%Kevin Groth
%Virginia Tech
%Fall 2006
%Plots Paramters Determined in Opt_Relax_Model_Coef.m
close all;clc;clear all;
[So,Po]=posture(1);
[V,IVD,NUC,Or,dOr,RBV,dRBV,COM,dCOM,Gl,Gr,IVD_prop,H,NIVD,NL,NF,NP,Xi,Xs,IVDo,IVDa,dIVDa,IVD
L,dIVDL,NUCo,NUCa,dNUCa,NUCN,dNUCN]=para(So,Po);
area=IVD_prop(12)
[Holmes]=xlsread('Holmes_relax.xls');
eo=0.0417; %% Strain that causes the S= 2050/.00165 [Pa]
t1=0;
P =1.0e+002 *[6.41378109529765   0.03150455252881];
E2=(P(1)*eo+P(2))*10^6;
so =E2*eo;
for i=1:length(Holmes)
   t(i)=Holmes(i,1);
```

```
    e(i)=eo;
    P =1.0e+002 *[6.41378109529765   0.03150455252881];
    E2(i)=(P(1)*eo+P(2))*10^6;
    E1(i)=8.96*10^6;
    u(i)=102.3*10^9;
    p1(i)=(u(i)./(E1(i)+E2(i)));
    qo(i)=(E1(i).*E2(i))./(E1(i)+E2(i));
    q1(i)=(E2(i).*u(i))./(E1(i)+E2(i));
    s(i)=eo.*qo(i)+exp(p1(i).^(-1).*((-1).*t(i)+t1)).*((-1).*eo.*qo(i)+so);
end
s1=s/10^6
area=0.00165;
s2=(Holmes(:,2)/area)/10^6;
figure
hold on
plot(Holmes(:,1),s1,'-')
plot(Holmes(:,1),s2,'x')
xlabel('Time, t [s]')
ylabel('Stress, S [MPa]')
grid on
maxerror=max(abs((s1'-s2)./(s2)))
avgerror=(sum(abs((s1'-s2)./(s2))))/length(s1')
corrcoef([s1',s2])
HR=[Holmes(:,1),s1',s2]
csvwrite('Holmes_Relax_Fit.csv',HR)
%%%%%%%%%%End of Program%%%%%%%%%%%%%%%%%%%%%%%%%%%%%%%%%%%%
```

A.1.3. Solving the Cyclic Relaxation. Once all the parameters are calibrated, run *Solve_Cyclic_Relaxation.m* to solve the cyclic relaxation of the SLS and SNS models (Mat. Code A.1.5). In addition, this program calculates the cyclic relaxation, the dynamic modulus, and the hysteresis of the IVD.

Matlab Code A.1.5. *Solve_Cyclic_Relaxtion.m*

```
%Kevin Groth
%Virginia Tech
%Fall 2006
%Solves cyclic stress relaxation of the SLS and SNS
close all; clear all; clc;
%%Sets stress relaxation conditions
cycles=30;          %Number of displacement cycles
f=1                 %Frequency of displacement cycles [Hz]
dt=.001;            %Time increment
w=2*pi*f;           %Driving frequency   [Hz]
%%Time
ti=0;               %Initial Time [s]
tf=cycles/f;        %Final Time [s]
t=ti:dt:tf;         %Time interval
%%SLS Parameters and Initial Conditions [Li 1994, Li 1995]
H=.00964;           %Height of IVD [m]
area=.00165;        %Area of IVD  [m^2]
F=426;              %Initial Preload [N]
so=F/area;          %Initial Stress [Pa]
E2=5.06E6;          %Modulus of series spring
e1=so/E2;           %Initial Strain
d=100E-6;           %Maximum Displacement [m]
ein=d/H;            %Strain Input
eo=ein/2;
%%Solves the SLS differential equation
[t1,s1]=ode23(@Fun_SLS,t,so,[],H,area,eo,e1,w);    %SLS Model
ecyc1=(eo.*(1-cos(w.*t1)))+e1;   %Cyclic Strain
z1=ecyc1.*H.*1000;               %Cyclic Displacement
z1min=min(z1);                   %Minimum Displacement
force1=s1*area;                  %Calculated Force Relaxation
Kd1=force1./z1;                  %Stiffness
%%SNS Parameters and Initial Conditions [Li 1995]
```

```
H = 0.0089;           %Height of IVD [m]        [Gardner-Morse 2004]
area = 0.001161;    %Area of IVD  [m^2]      [Gardner-Morse 2004]
F=426;                 %Initial Preload [N]
so=F/area;             %Initial Stress [Pa]
k=2216.99*1000;     %Stiffness at Preload, k [N/m]
x1=F/k;                %Initial Preload Displacement [m]
e1=x1/H;               %Initial Preload Strain
d=100E-6;              %Peak to Peak displacement
ein=d/H;               %Peak to Peak strain input  1.1% (S.D. 0.2)
eo=ein/2;              %Half the peak to peak strain input
%%Solves the SNS differential equation
[t2,s2]=ode23(@Fun_SNS,t,so,[],H,area,eo,e1,w); %Linear k2, Constant k1, Constant b
ecyc2=(eo.*(1-cos(w.*t2)))+e1;   %Cyclic Strain
z2=ecyc2.*H.*1000;               %Cyclic Displacement
force2=s2*area;                  %Calculated Force Relaxation
Kd2=force2./z2;                  %Stiffness
figure
plot(t1,z1-z1min,'.')
xlabel('Time, t [s]')
ylabel('Displacement, z [mm]')
%%Plots Modulus vs time
Ed1=s1./ecyc1;
Ed2=s2./ecyc2;
%
% figure(1)
% plot(t1,Ed1)
% figure(2)
% plot(t2,Ed2,'r')
figure(10)
z1int=z1(((cycles-3)*1000+1):((cycles)*1000+1));
force1int=force1(((cycles-3)*1000+1):((cycles)*1000+1));
[z1min,i]=min(z1int);
[force1min,i]=min(force1int);
plot( z1int-z1min,force1int-force1min);
[P1,f]=polyfit( z1int,force1int,1);
%%Modulus
Modulus_SLS=(mean(Ed1((cycles-1)*1000+1:(cycles)*1000+1)))/10^6
% Stiff_SLS=(mean(Kd1((cycles-1)*1000+1:(cycles)*1000+1)))
%%Hysteresis
c1=cumtrapz(z1int(1:502),force1int(1:502));
c2=abs(cumtrapz(z1int(502:1001),force1int(502:1001)));
c=c1(length(c1))-c2(length(c2));
Hyst(1)=c/c1(length(c1));
c1=cumtrapz(z1int(1001:1502),force1int(1001:1502));
c2=abs(cumtrapz(z1int(1502:2001),force1int(1502:2001)));
c=c1(length(c1))-c2(length(c2));
Hyst(2)=c/c1(length(c1));
c1=cumtrapz(z1int(2001:2502),force1int(2001:2502));
c2=abs(cumtrapz(z1int(2502:3001),force1int(2502:3001)));
c=c1(length(c1))-c2(length(c2));
Hyst(3)=c/c1(length(c1));
Hyst_SLS=mean(Hyst)
%%Relaxation Index
relaxindex_SLS=(force1(1)-(force1(length(force1))))./force1(1)
%%SNS Calculations
hold on
n=3;
z2int=z2((cycles-n)*1000+1:(cycles)*1000+1);
force2int=force2((cycles-n)*1000+1:(cycles)*1000+1);
[z2min,i]=min(z2int);
[force2min,i]=min(force2int);
plot( z2int-z2min,force2int-force2min);
%%Modululus
Modulus2=(mean(Ed2((cycles-1)*1000+1:(cycles)*1000+1)))/10^6;
Modulus_SNS=Modulus2
% Stiff_SNS=(mean(Kd2((cycles-1)*1000+1:(cycles)*1000+1)))
%%Hysteresis
c1=cumtrapz(z2int(1001:1502),force2int(1001:1502));
c2=abs(cumtrapz(z2int(1502:2001),force2int(1502:2001)));
c=c1(length(c1))-c2(length(c2));
```

```
Hyst(2)=c/c1(length(c1));
c1=cumtrapz(z2int(2001:2502),force2int(2001:2502));
c2=abs(cumtrapz(z2int(2502:3001),force2int(2502:3001)));
c=c1(length(c1))-c2(length(c2));
Hyst(3)=c/c1(length(c1));
Hyst_SNS=mean(Hyst)
%%Relaxation Index
relaxindex_SNS=(force2(1)-(force2(length(force2)))./force2(1)
figure(100)
hold on
plot(t1,force1,'k')
plot(t2,force2,'--')
xlabel('Time, t [s]')
ylabel('Force, F [N]')
FR=[t1,force1,t2,force2];
csvwrite('Force_Relaxation_Compare.csv',FR)
%%%%%%End of Program%%%%%%%%%%%%%%%%%%%
```

A.2. Three-dimensional Spine Model Programs

A.2.1. Calculating Element Insertion Points. In order to run the IVD model, the IVD parameters must first be chosen. These can be set in the Excel spread sheet *IVD properties.xls* (Fig. A.2.1). In *IVD properties.xls*, you can set the lateral width, anterior-posterior width, fiber layer (level) distance, number of IVDs, number of layers (levels), number of fibers, and area of the disc. Each of the parameters has a variable name, numerical value, description, and an associated reference with them. Note that lamella fiber thickness, fiber width and height of vertebra are not used, but have been added merely as a reference. To load these values into any Matlab file you can use the Matlab command *xlsread.m*.

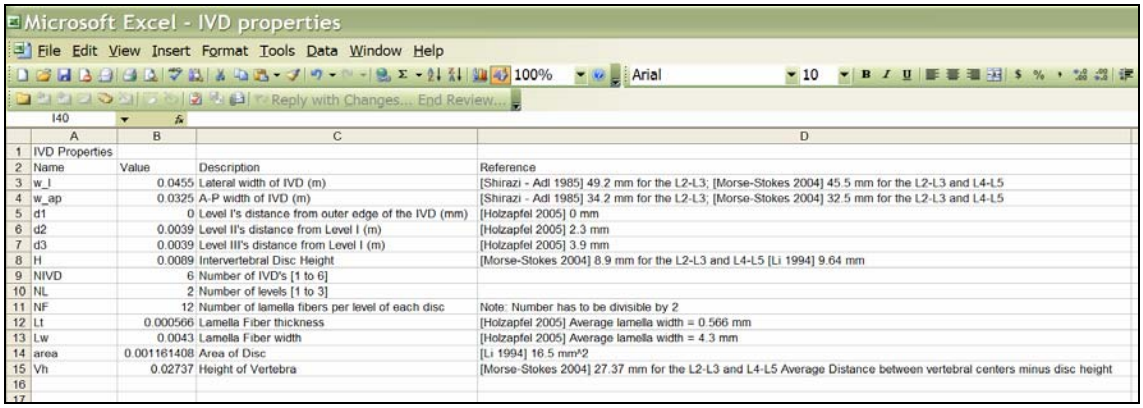

	A	B	C	D
1	IVD Properties			
2	Name	Value	Description	Reference
3	w_l	0.0455	Lateral width of IVD (m)	[Shirazi - Adl 1985] 49.2 mm for the L2-L3; [Morse-Stokes 2004] 45.5 mm for the L2-L3 and L4-L5
4	w_ap	0.0325	A-P width of IVD (m)	[Shirazi - Adl 1985] 34.2 mm for the L2-L3; [Morse-Stokes 2004] 32.5 mm for the L2-L3 and L4-L5
5	d1	0	Level I's distance from outer edge of the IVD (mm)	[Holzapfel 2005] 0 mm
6	d2	0.0039	Level II's distance from Level I (m)	[Holzapfel 2005] 2.3 mm
7	d3	0.0039	Level III's distance from Level I (m)	[Holzapfel 2005] 3.9 mm
8	H	0.0089	Intervertebral Disc Height	[Morse-Stokes 2004] 8.9 mm for the L2-L3 and L4-L5 [Li 1994] 9.64 mm
9	NIVD	6	Number of IVD's [1 to 6]	
10	NL	2	Number of levels [1 to 3]	
11	NF	12	Number of lamella fibers per level of each disc	Note: Number has to be divisible by 2
12	Lt	0.000566	Lamella Fiber thickness	[Holzapfel 2005] Average lamella width = 0.566 mm
13	Lw	0.0043	Lamella Fiber width	[Holzapfel 2005] Average lamella width = 4.3 mm
14	area	0.001161408	Area of Disc	[Li 1994] 16.5 mm^2
15	Vh	0.02737	Height of Vertebra	[Morse-Stokes 2004] 27.37 mm for the L2-L3 and L4-L5 Average Distance between vertebral centers minus disc height
16				
17				

Figure A.2.1. *IVD properties.xls.*

To set the geometry and position of each vertebra as well as some other parameters, you must use the Excel spreadsheet *properties.xls* (Fig. A.2.2) (Franklin and Granata 2006). In *properties.xls*, you can set position of the center of mass (COM), lateral width, anterior-posterior width, and height of each vertebra relative to the body coordinate system. Note that gravity and mass are not used in the current study's model. However, these properties will be needed if dynamics is added to the model.

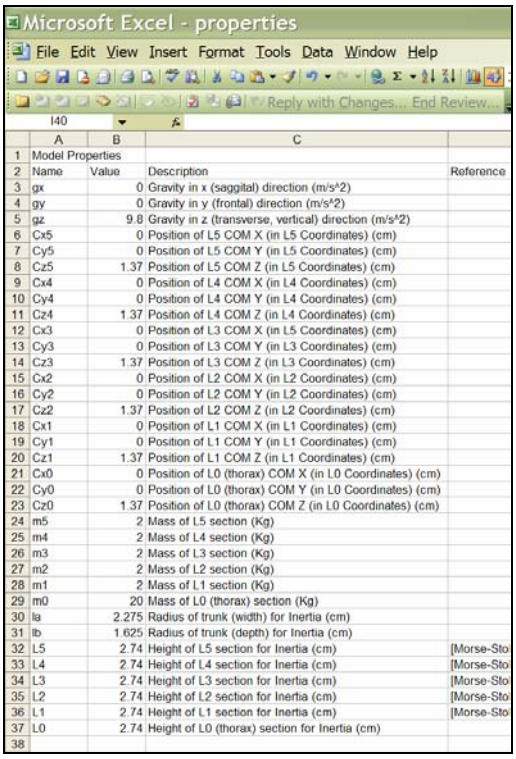

Microsoft Excel - properties

File Edit View Insert Format Tools Data Window Help

Reply with Changes... End Review...

I40

	A	B	C	
1	Model Properties			
2	Name	Value	Description	Reference
3	gx	0	Gravity in x (saggital) direction (m/s^2)	
4	gy	0	Gravity in y (frontal) direction (m/s^2)	
5	gz	9.8	Gravity in z (transverse, vertical) direction (m/s^2)	
6	Cx5	0	Position of L5 COM X (in L5 Coordinates) (cm)	
7	Cy5	0	Position of L5 COM Y (in L5 Coordinates) (cm)	
8	Cz5	1.37	Position of L5 COM Z (in L5 Coordinates) (cm)	
9	Cx4	0	Position of L4 COM X (in L4 Coordinates) (cm)	
10	Cy4	0	Position of L4 COM Y (in L4 Coordinates) (cm)	
11	Cz4	1.37	Position of L4 COM Z (in L4 Coordinates) (cm)	
12	Cx3	0	Position of L3 COM X (in L5 Coordinates) (cm)	
13	Cy3	0	Position of L3 COM Y (in L3 Coordinates) (cm)	
14	Cz3	1.37	Position of L3 COM Z (in L3 Coordinates) (cm)	
15	Cx2	0	Position of L2 COM X (in L2 Coordinates) (cm)	
16	Cy2	0	Position of L2 COM Y (in L2 Coordinates) (cm)	
17	Cz2	1.37	Position of L2 COM Z (in L2 Coordinates) (cm)	
18	Cx1	0	Position of L1 COM X (in L1 Coordinates) (cm)	
19	Cy1	0	Position of L1 COM Y (in L1 Coordinates) (cm)	
20	Cz1	1.37	Position of L1 COM Z (in L1 Coordinates) (cm)	
21	Cx0	0	Position of L0 (thorax) COM X (in L0 Coordinates) (cm)	
22	Cy0	0	Position of L0 (thorax) COM Y (in L0 Coordinates) (cm)	
23	Cz0	1.37	Position of L0 (thorax) COM Z (in L0 Coordinates) (cm)	
24	m5	2	Mass of L5 section (Kg)	
25	m4	2	Mass of L4 section (Kg)	
26	m3	2	Mass of L3 section (Kg)	
27	m2	2	Mass of L2 section (Kg)	
28	m1	2	Mass of L1 section (Kg)	
29	m0	20	Mass of L0 (thorax) section (Kg)	
30	la	2.275	Radius of trunk (width) for Inertia (cm)	
31	lb	1.625	Radius of trunk (depth) for Inertia (cm)	
32	L5	2.74	Height of L5 section for Inertia (cm)	[Morse-Sto
33	L4	2.74	Height of L4 section for Inertia (cm)	[Morse-Sto
34	L3	2.74	Height of L3 section for Inertia (cm)	[Morse-Sto
35	L2	2.74	Height of L2 section for Inertia (cm)	[Morse-Sto
36	L1	2.74	Height of L1 section for Inertia (cm)	[Morse-Sto
37	L0	2.74	Height of L0 (thorax) section for Inertia (cm)	
38				

Figure A.2.2. *properties.xls* (Franklin and Granata 2006).

After setting the spine model properties, you will want to choose a starting posture. Currently, you can select two starting postures (normal lordosis and vertical). To set the posture you will use the Matlab function *posture.m* (Franklin and Granata 2006). This function has been written into the program *element_pos_orient.m* and will need to be set in this program before you can determine the position and orientation of the element (Mat. Code A.2.1). Once all the parameters are set, *element_pos_orient.m* can be run. This program will determine the insertion points in absolute coordinates for the nucleus and lamella fiber elements. Note that if you would like to find insertion point for only one segmental level, you will need to choose the number of IVD's up to that level in *IVD propeteris.xls* and change 'level' to the segmental level of interest in *element_pos_orient.m.* However, for all other programs you will need to choose one IVD in *IVD properties.xls*.

This matrix of information is then stored in two separate files (*InsertionPoints.csv* and *Nucleus.csv*). *InsertionPoints.csv* is the nodal position of the lamella elements (Fig. A.2.3) and *Nucleus.csv* is the nodal position of the nucleus elements. Note that column A is the number of nodes per element, columns B and F tells you which body the node is referenced from, column C-E and G-I are the x, y, and z coordinates, respectively, referenced to their corresponding bodies.

Matlab Code A.2.1. *element_pos_orient.m*

```
%%%Calculation of nucleus and lamella fiber position and orientation
%%%Kevin Groth
%%%Virginia Tech
%%%Summer 2006
close all;clear all;clc
```

```
disp(['IVD Model Generation Started:   ' datestr(clock,21)])
starttime=clock;
eps(1)=2^(-64*5)
%Load Initial Conditions
[So,Po]=posture(1); % Do NOT change this lordotic posture(1); used for calculation of insertion points.
[V,IVD,NUC,Or,dOr,RBV,dRBV,COM,dCOM,Gl,Gr,IVD_prop,H,NIVD,NL,NF,NP,Xi,Xs,IVDo,IVDa,dIVDa,IVDL,dIVDL,NUCo,
NUCa,dNUCa,NUCN,dNUCN,area]=para(So,Po);
%Inferior ellipse of IVD, ei
[ei,ei_area,npts]=ellipse3(IVD_prop,NL);
%%%Superior ellipse of IVD, es
[es,es_area,npts]=ellipse3(IVD_prop,NL);
%%%Draws vector r for the purpose of finding intersection points
[r,rmag]=intersecting_vector(IVD_prop,ei);
% hold on
% plot(r(:,1),r(:,2))
%%%Calculation of polar points for inferior disc
[Pi,alpha,rPimag]=polar(NL,NIVD,NP,Xi,r,ei,1,npts);
%%%Calculation of polar points for superior disc
[Ps,alpha,rPsmag]=polar(NL,NIVD,NP,Xs,r,es,2,npts);
%%%Polar points in absolute coordinates
[Or,dOr,RBV,dRBV,COM,dCOM,Gl,Gr] = kinematicsc(So,Po,V);
[Pia,dMa,Len,dLen]=getabsc(Pi,Or,dOr,RBV,dRBV);
[Psa,dMa,Len,dLen]=getabsc(Ps,Or,dOr,RBV,dRBV);
%%%Plot polar points in absolute coordinates
% plot_points(Pia,Psa,NL,NIVD,NP)
% view(-90,0)
%%%Calculation of height of disc at each polar point
[h]=height(Pia,Psa,NL,NIVD,NP,alpha);
%%%Calculate Insertion points at each polar point
[Pi1,Pi2,Ps1,Ps2,L,phi,phi2,dphi]=insertion(Xi,Xs,h,alpha,r,rPimag,ei,NL,NIVD,NP,npts);
%%%Change this posture for plotting
[So,Po]=posture(1);
[Or,dOr,RBV,dRBV,COM,dCOM,Gl,Gr] = kinematicsc(So,Po,V);
%%%Insertion points in absolute coordinates
[Pi1a,dMa,Len,dLen]=getabsc(Pi1,Or,dOr,RBV,dRBV);
[Pi2a,dMa,Len,dLen]=getabsc(Pi2,Or,dOr,RBV,dRBV);
[Ps1a,dMa,Len,dLen]=getabsc(Ps1,Or,dOr,RBV,dRBV);
[Ps2a,dMa,Len,dLen]=getabsc(Ps2,Or,dOr,RBV,dRBV);
%%%Plot insertion points in absolute coordinates
plot_points(Pi1a,Pi2a,NL,NIVD,NP)
plot_points(Ps1a,Ps2a,NL,NIVD,NP)
%%%To find the absolute coordinate for each ellipse of IVD
%%%Inferior ellipse of IVD, ei
[ei]=ellipse_abs(IVD_prop,NIVD,NL,Xi,1);
plot_ellipse(ei,So,Po,V,NL,NIVD)
%%%Superior ellipse of IVD, es
[es]=ellipse_abs(IVD_prop,NIVD,NL,Xs,2);
plot_ellipse(es,So,Po,V,NL,NIVD)
%%%Generate IVD matrix using insertion points of lamella fibers
[IVD]=IVDgen(Pi1,Pi2,Ps1,Ps2,NP,NF,NL,NIVD)
%%%Generate Nucleus matrix
[NUC]=NUCgen(Xi,Xs,NIVD);
csvwrite('InsertionPoints.csv',IVD);
csvwrite('Nucleus.csv',NUC);
%%% Plot spine
drawspine(So,Po,V,IVD,NUC,zeros(size(IVD,1),1),[1,1,.20],[0,0,.20]);
% zoom(10)
xlabel('Right Lateral/Left Lateral [m]')
ylabel('Anterior/Posterior [m]')
zlabel('Superior/Inferior [m]')
disp(['IVD Generation Elapsed Time: ' etimev(clock,starttime)]);
%%%%%%%%%End of Program%%%%%%%%%%%%%%%%%%%%%%%%%%%%%
```

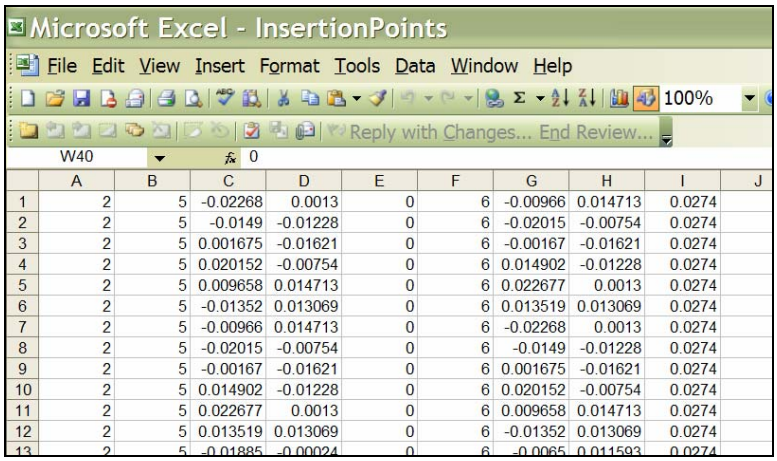

Microsoft Excel - InsertionPoints

File Edit View Insert Format Tools Data Window Help

100%

Reply with Changes... End Review...

W40 0

	A	B	C	D	E	F	G	H	I	J
1	2	5	-0.02268	0.0013	0	6	-0.00966	0.014713	0.0274	
2	2	5	-0.0149	-0.01228	0	6	-0.02015	-0.00754	0.0274	
3	2	5	0.001675	-0.01621	0	6	-0.00167	-0.01621	0.0274	
4	2	5	0.020152	-0.00754	0	6	0.014902	-0.01228	0.0274	
5	2	5	0.009658	0.014713	0	6	0.022677	0.0013	0.0274	
6	2	5	-0.01352	0.013069	0	6	0.013519	0.013069	0.0274	
7	2	5	-0.00966	0.014713	0	6	-0.02268	0.0013	0.0274	
8	2	5	-0.02015	-0.00754	0	6	-0.0149	-0.01228	0.0274	
9	2	5	-0.00167	-0.01621	0	6	0.001675	-0.01621	0.0274	
10	2	5	0.014902	-0.01228	0	6	0.020152	-0.00754	0.0274	
11	2	5	0.022677	0.0013	0	6	0.009658	0.014713	0.0274	
12	2	5	0.013519	0.013069	0	6	-0.01352	0.013069	0.0274	
13	2	5	-0.01885	-0.00024	0	6	-0.0065	0.011593	0.0274	

Figure A.2.3. *InsertionPoints.csv.*

A.2.2 Optimization of Lamella Fiber Area. Calculation of the IVJ stiffness was determined by optimizing the effective area of the lamella fibers. Before running the optimization program *Opt_Fiber_Area.m,* you will want to set the number of IVDs (NIVD) in *IVD_proporties.xls* to 1 (Mat. Code A.2.2). Next, you will want to choose the posture you are interested in and run *element_pos_orient.m.* You are now ready to run *Opt_Fiber_Area.m* to determine the effective area for each fiber (Note: Be sure the posture is correct). This program optimizes the fiber element areas by comparing the force output of the model to the experimental prediction (Gardner-Morse and Stokes 2004).

Matlab Code A.2.2. *Opt_Fiber_Area.m*

```
%Kevin Groth
%Virginia Tech
%Spring 2007
%Optimization program for finding effective area of fibers
close all;clear all;clc
disp(['IVJ Optimization Started:   ' datestr(clock,21)])
starttime=clock;
%%Load Initial Conditions
[So,Po]=posture(2);
[V,IVD,NUC,Or,dOr,RBV,dRBV,COM,dCOM,Gl,Gr,IVD_prop,H,NIVD,NL,NF,NP,Xi,Xs,IVDo,IVDa,dIVDa,IVDL,dIVDL,NUCo,
NUCa,dNUCa,NUCN,dNUCN,area]=para(So,Po);
%Define parameters for optimization
areaLo=[zeros(size(IVD(:,1)))];  %Initial effective area guess for fibers
areaLo(:,1)=(area*(.4))/(NF*NL);
lb=[zeros(size(IVD(:,1)))];
lb(:,1)=((area*(.4))/(NF*NL))/10;
ub=[zeros(size(IVD(:,1)))];
ub(:,1)=((area*(.4))/(NF*NL))*10;
options=optimset('Display','iter','LargeScale','off','MaxIter',1E6,'MaxFunEvals',1E6,'Tolfun',1E-6);          % Sets
optimization options
[areaLo,fval]=fmincon(@Cost_Fiber_Area,areaLo,[],[],[],[],lb,ub,[],options,So,Po,V,IVD,NUC,Or,dOr,RBV,dRBV,COM,dC
OM,Gl,Gr,IVD_prop,H,NIVD,NL,NF,NP,Xi,Xs,IVDo,IVDa,dIVDa,IVDL,dIVDL,NUCo,NUCa,dNUCa,NUCN,dNUCN,area)
%Makes the area of fibers sagittally symetric
areaL=[zeros(size(IVD(:,1)))];
areaL(1:3)=areaLo(1:3);
areaL(4)=areaLo(2);
areaL(5)=areaLo(1);
areaL(6)=areaLo(6);
areaL(7:12)=areaL(1:6);
areaL(13:15)=areaLo(13:15);
areaL(16)=areaLo(14);
areaL(17)=areaLo(13);
areaL(18)=areaLo(18);
areaL(19:24)=areaL(13:18);
csvwrite('Fiber Area.csv', areaL)
disp(['IVJ Optimization Elapsed Time: ', etimev(clock,starttime)])
```

A.2.3 External Force Output of IVD Model. After calculating the lamella fiber area, you can check the external force output using the Matlab program *External Forces.m* (Mat. Code A.2.3). This program allows the user to define starting translational/rotational displacement and total translational/rotational displacement. Furthermore, it calculates the root mean square (RMS) between the model predicted force output and the experimentally predicted force output.

Matlab Code A.2.3. *External Forces.m*

```
%Kevin Groth
%Virginia Tech
%Fall 2006
%External IVD Force Program
close all; clear all; clc
[So,Po]=posture(1);
[V,IVD,NUC,Or,dOr,RBV,dRBV,COM,dCOM,Gl,Gr,IVD_prop,H,NIVD,NL,NF,NP,Xi,Xs,IVDo,IVDa,dIVDa,IVD
L,dIVDL,NUCo,NUCa,dNUCa,NUCN,dNUCN,area]=para(So,Po);
%%%Starting translational/rotational displacement
Si=So;
%%Body 0
Si(31)=So(31)-0;
Si(32)=So(32)-0;
Si(33)=So(33)-0.0002066*(0/2);
Si(34)=So(34)-0*(pi/180);
Si(35)=So(35)-0*(pi/180);
Si(36)=So(36)-0*(pi/180);
% Define Total translational/rotational displacement
D=zeros(36,1);
%%Body 0
D(31)=0;                    %X-axis, Medial/Lateral, [m]
D(32)=0;                    %Y-axis, Anterior/Posterior, [m]
D(33)=-0.0002066*(2/2);          %Z-axis, Axial, [m]  D(33) = -.0002066 is the max experimental
displacement [Morse Stokes 2004]
D(34)=0*(pi/180);           %X-axis, (+) for Extension, [degrees]
D(35)=0*(pi/180);           %Y-axis, (+) for Right Lateral Rotation, [degrees]
D(36)=0*(pi/180);           %Z-axis, (+) for Counterclockwise Torsion [degrees]
% %Final Translation/Rotation of Body
Sd=Si;
%%Body 0
Sd(31)=Sd(31)+D(31);              % X-axis, X0
Sd(32)=Sd(32)+D(32);              % Y-axis, Y0
Sd(33)=Sd(33)+D(33);              % Z-axis, Z0
Sd(34)=Sd(34)+D(34);              % X-axis, T0, (+) for Extension
Sd(35)=Sd(35)+D(35);              % Y-axis, B0, (+) for  Right Lateral Rotation
Sd(36)=Sd(36)+D(36);              % Z -axis, A0, (+) for Counterclockwise Torsion
%%Loop Initial Conditions
steps=110;                         %Step increments
dSd=zeros(72,1);                  %Initial displacement increments
Sl=Si;                             %Creates a loop state vector
for i=1:steps+1
   Sl(3)=Sl(3)+dSd(3);
   Sl(5)=Sl(5)+dSd(5);
   Sl(9)=Sl(9)+dSd(9);
   Sl(11)=Sl(11)+dSd(11);
   Sl(15)=Sl(15)+dSd(15);
   Sl(21)=Sl(21)+dSd(21);
   Sl(27)=Sl(27)+dSd(27);
   Sl(28)=Sl(28)+dSd(28);
   Sl(31)=Sl(31)+dSd(31);
   Sl(32)=Sl(32)+dSd(32);
   Sl(33)=Sl(33)+dSd(33);
   Sl(34)=Sl(34)+dSd(34);
   Sl(35)=Sl(35)+dSd(35);
   Sl(36)=Sl(36)+dSd(36);
   [lVDLl]=muscprop(Sl,Po,V,IVD);
   lVDL(:,i)=lVDLl;
```

```
   [NUCNl]=muscprop(Sl,Po,V,NUC);
   NUCN(:,i)=NUCNl;
   [FlVDl,FNl,Qil,Fl,
KLl,KNl,eLl,ENl,ELl,areaLl,stretchl,Ehighl,Elowl,cfl,ecl,drl,dll,dLl,dNl,ll,sLl]=lVDmodel(So,Sl,Po,V,IVDa,N
UCa,dlVDa,dNUCa,lVDL(:,i),NUCN(:,i),dlVDL,dNUCN,lVDo,NUCo,Or,dOr,Gl, Gr, RBV,dRBV,area,
H,NF,NL,NlVD,lVD_prop,lVD);
   sL(:,i)=sLl;
   l(:,i)=ll;
   dN(:,i)=dNl;
   dL(:,i)=dLl;
   dl(:,i)=dll;
   dr(:,i)=drl;
   ec(:,i)=ecl;
   cf(:,i)=cfl;
   Ehigh(:,i)=Ehighl;
   Elow(:,i)=Elowl;
   areaL(:,i)=areaLl;
   %Lamella Stiffness
   KL(:,i)=KLl;
   eL(:,i)=eLl;
   stretch(:,i)=stretchl;
   %Lamella Modulus
   EL(:,i)=ELl;
   %Nucleus Modulus
   EN(:,i)=ENl;
   %Nucleus Stiffness
   KN(:,i)=KNl;
   %Lamella Forces
   FlVD(:,i)=FlVDl;
   %Lamella Stress
   Stress(:,i)=FlVDl./areaLl;
   %Nucleus Forces
   FN(:,i)=FNl;
   %lVD Displacement From Initial Posture
   S(1,i)=(-Si(31)+Sl(31))*1000;
   S(2,i)=(-Si(32)+Sl(32))*1000;
   S(3,i)=(-Si(33)+Sl(33))*1000;
   S(4,i)=Sl(34)*(180/pi);
   S(5,i)=Sl(35)*(180/pi);
   S(6,i)=Sl(36)*(180/pi);
   %lVD Forces
   Qi(1,i)=Qil(31);
   Qi(2,i)=Qil(32);
   Qi(3,i)=Qil(33);
   Qi(4,i)=Qil(34);
   Qi(5,i)=Qil(35);
   Qi(6,i)=Qil(36);
   %Experimental Forces [Morse-Stokes 2004]
   F(1,i)=Fl(1);
   F(2,i)=Fl(2);
   F(3,i)=Fl(3);
   F(4,i)=Fl(4);
   F(5,i)=Fl(5);
   F(6,i)=Fl(6);
   %Calculate Square Difference
   square_diff(1:6,i)=(Qi(1:6,i)-F(1:6,i)).^2;

   %Plot Spine Deformation
   % drawspine(Sl,Po,V,lVD,NUC,zeros(size(lVD,1),1),[0,1,.10],[0,0,.10]);
   % zoom(5)
   % pause(.001)

   %%%Displacement increments
   dSd(3)=D(3)/(steps);
   dSd(5)=D(5)/(steps);
   dSd(9)=D(9)/(steps);
   dSd(11)=D(11)/(steps);
   dSd(15)=D(15)/(steps);
   dSd(21)=D(21)/(steps);
   dSd(27)=D(27)/(steps);
```

```
   dSd(28)=D(28)/(steps);
   dSd(31)=D(31)/(steps);
   dSd(32)=D(32)/(steps);
   dSd(33)=D(33)/(steps);
   dSd(34)=D(34)/(steps);
   dSd(35)=D(35)/(steps);
   dSd(36)=D(36)/(steps);
end
RMS=zeros(6,1);
RMS(1)=sqrt(mean(square_diff(1,:)));       %[N]
RMS(2)=sqrt(mean(square_diff(2,:)));       %[N]
RMS(3)=sqrt(mean(square_diff(3,:)));       %[N]
RMS(4)=sqrt(mean(square_diff(4,:)));       %[N-m]
RMS(5)=sqrt(mean(square_diff(5,:)));       %[N-m]
RMS(6)=sqrt(mean(square_diff(6,:)));       %[N-m]
FvD=[S(1,:);        S(2,:);        S(3,:);        S(4,:);        S(5,:);        S(6,:);
   Qi(1,:);        Qi(2,:);        Qi(3,:);        Qi(4,:);        Qi(5,:);        Qi(6,:);
   F(1,:);        F(2,:);        F(3,:);        F(4,:);        F(5,:);        F(6,:)];
csvwrite('Forces vs Displacement.csv',FvD)
%%%Inferior ellipse of IVD, ei
[ei]=ellipse_abs(IVD_prop,NIVD,NL,Xi,1);
plot_ellipse(ei,So,Po,V,NL,NIVD)
%%%Superior ellipse of IVD, es
[es]=ellipse_abs(IVD_prop,NIVD,NL,Xs,2);
plot_ellipse(es,So,Po,V,NL,NIVD)
%%% Plot spine
drawspine(Sl,Po,V,IVD,NUC,zeros(size(IVD,1),1),[0,1,.10],[0,0,.10]);
zoom(5)
xlabel('Right Lateral/Left Lateral [m]')
ylabel('Anterior/Posterior [m]')
zlabel('Superior/Inferior [m]')
%%Plot IVD forces
plot_forces(So,Sd,Sl,Si,dSd,Qi,F)
%%%%%%%End of Program%%%%%%%%%%%%%%%%%%%%%%%%%%%%%%%%%
```

Appendix B: Figures

B.1. SNS Model Figures

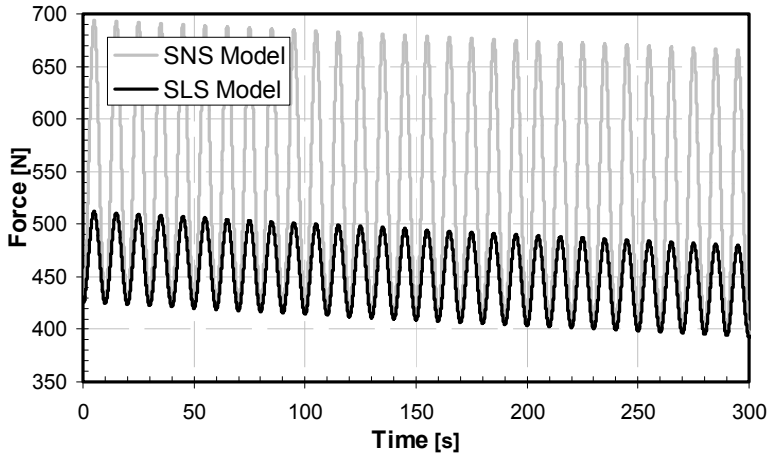

Figure B.1.1 Cyclic relaxation of the IVD models subjected to a frequency of 0.1 Hz.

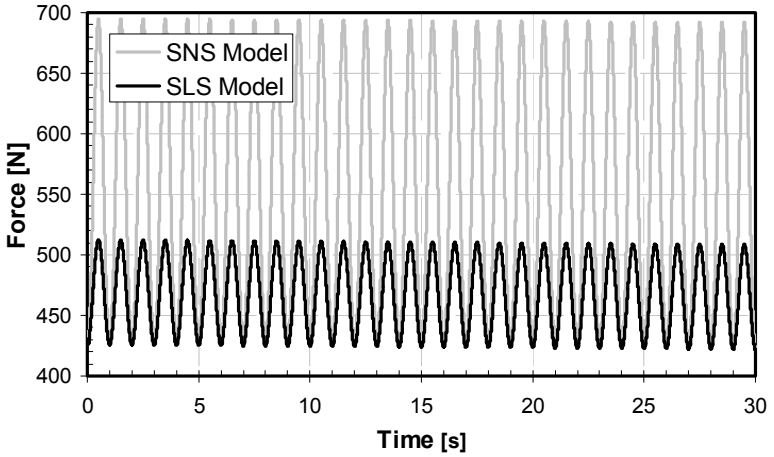

Figure B.1.2 Cyclic relaxation of the IVD models subjected to a frequency of 1 Hz.

B.2. Three-dimensional Model Figures

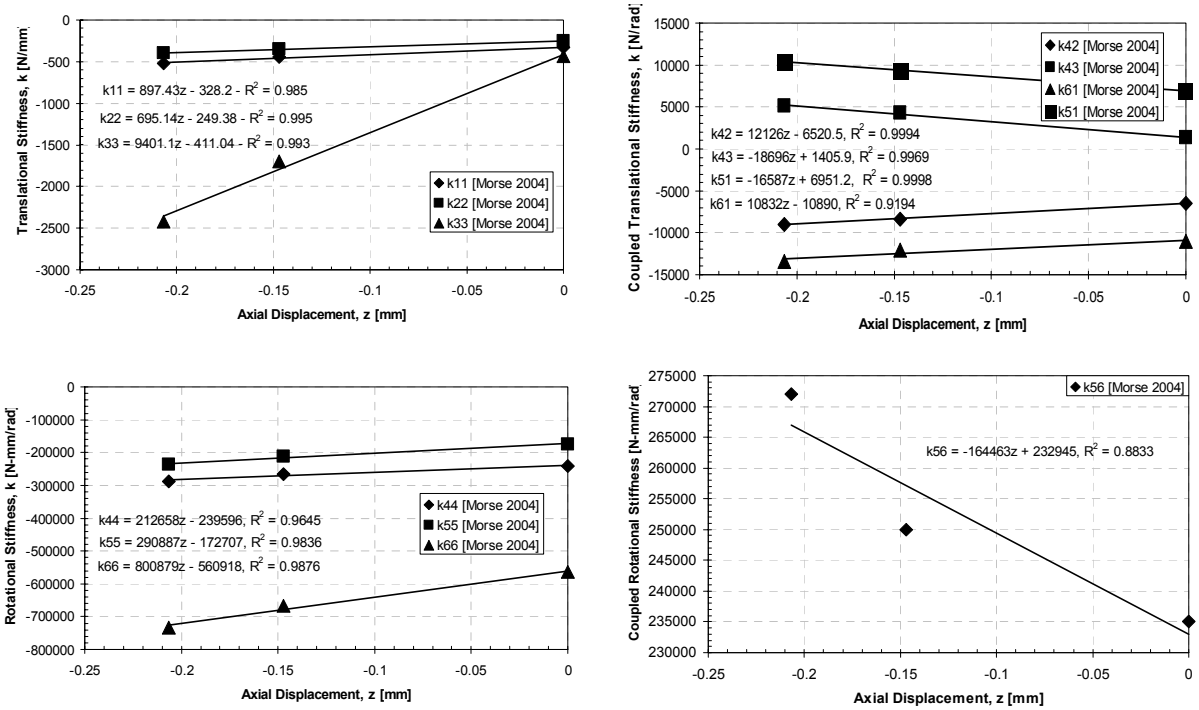

Figure B.2.1. Preload displacement dependent stiffness (L2-L3) (Gardner-Morse and Stokes 2004).

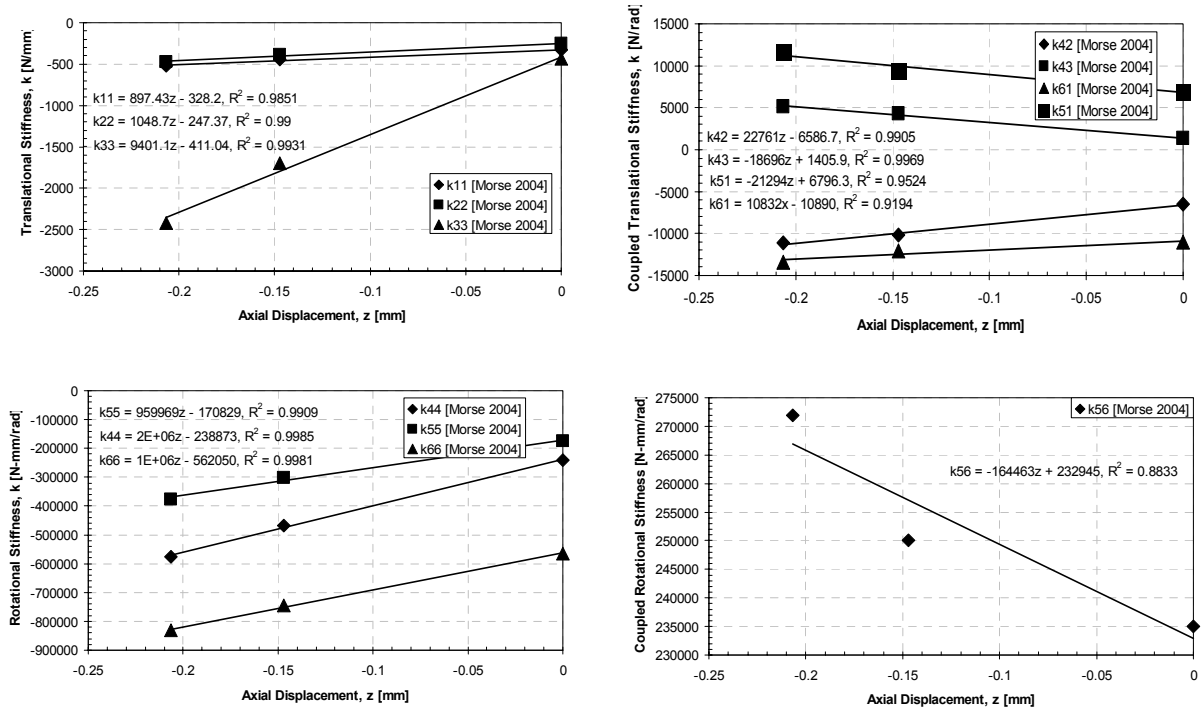

Figure B.2.2. Preload displacement dependent stiffness (L4-L5) (Gardner-Morse and Stokes 2004).

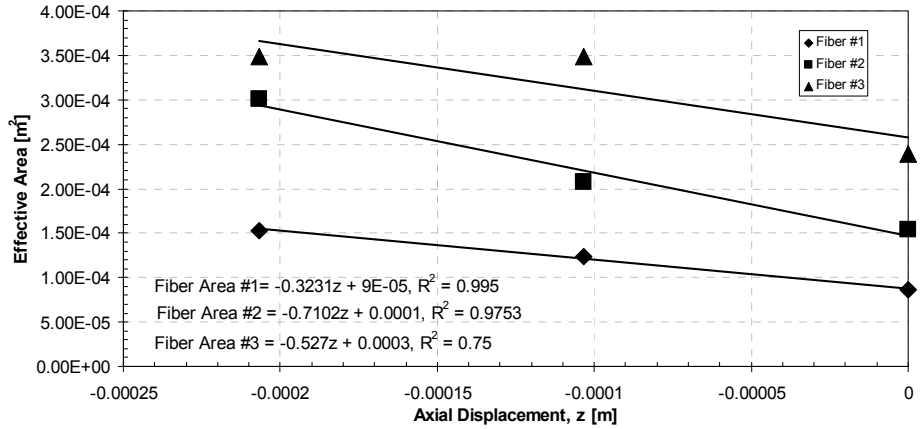

Figure B.2.3. Modeling the effective area of the IVJ as function of preload displacement (Posture 2, L2-L3). Note: For clarity, symmetric fibers are not shown.

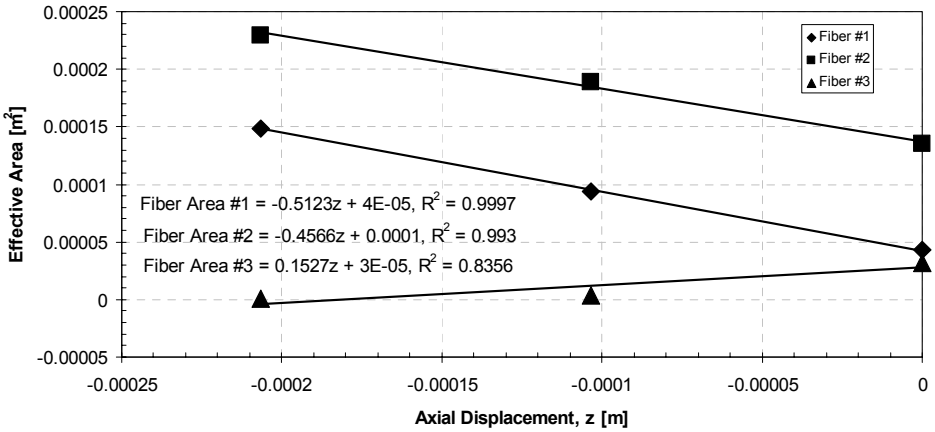

Figure B.2.4. Modeling the effective area of the IVJ as function of preload displacement (Posture 1, L4-L5). Note: For clarity, symmetric fibers are not shown.

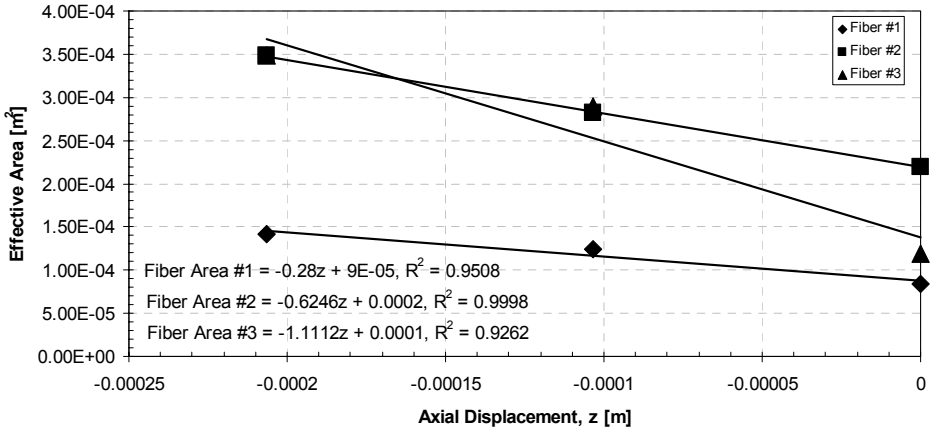

Figure B.2.5. Modeling the effective area of the IVJ as function of preload displacement (Posture 2, L4-L5). Note: For clarity, symmetric fibers are not shown.

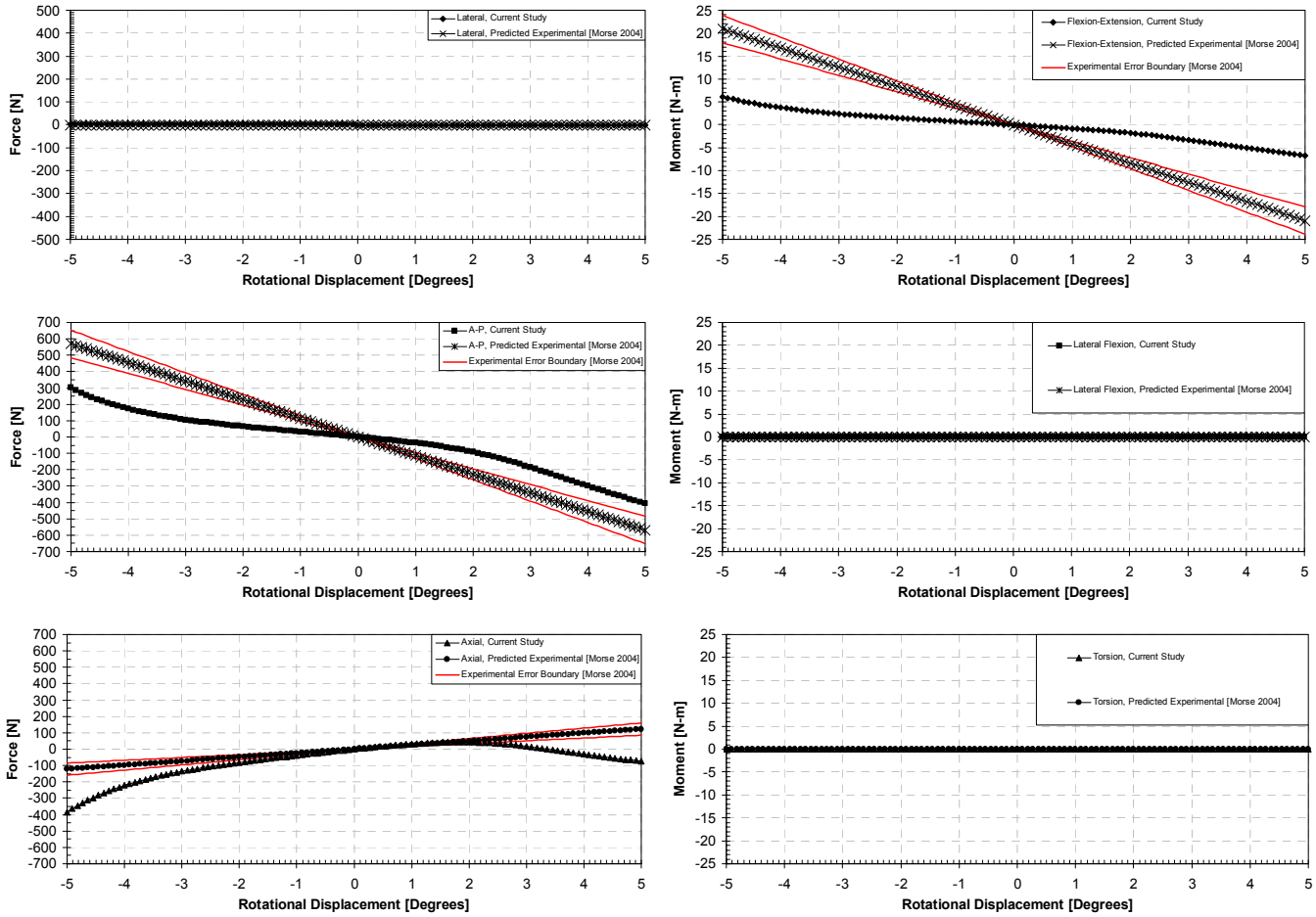

Figure B.2.6. Three-dimensional model's response to flexion/extension under a preload displacement of 0 mm (Posture 1, L2-L3).

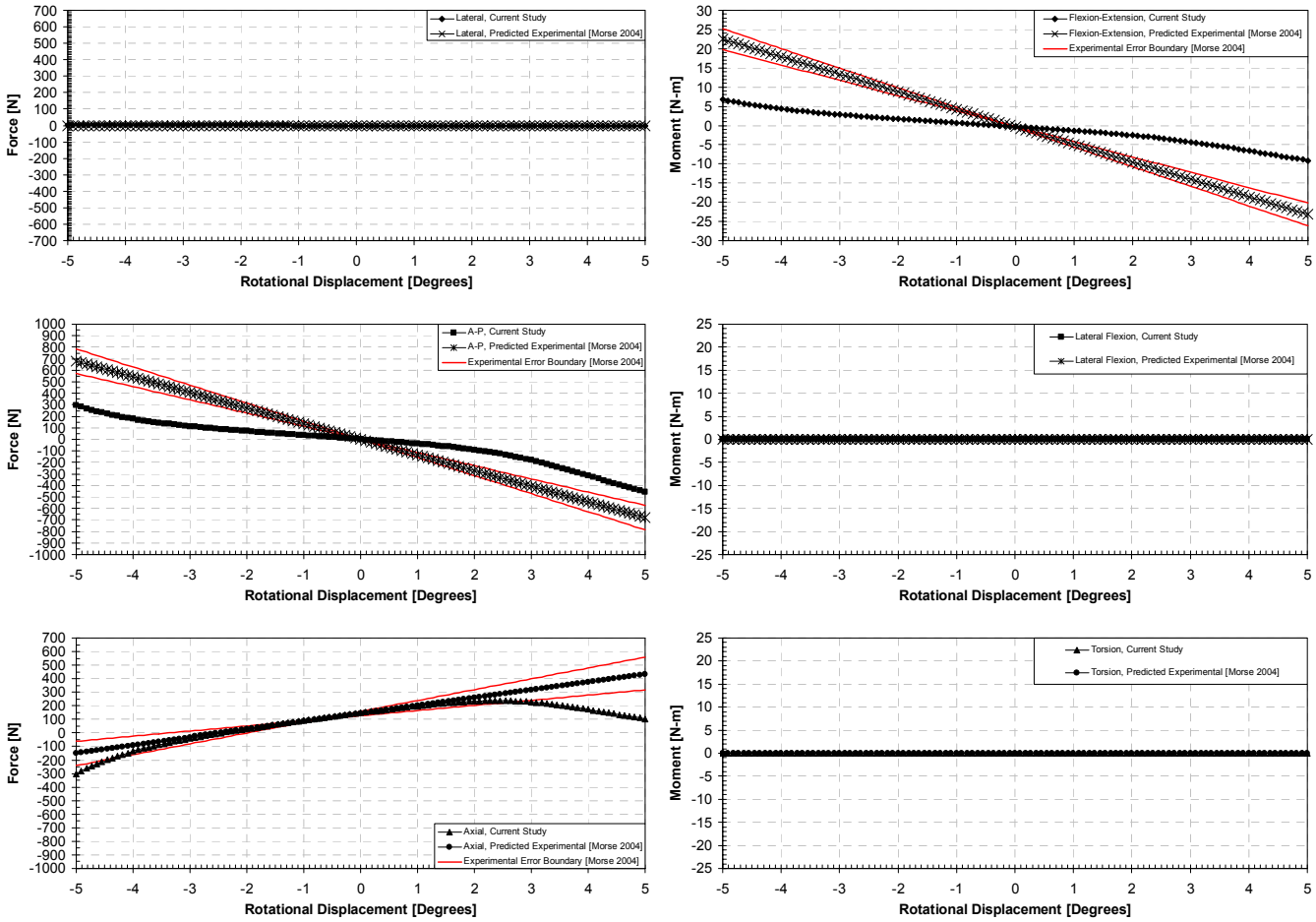

Figure B.2.7. Three-dimensional model's response to flexion/extension under a preload displacement of 0.1033 mm (Posture 1, L2-L3).

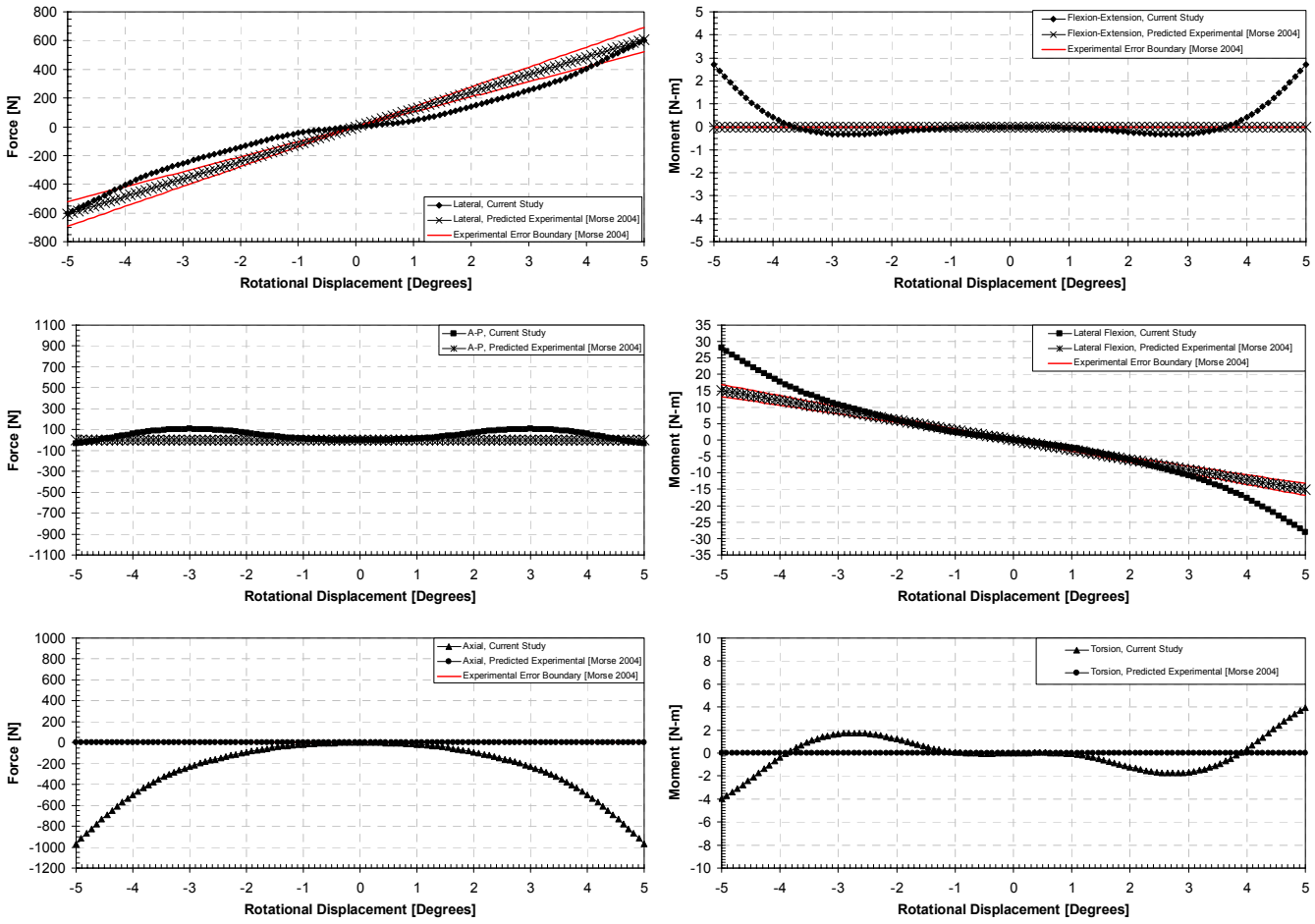

Figure B.2.8. Three-dimensional model's response to lateral flexion under a preload displacement of 0 mm (Posture 1, L2-L3).

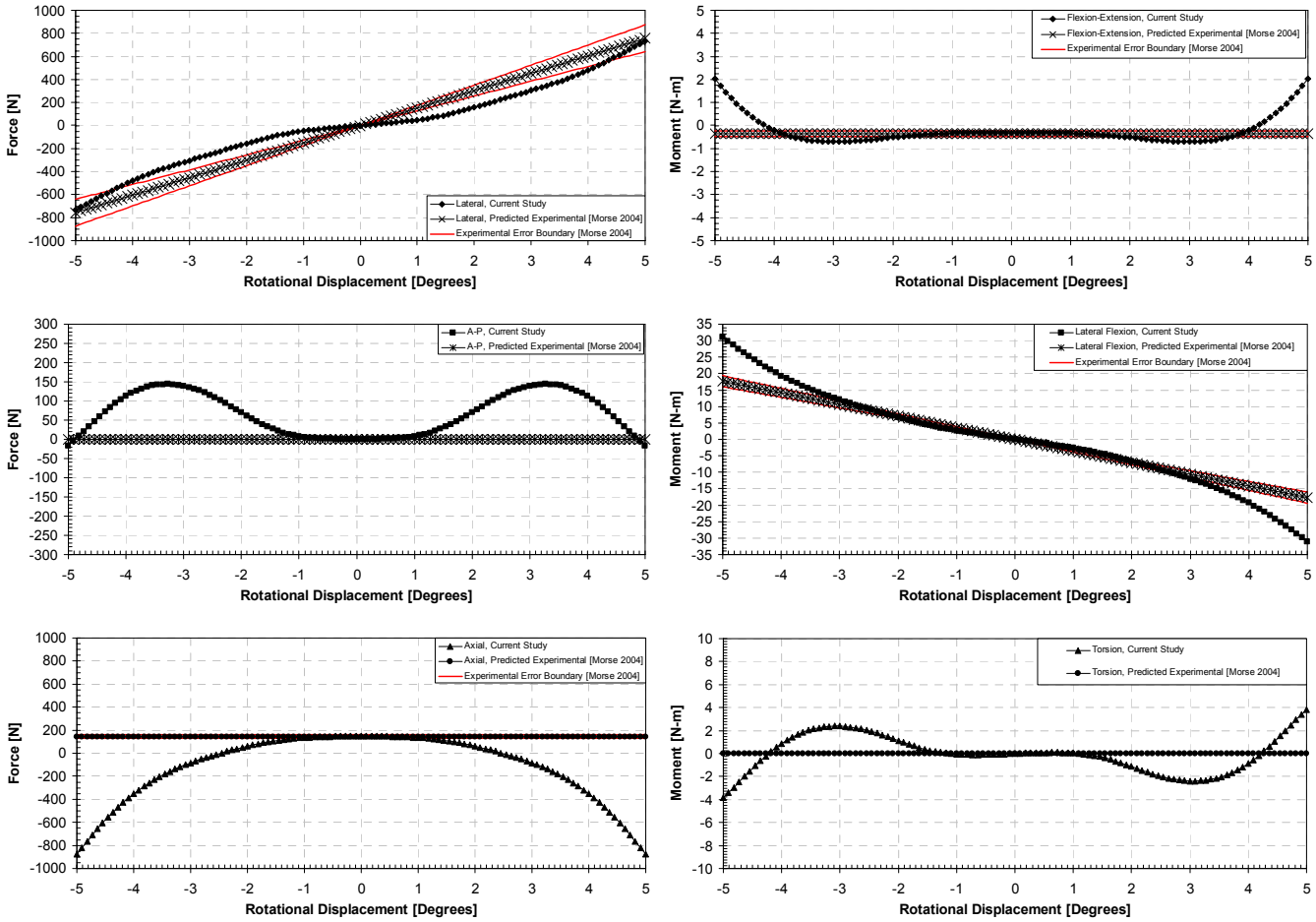

Figure B.2.9. Three-dimensional model's response to lateral flexion under a preload displacement of 0.1033 mm (Posture 1, L2-L3).

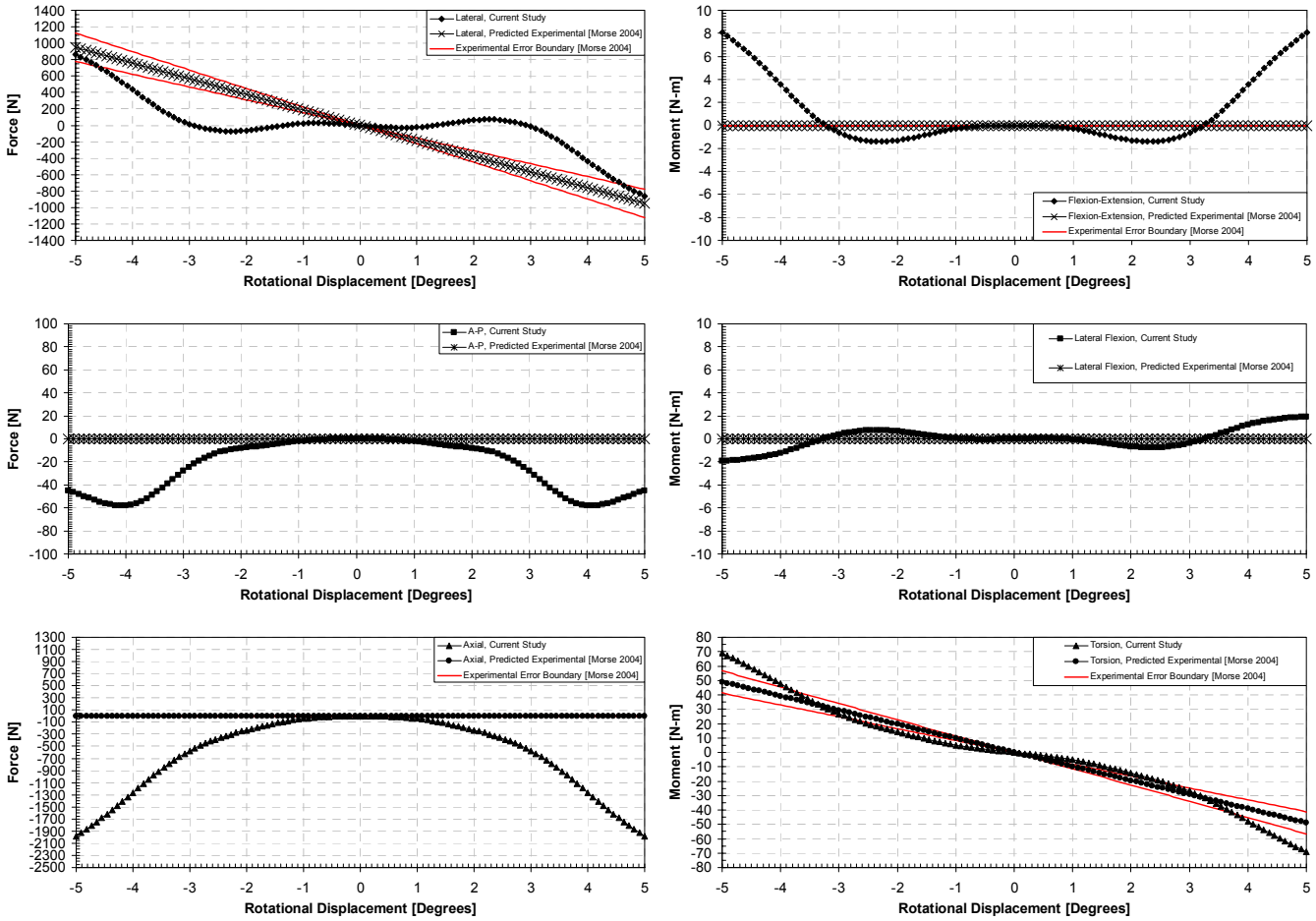

Figure B.2.10. Three-dimensional model's response to torsion under a preload displacement of 0 mm (Posture 1, L2-L3).

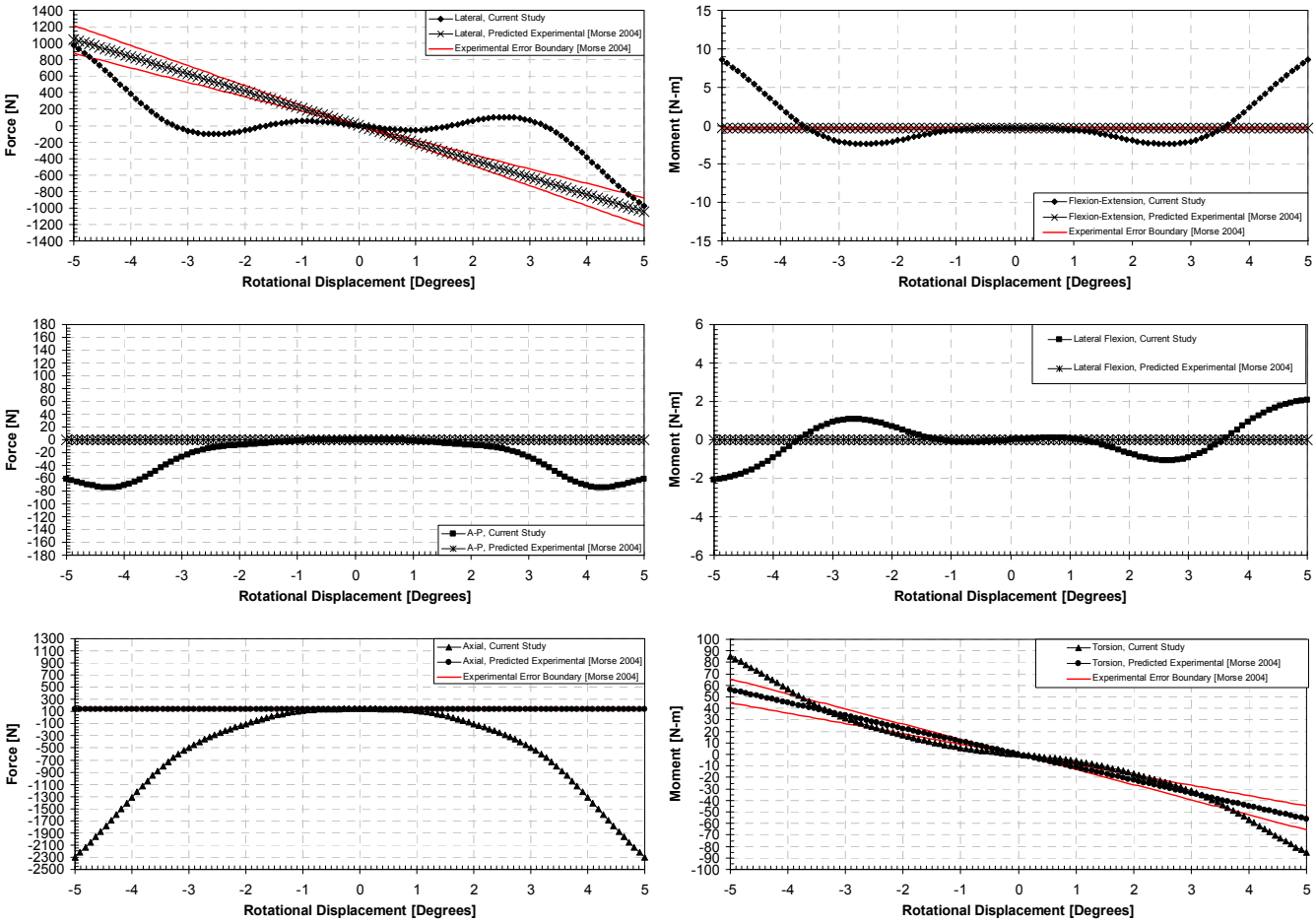

Figure B.2.11. Three-dimensional model's response to torsion under a preload displacement of 0.1033 mm (Posture 1, L2-L3).

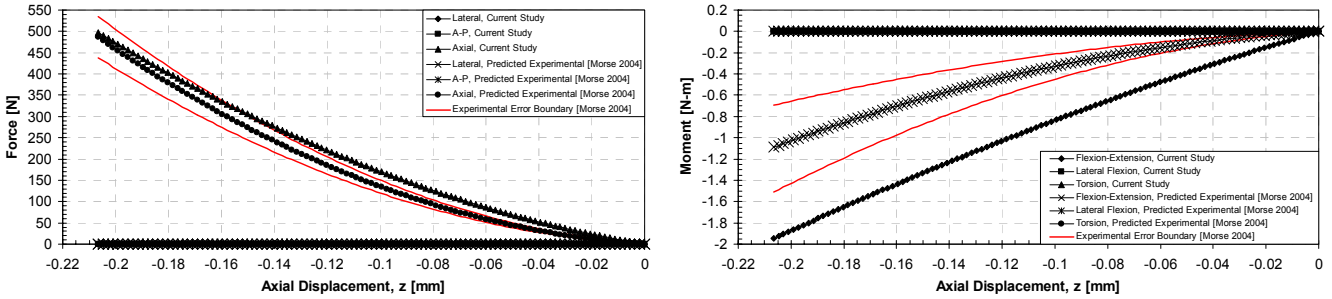

Figure B.2.12. Three-dimensional model's response to axial compression (Posture 2, L2-L3).

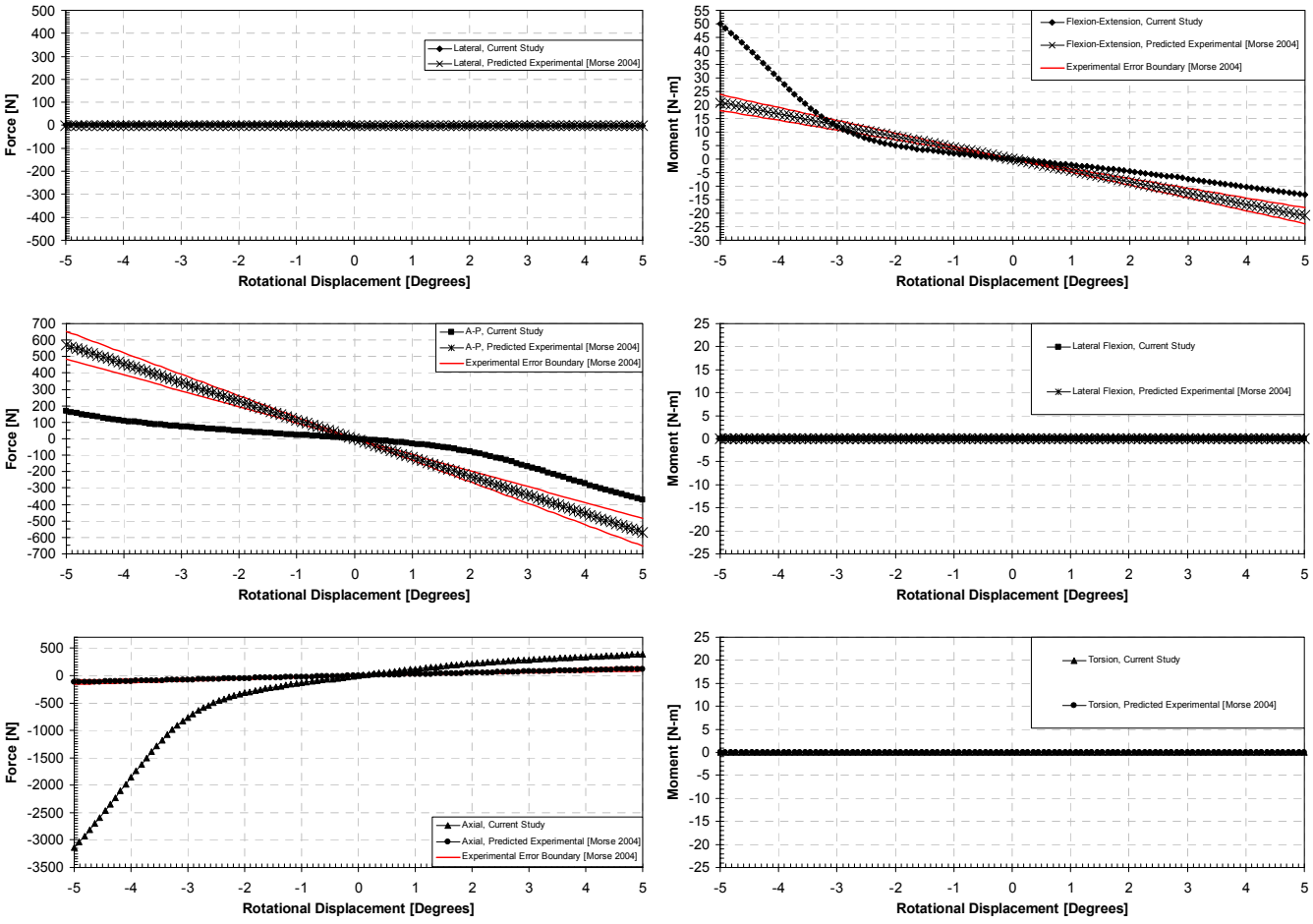

Figure B.2.13. Three-dimensional model's response to flexion/extension under a preload displacement of 0 mm (Posture 2, L2-L3).

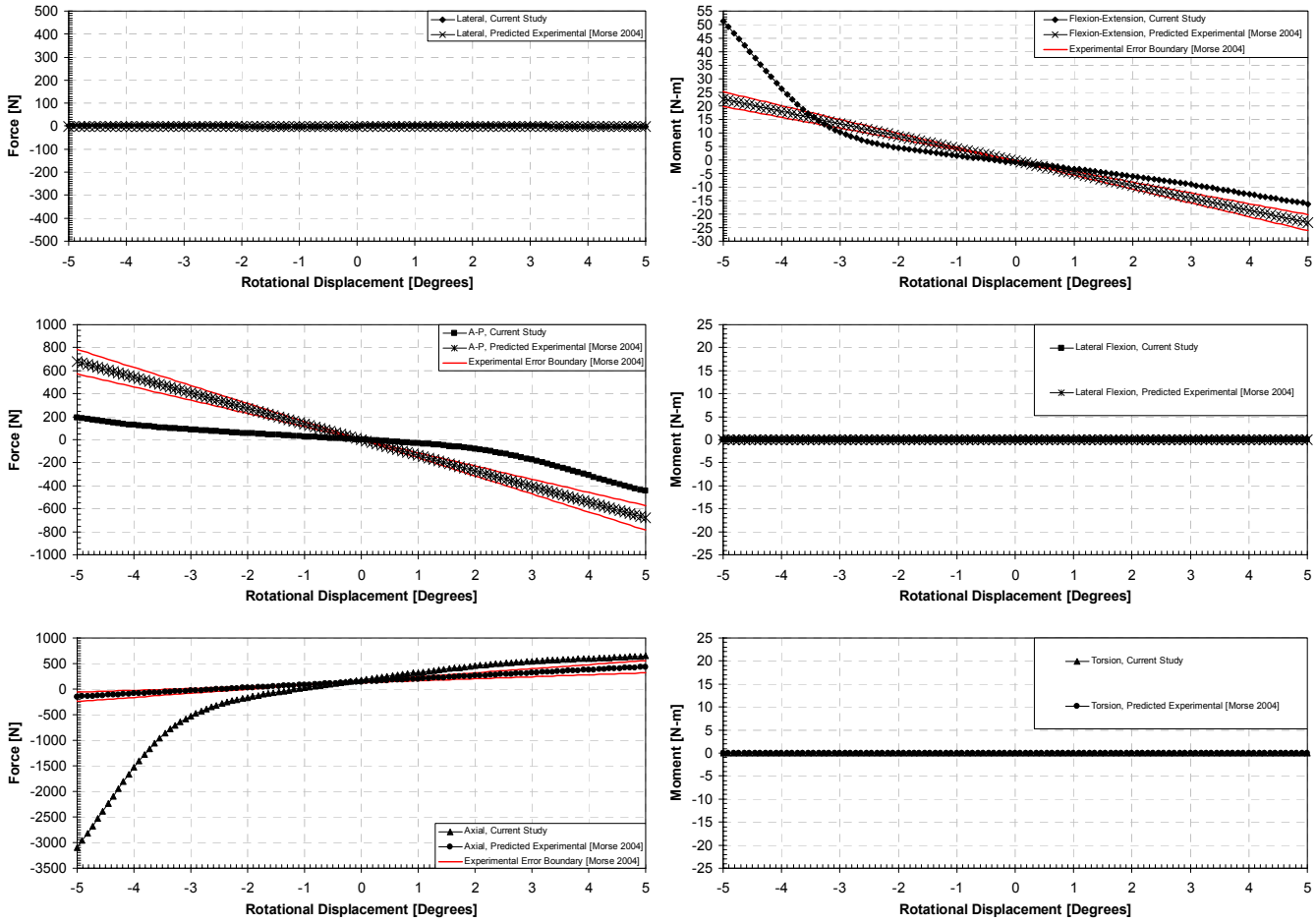

Figure B.2.14. Three-dimensional model's response to flexion/extension under a preload displacement of 0.1033 mm (Posture 2, L2-L3).

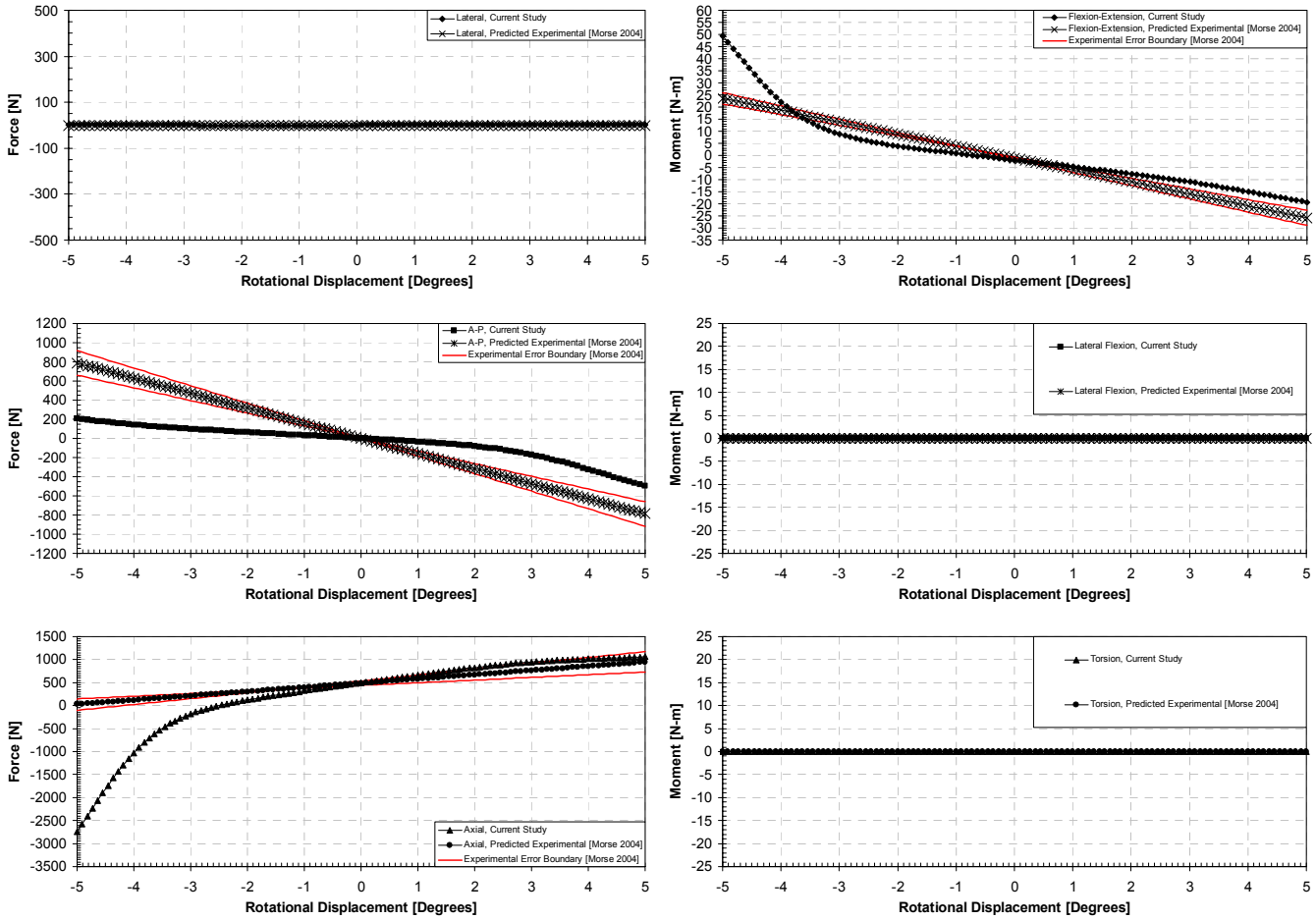

Figure B.2.15. Three-dimensional model's response to flexion/extension under a preload displacement of 0.2066 mm (Posture 2, L2-L3).

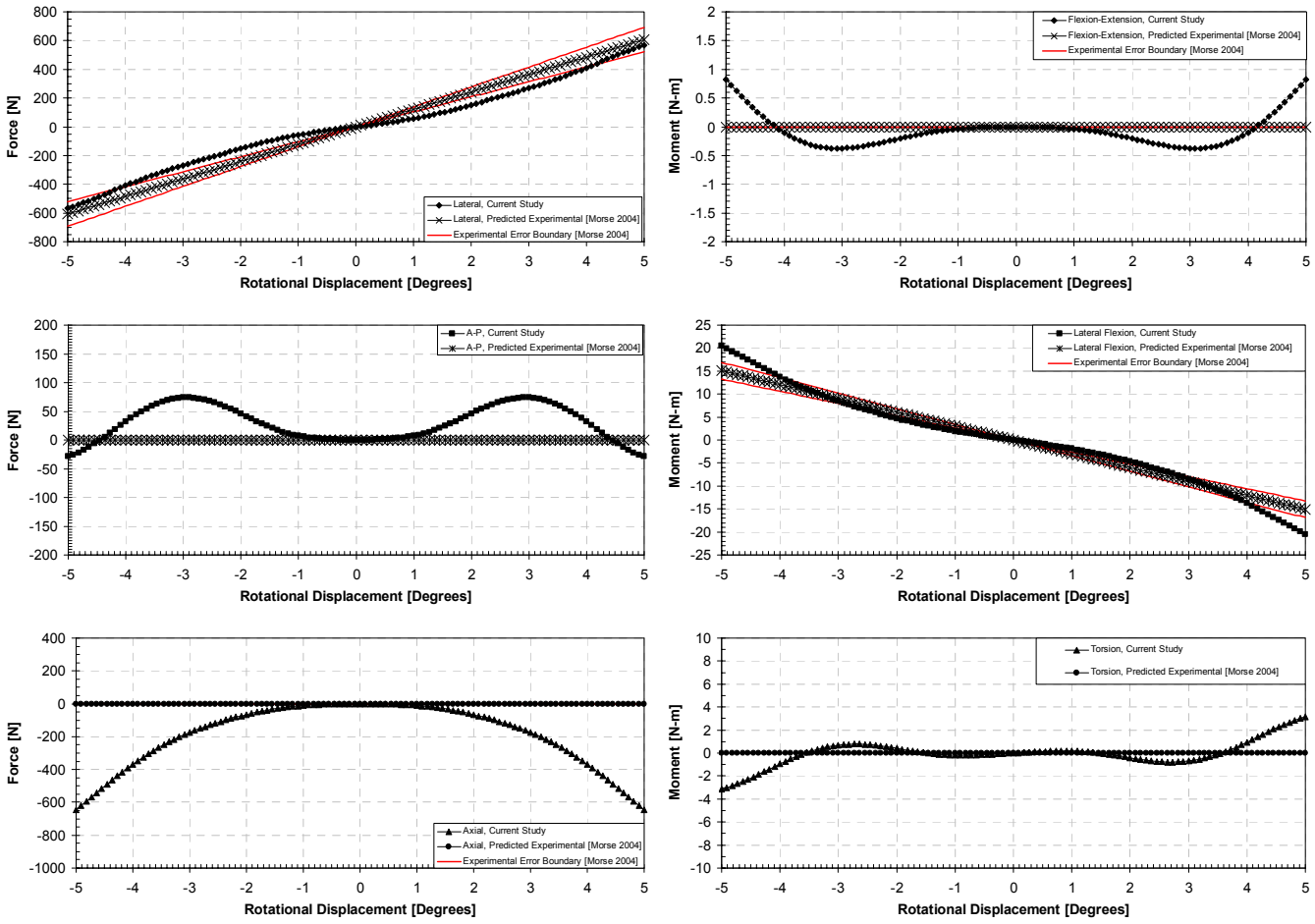

Figure B.2.16. Three-dimensional model's response to lateral flexion under a preload displacement of 0 mm (Posture 2, L2-L3).

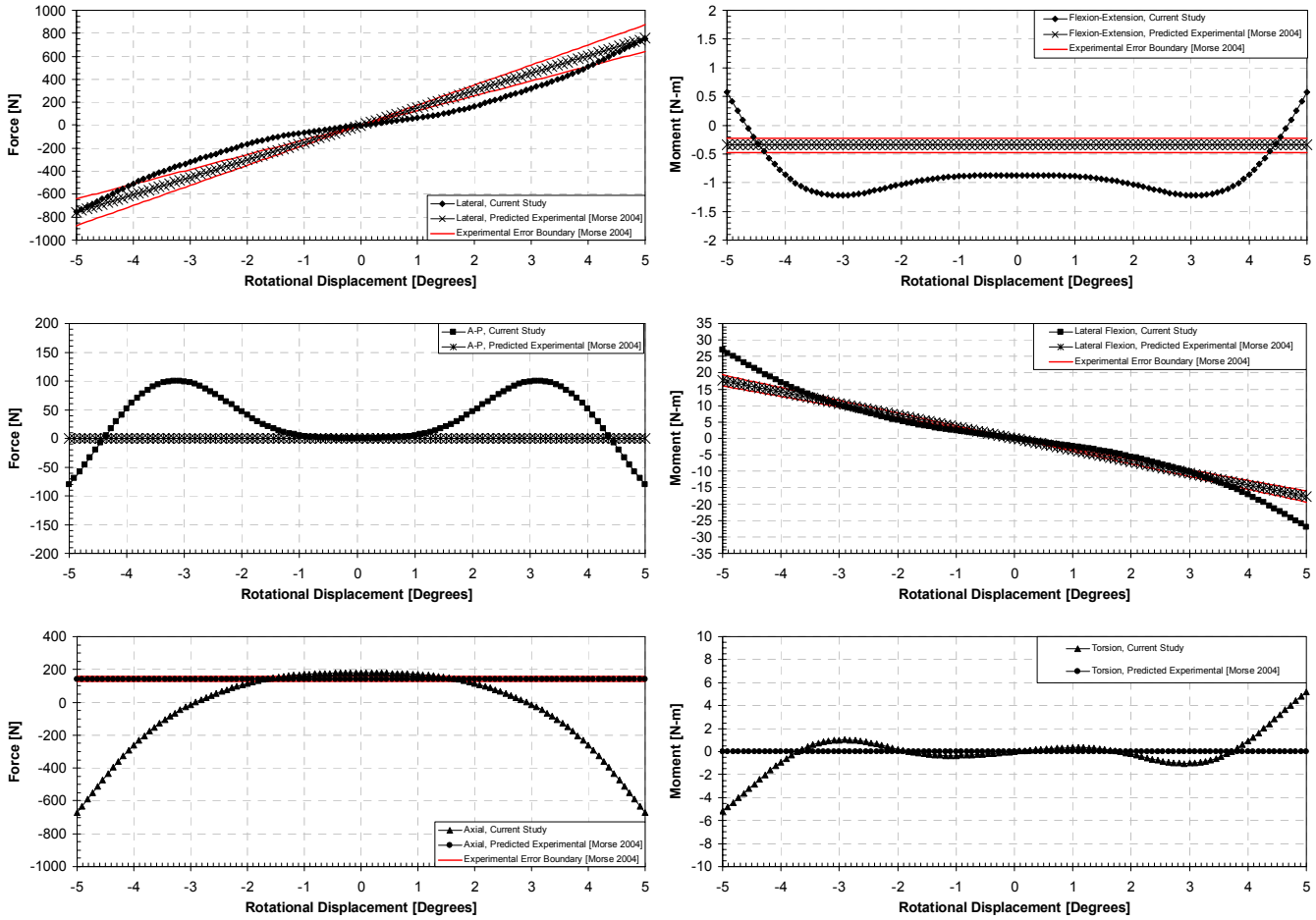

Figure B.2.17. Three-dimensional model's response to lateral flexion under a preload displacement of 0.1033 mm (Posture 2, L2-L3).

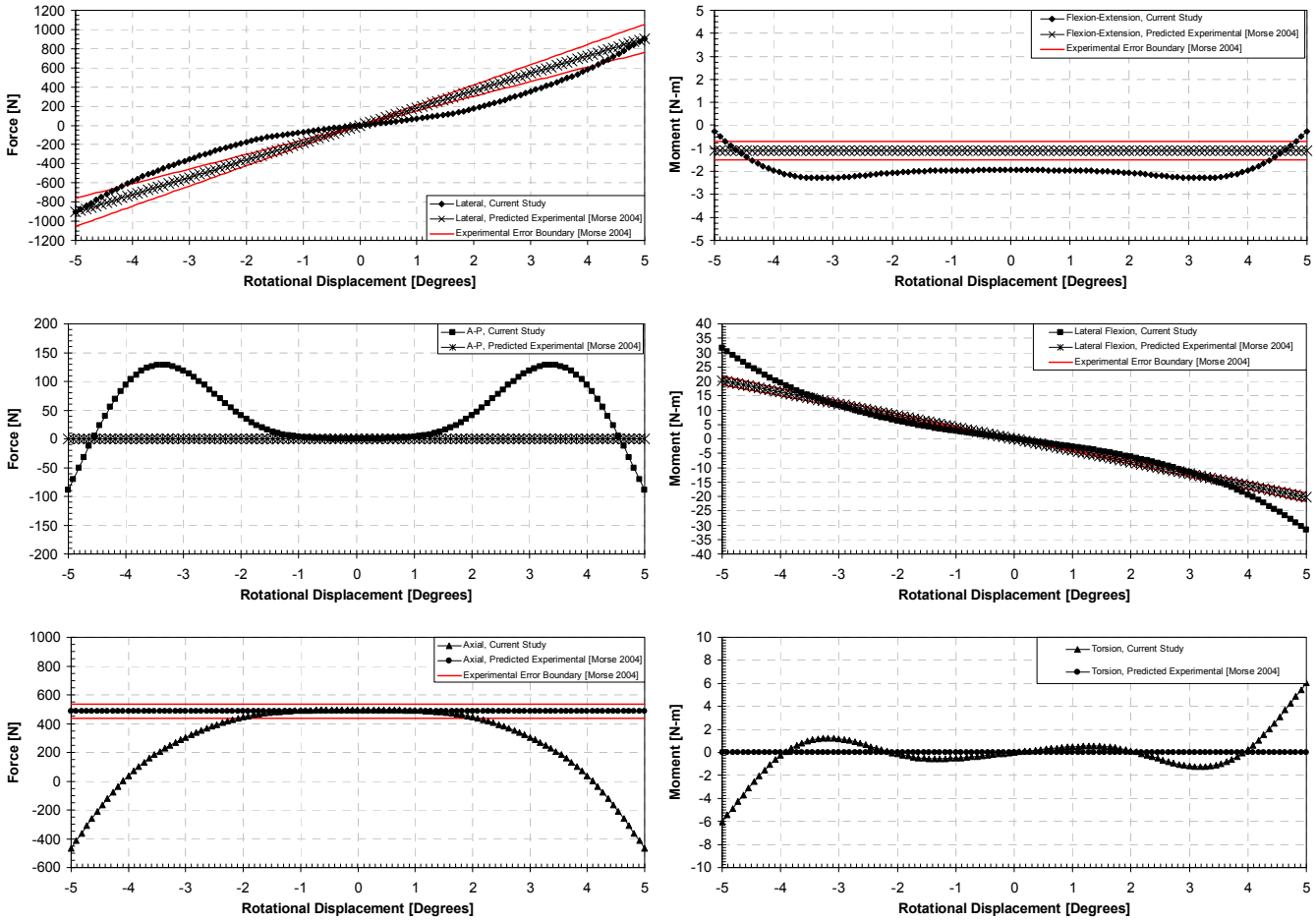

Figure B.2.18. Three-dimensional model's response to lateral flexion under a preload displacement of 0.2066 mm (Posture 2, L2-L3).

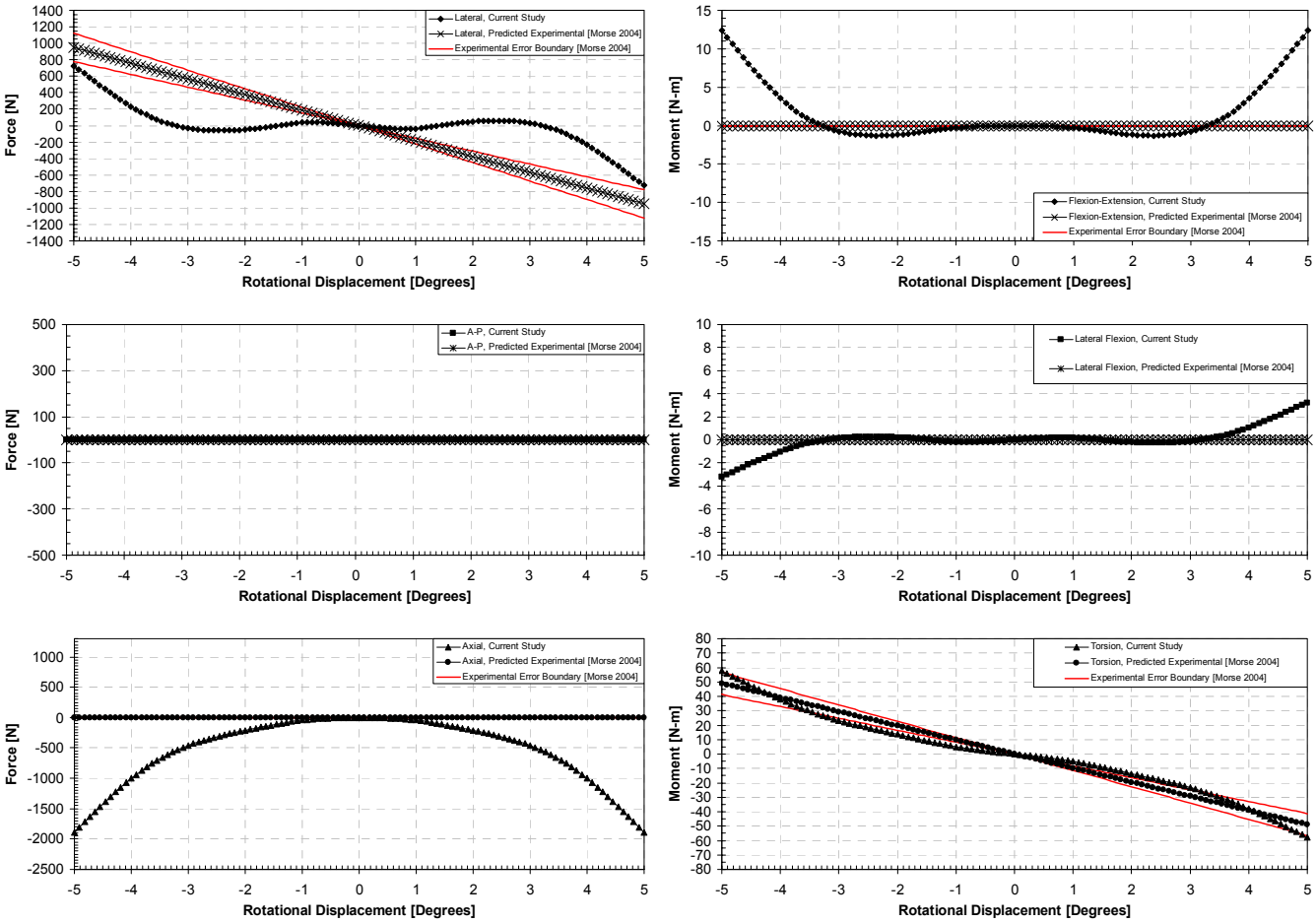

Figure B.2.19. Three-dimensional model's response to torsion under a preload displacement of 0 mm (Posture 2, L2-L3).

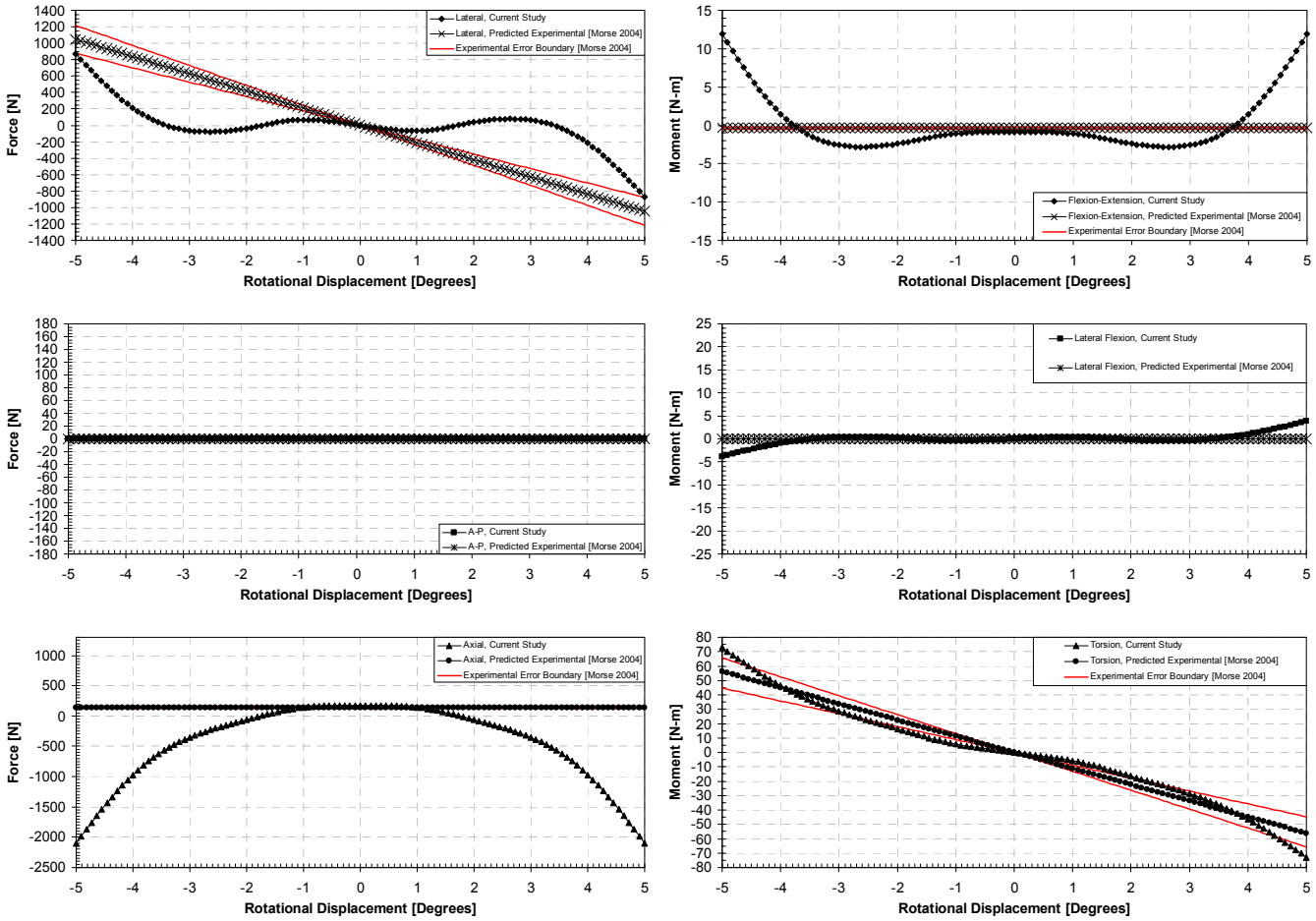

Figure B.2.20. Three-dimensional model's response to torsion under a preload displacement of 0.1033 mm (Posture 2, L2-L3).

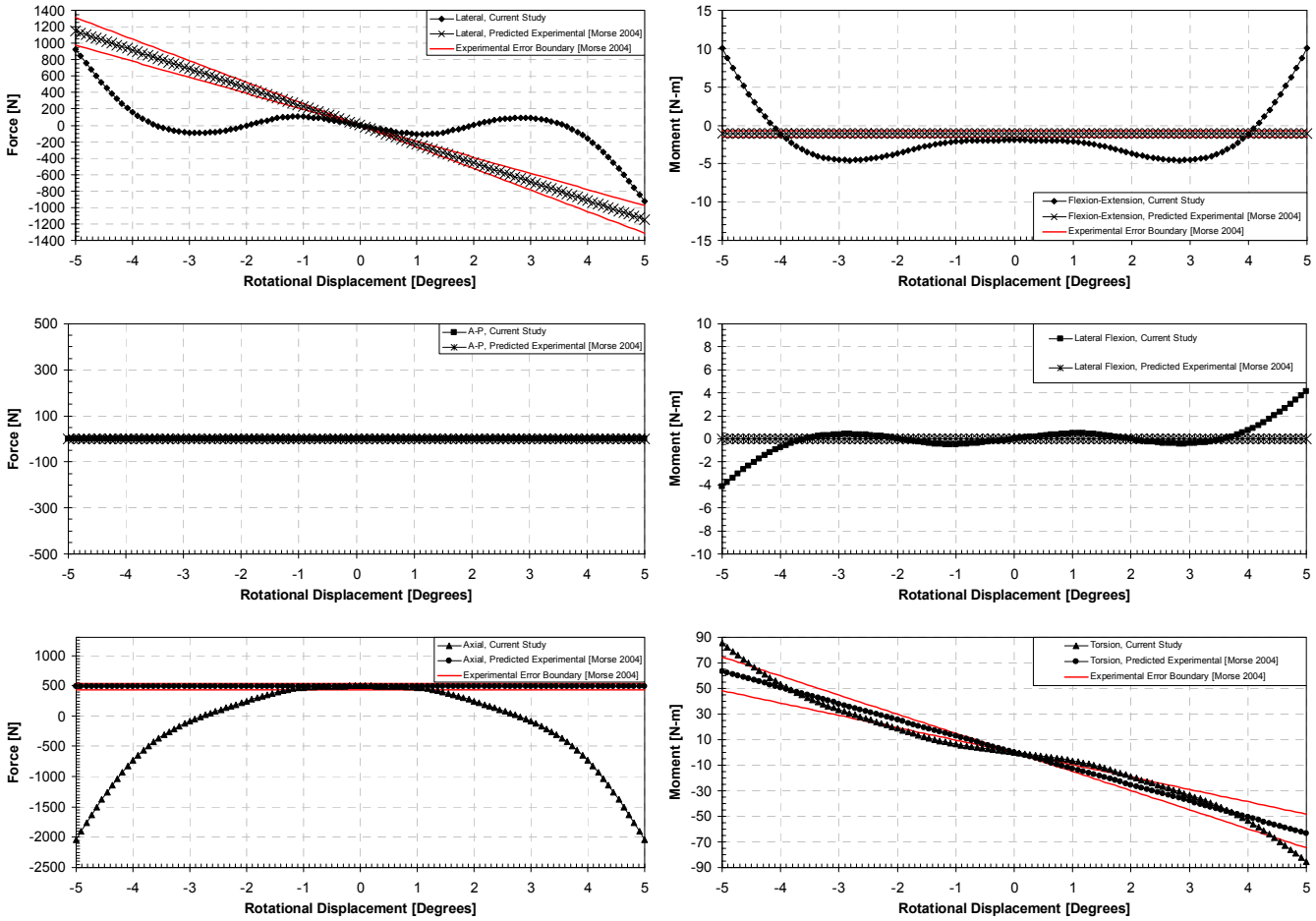

Figure B.2.21. Three-dimensional model's response to torsion under a preload displacement of 0.2066 mm (Posture 2, L2-L3).

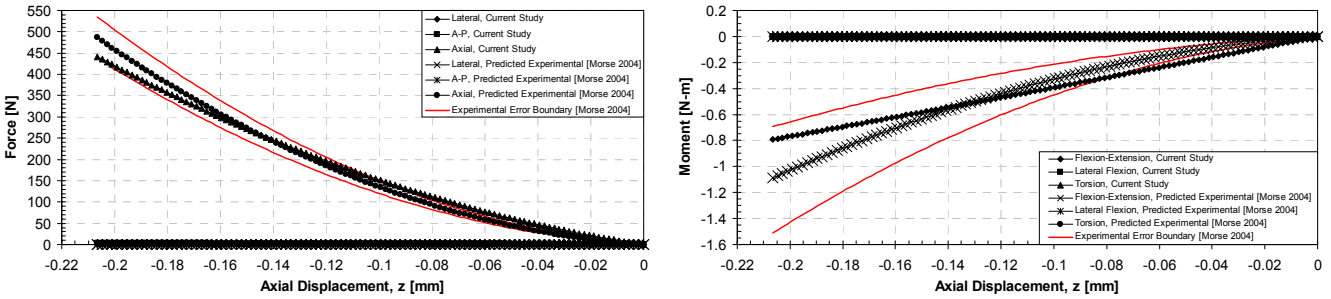

Figure B.2.22. Three-dimensional model's response to axial compression (Posture 1, L4-L5).

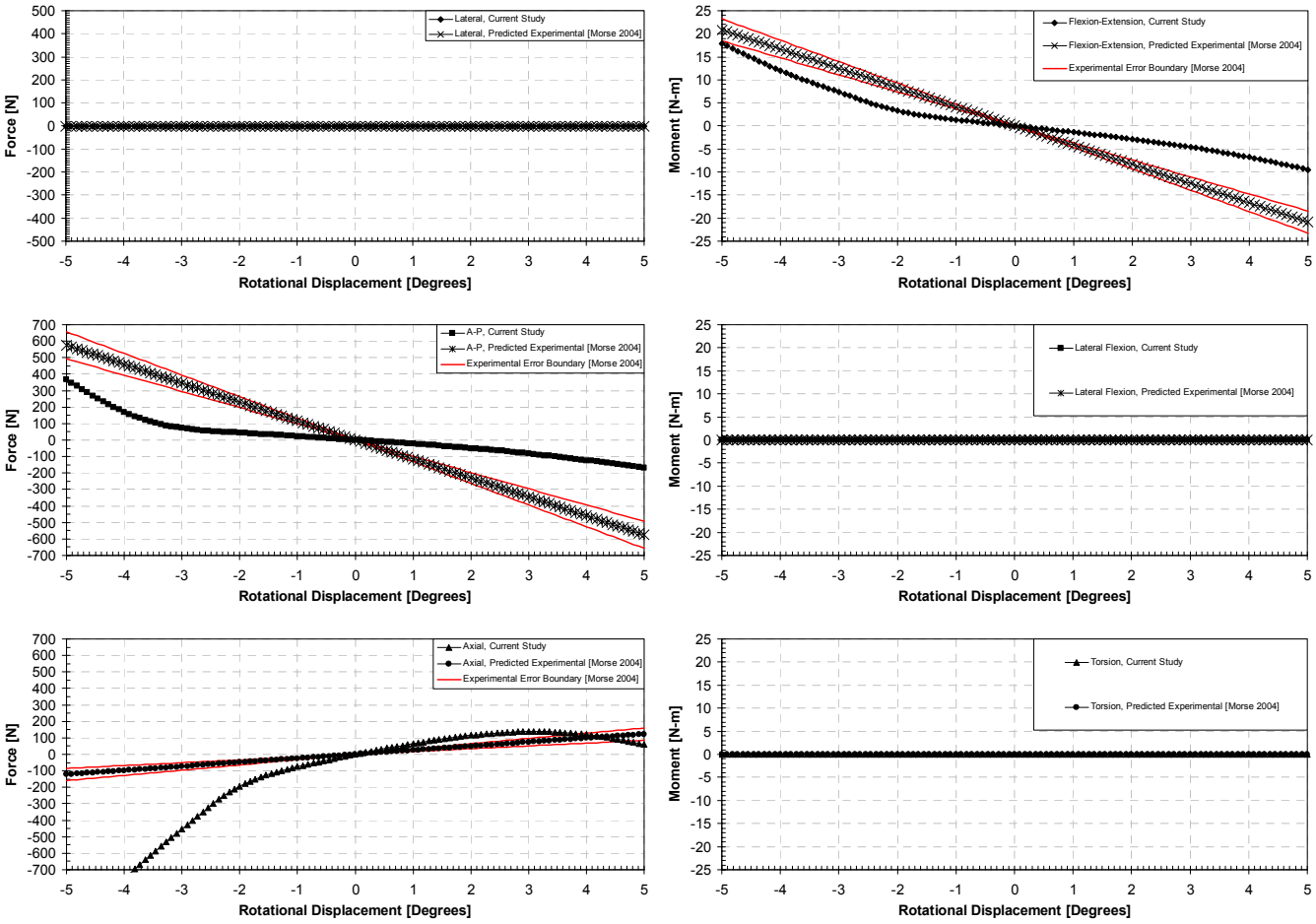

Figure B.2.23. Three-dimensional model's response to flexion/extension under a preload displacement of 0 mm (Posture 1, L4-L5).

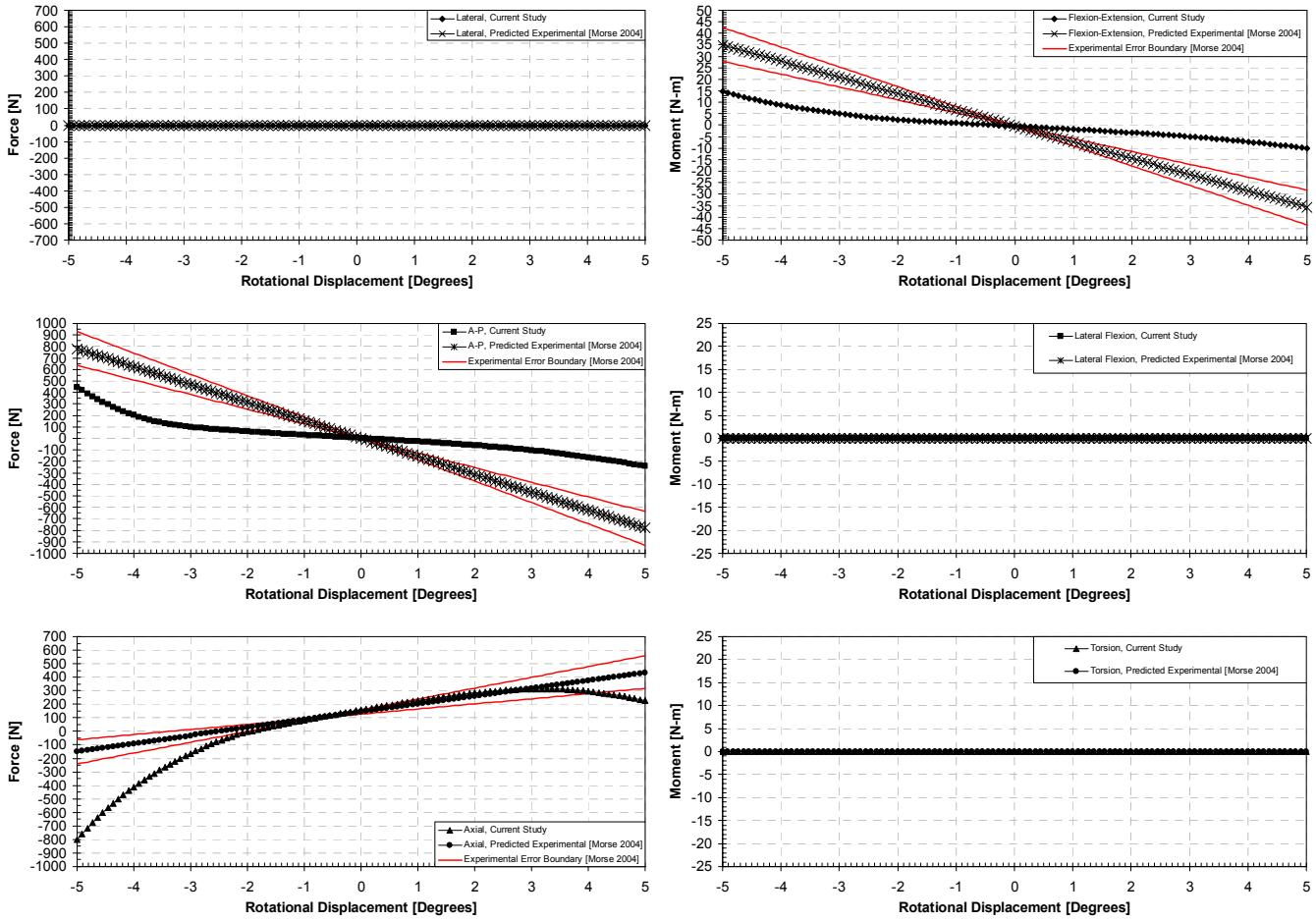

Figure B.2.24. Three-dimensional model's response to flexion/extension under a preload displacement of 0.1033 mm (Posture 1, L4-L5).

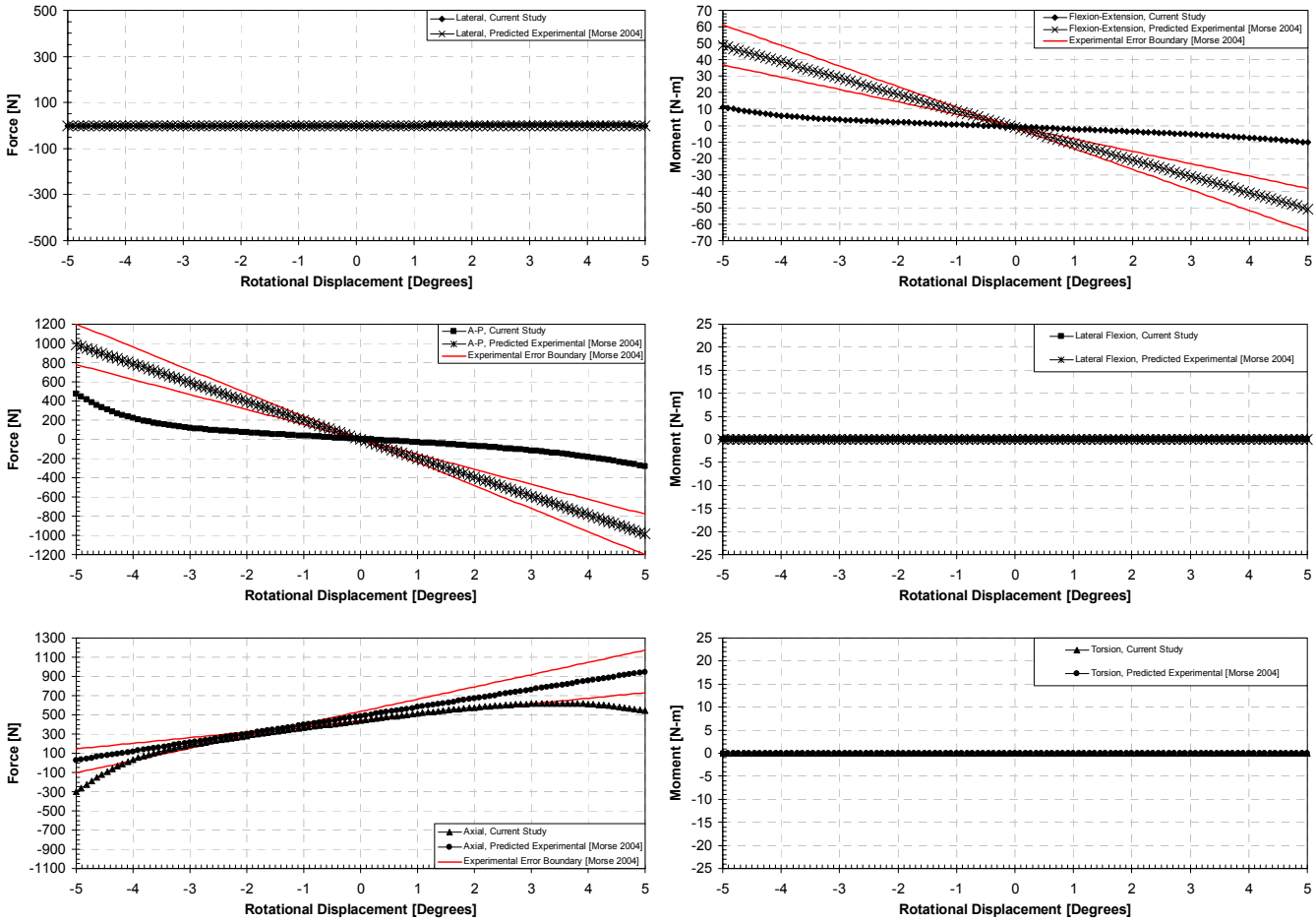

Figure B.2.25. Three-dimensional model's response to flexion/extension under a preload displacement of 0.2066 mm (Posture 1, L4-L5).

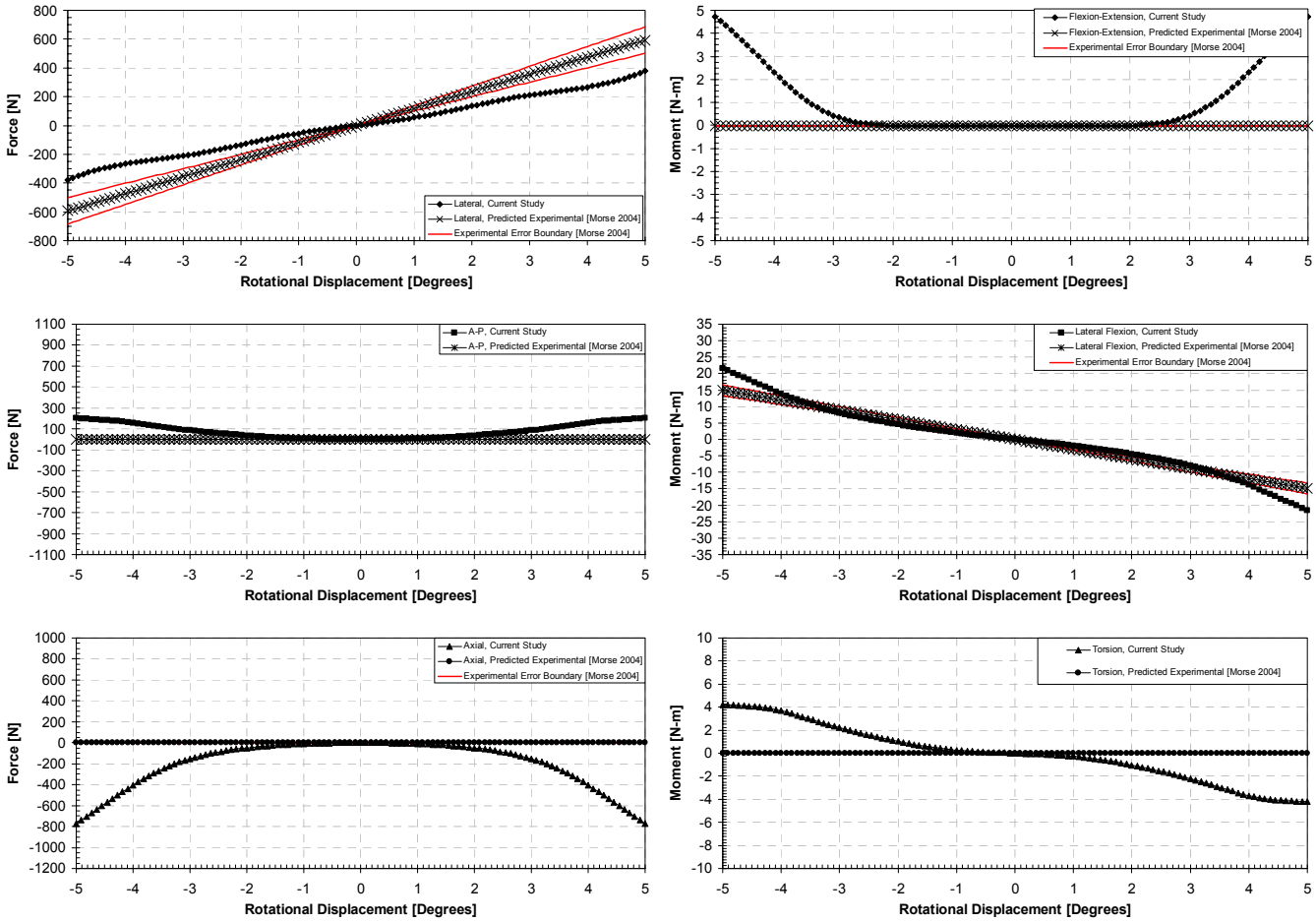

Figure B.2.26. Three-dimensional model's response to lateral flexion under a preload displacement of 0 mm (Posture 1, L4-L5).

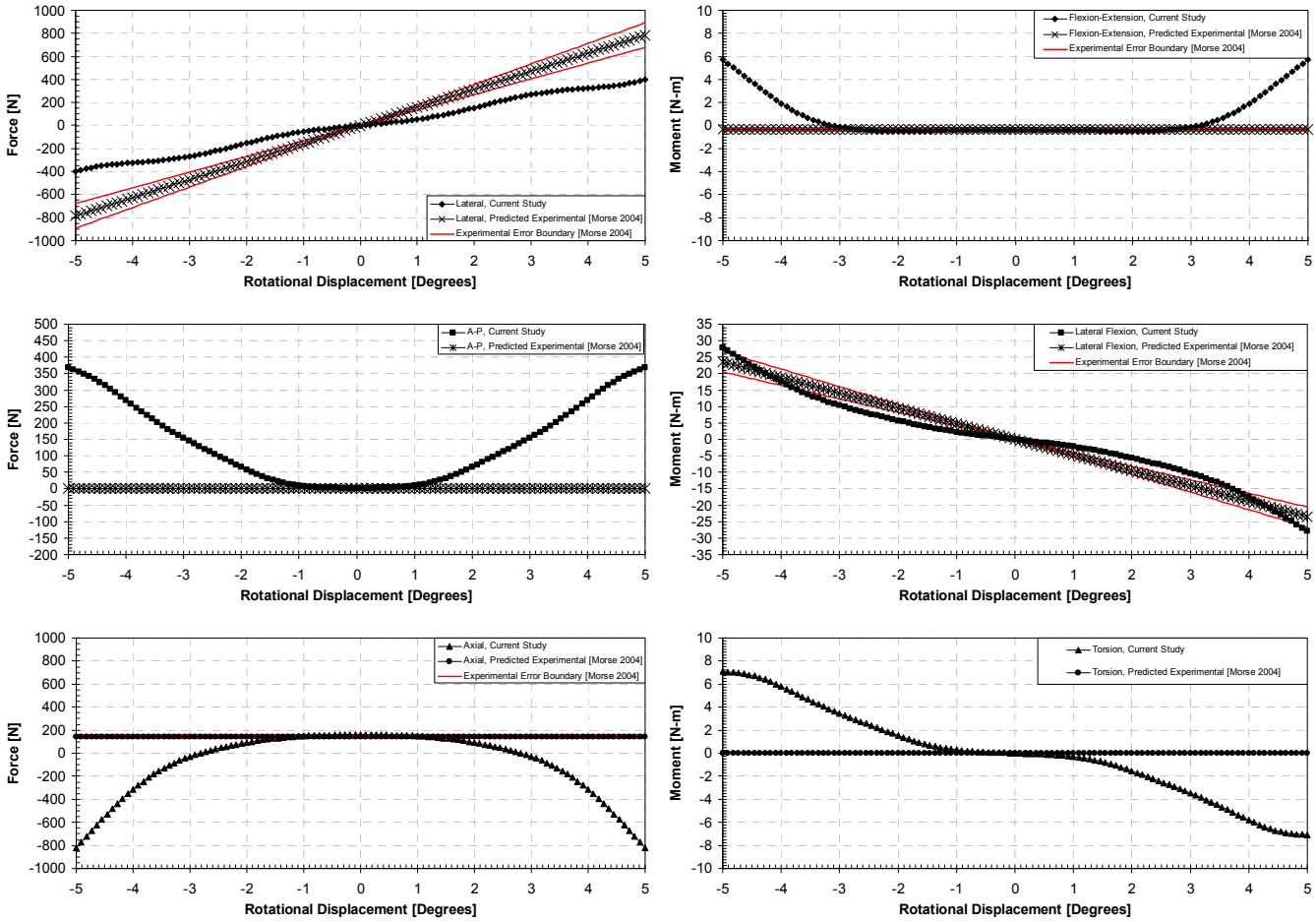

Figure B.2.27. Three-dimensional model's response to lateral flexion under a preload displacement of 0.1033 mm (Posture 1, L4-L5).

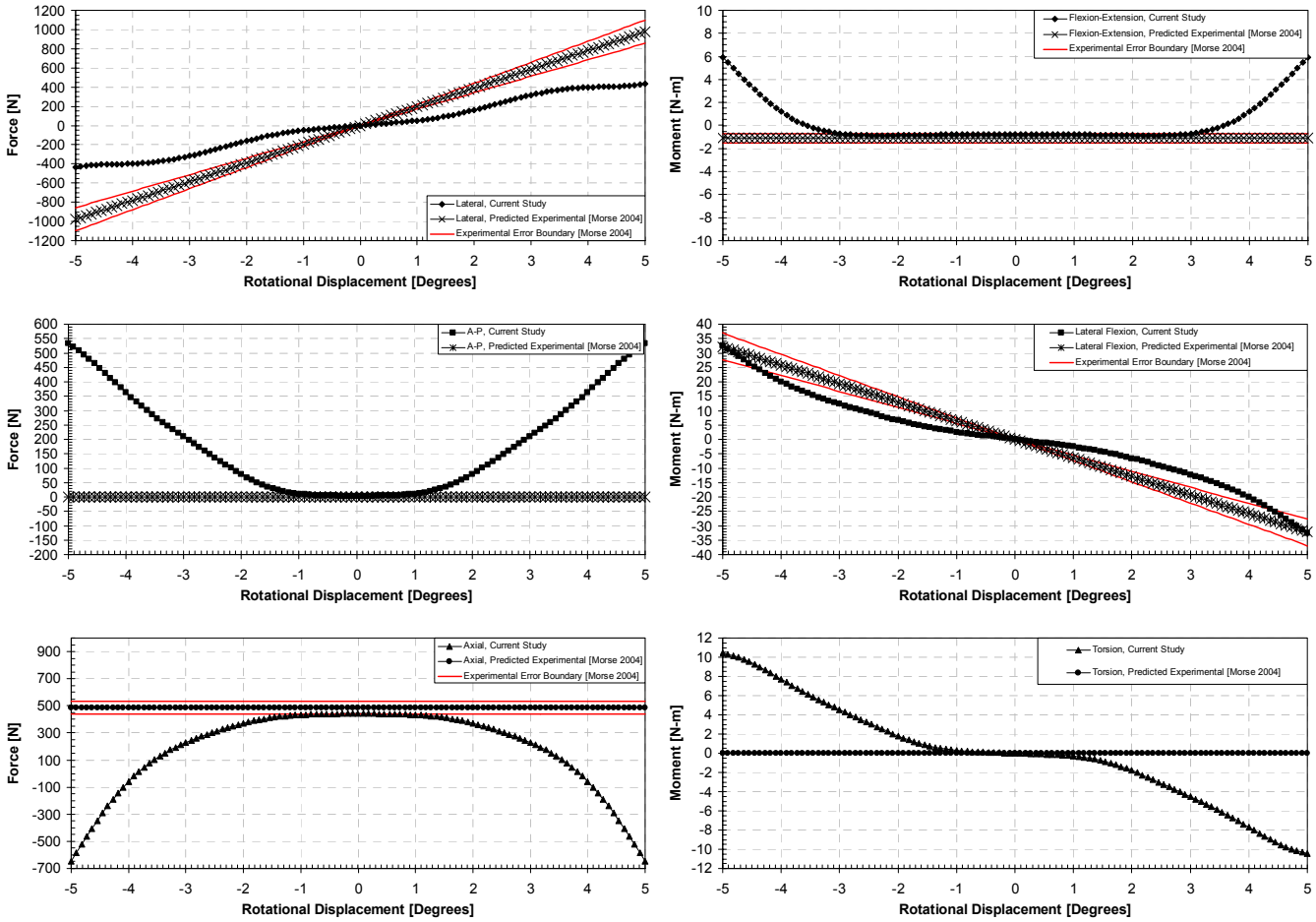

Figure B.2.28. Three-dimensional model's response to lateral flexion under a preload displacement of 0.2066 mm (Posture 1, L4-L5).

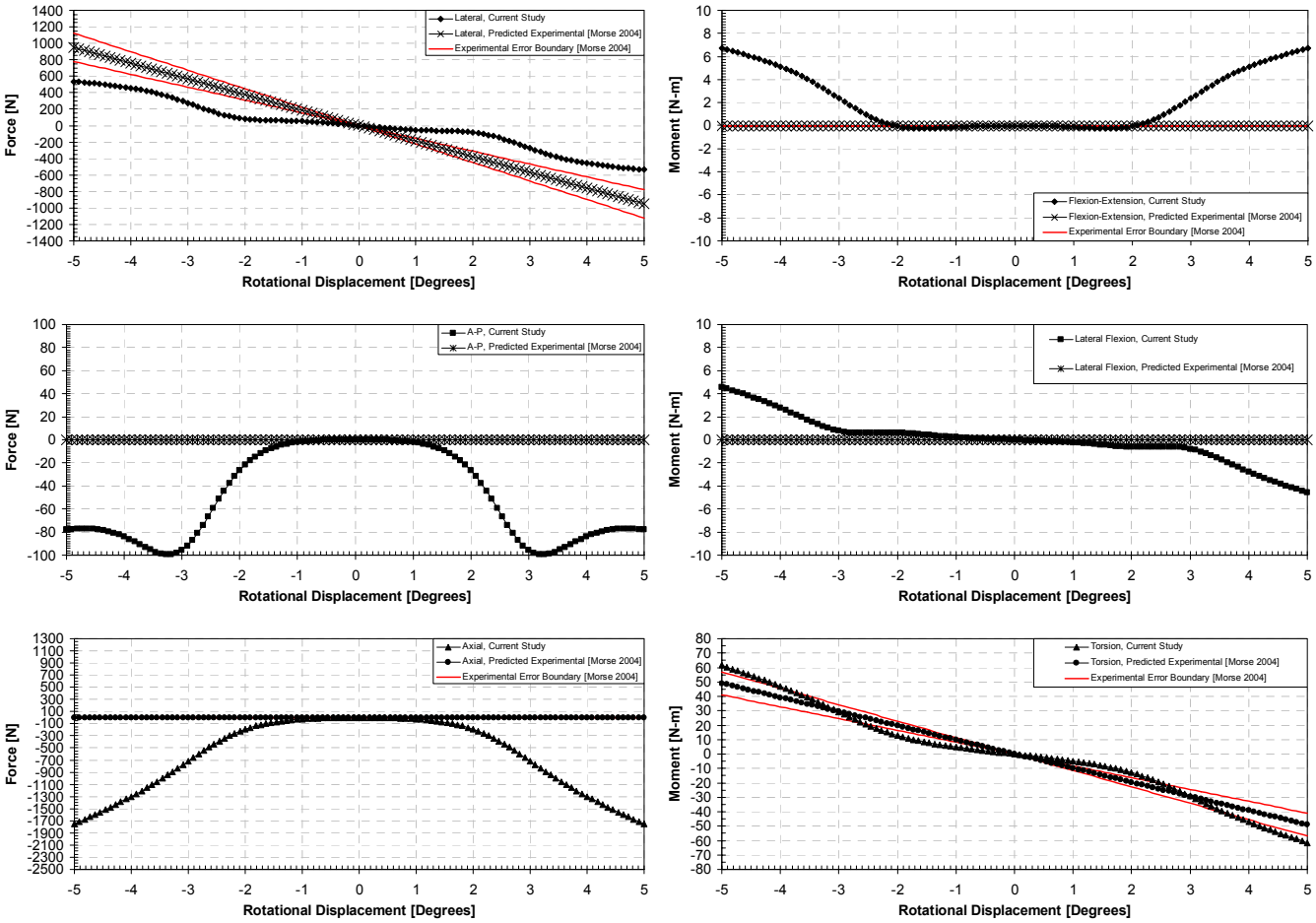

Figure B.2.29. Three-dimensional model's response to torsion under a preload displacement of 0 mm (Posture 1, L4-L5).

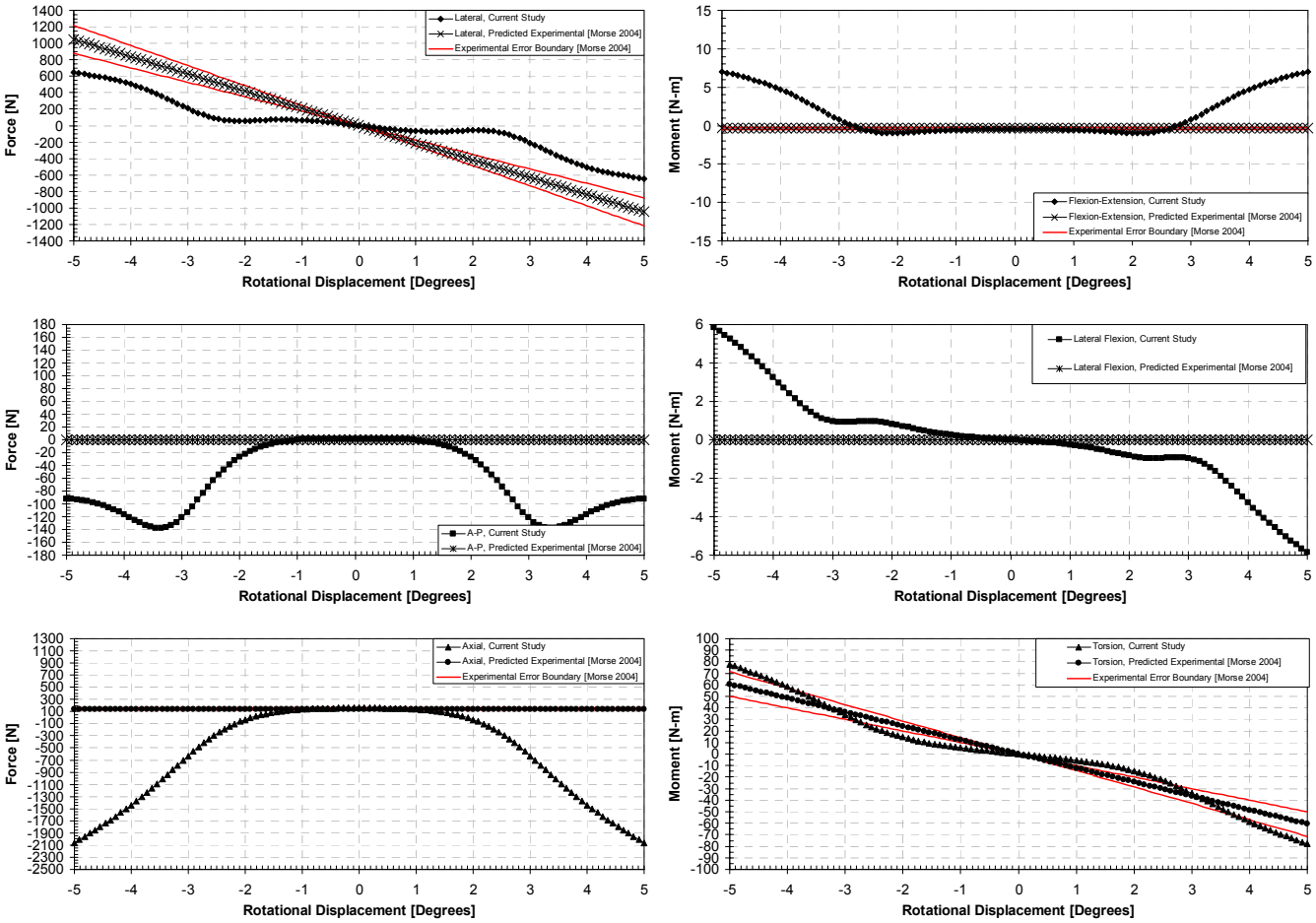

Figure B.2.30. Three-dimensional model's response to torsion under a preload displacement of 0.1033 mm (Posture 1, L4-L5).

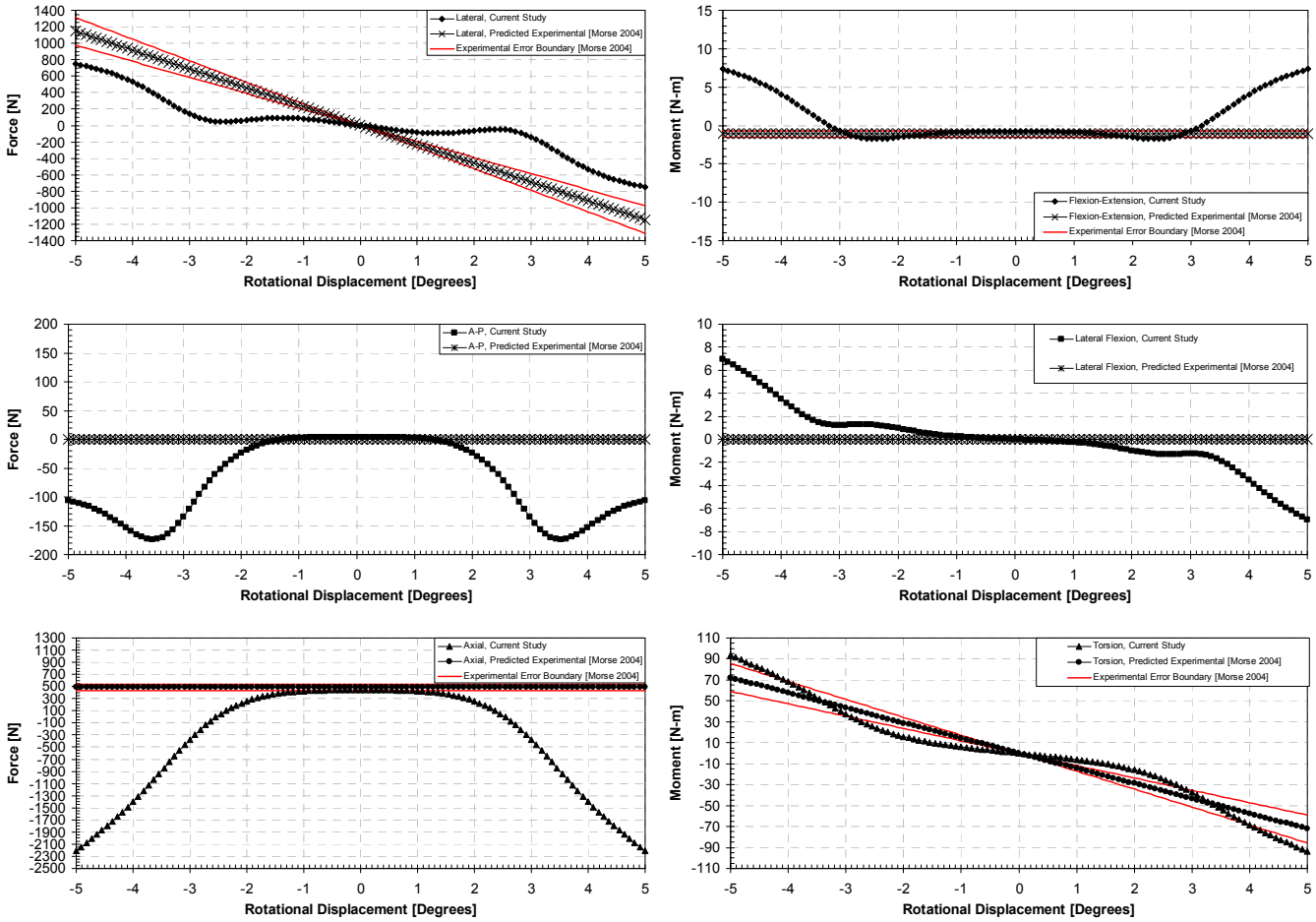

Figure B.2.31. Three-dimensional model's response to torsion under a preload displacement of 0.2066 mm (Posture 1, L4-L5).

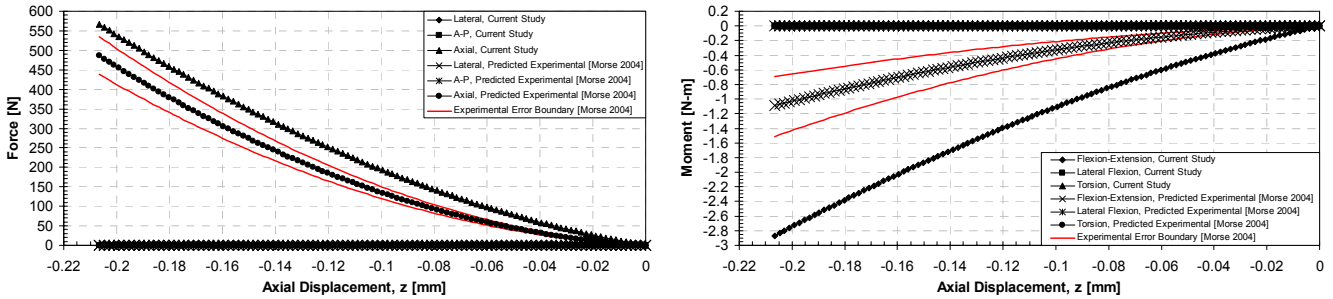

Figure B.2.32. Three-dimensional model's response to axial compression (Posture 2, L4-L5).

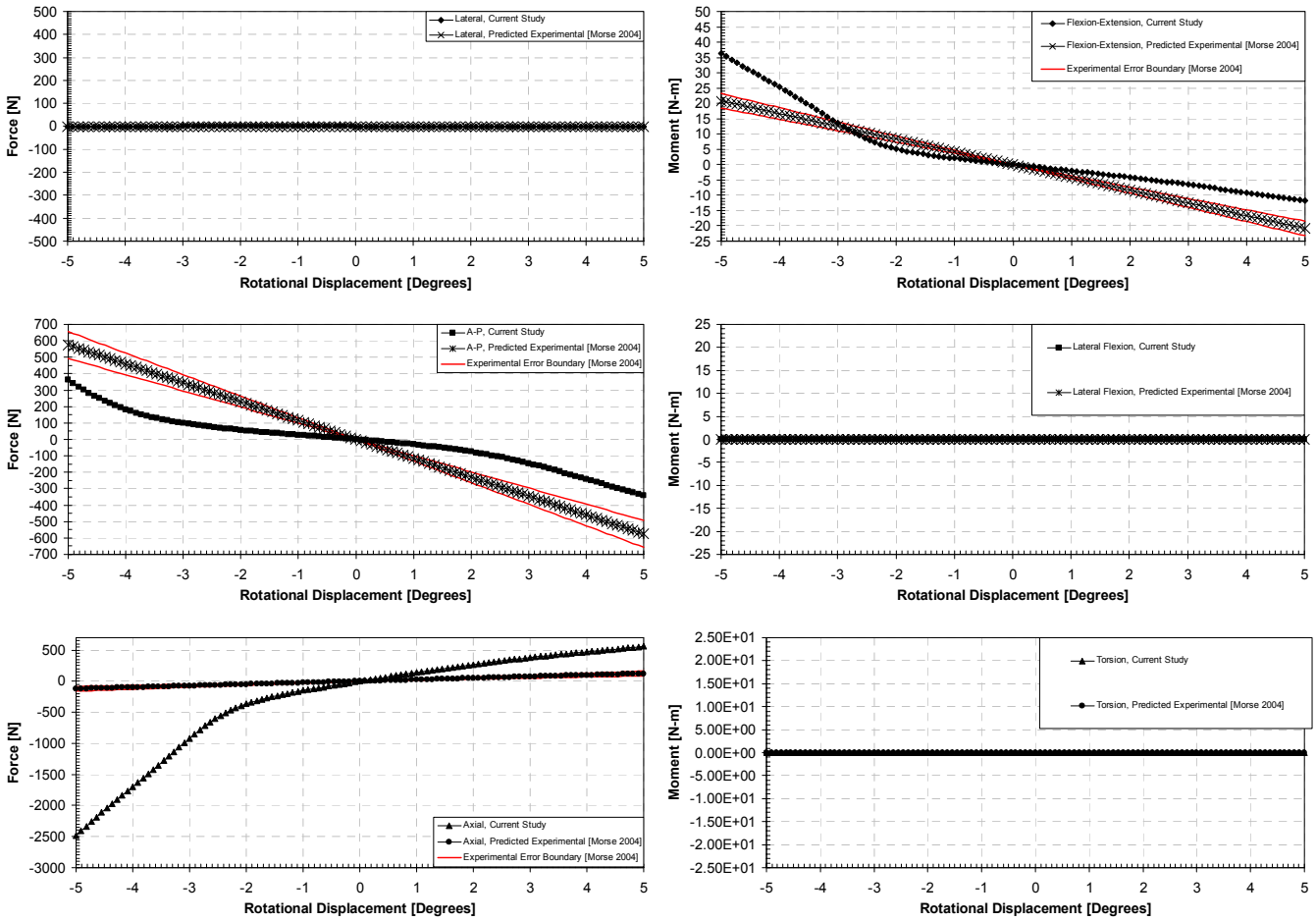

Figure B.2.33. Three-dimensional model's response to flexion/extension under a preload displacement of 0 mm (Posture 2, L4-L5).

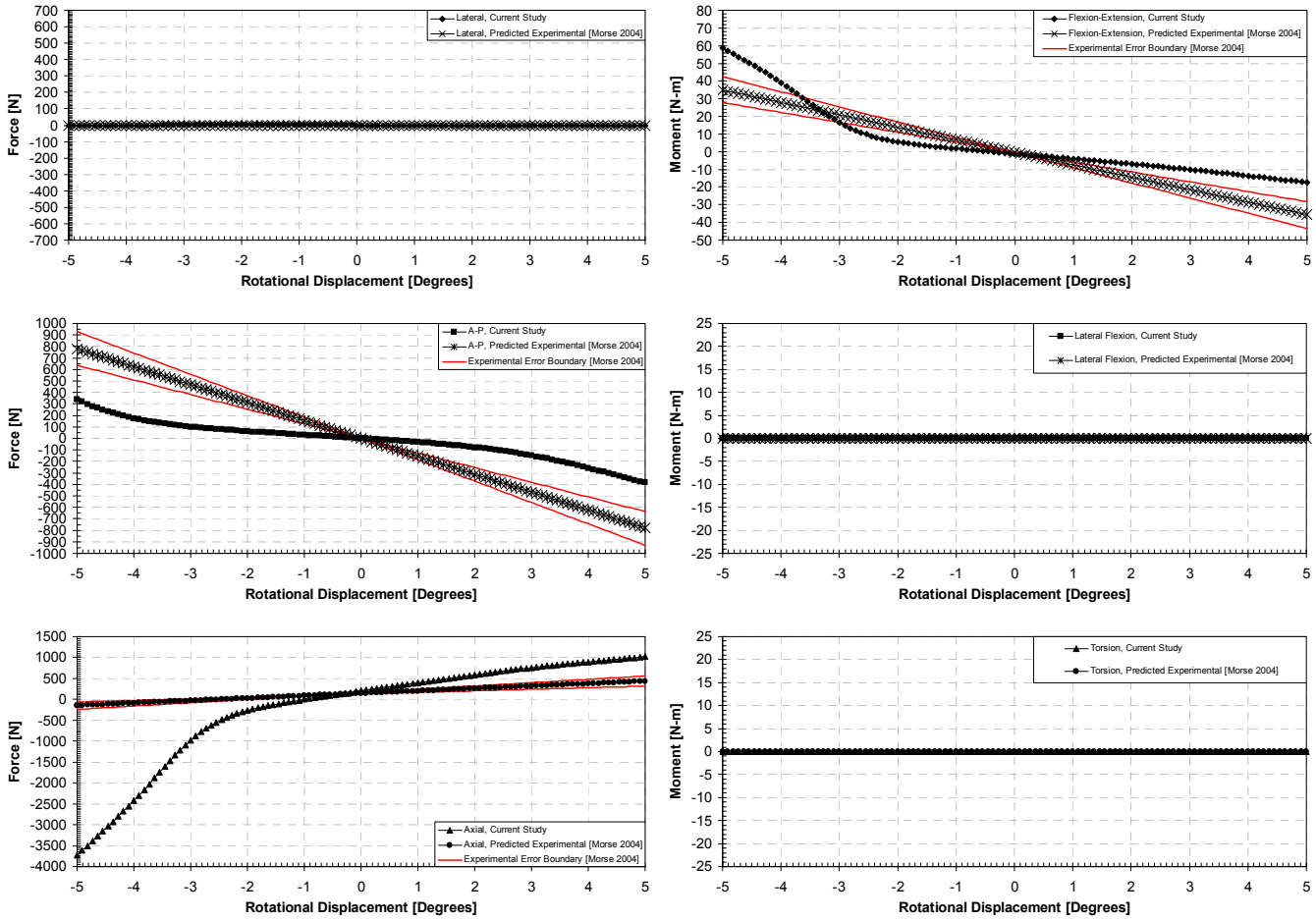

Figure B.2.34. Three-dimensional model's response to flexion/extension under a preload displacement of 0.1033 mm (Posture 2, L4-L5).

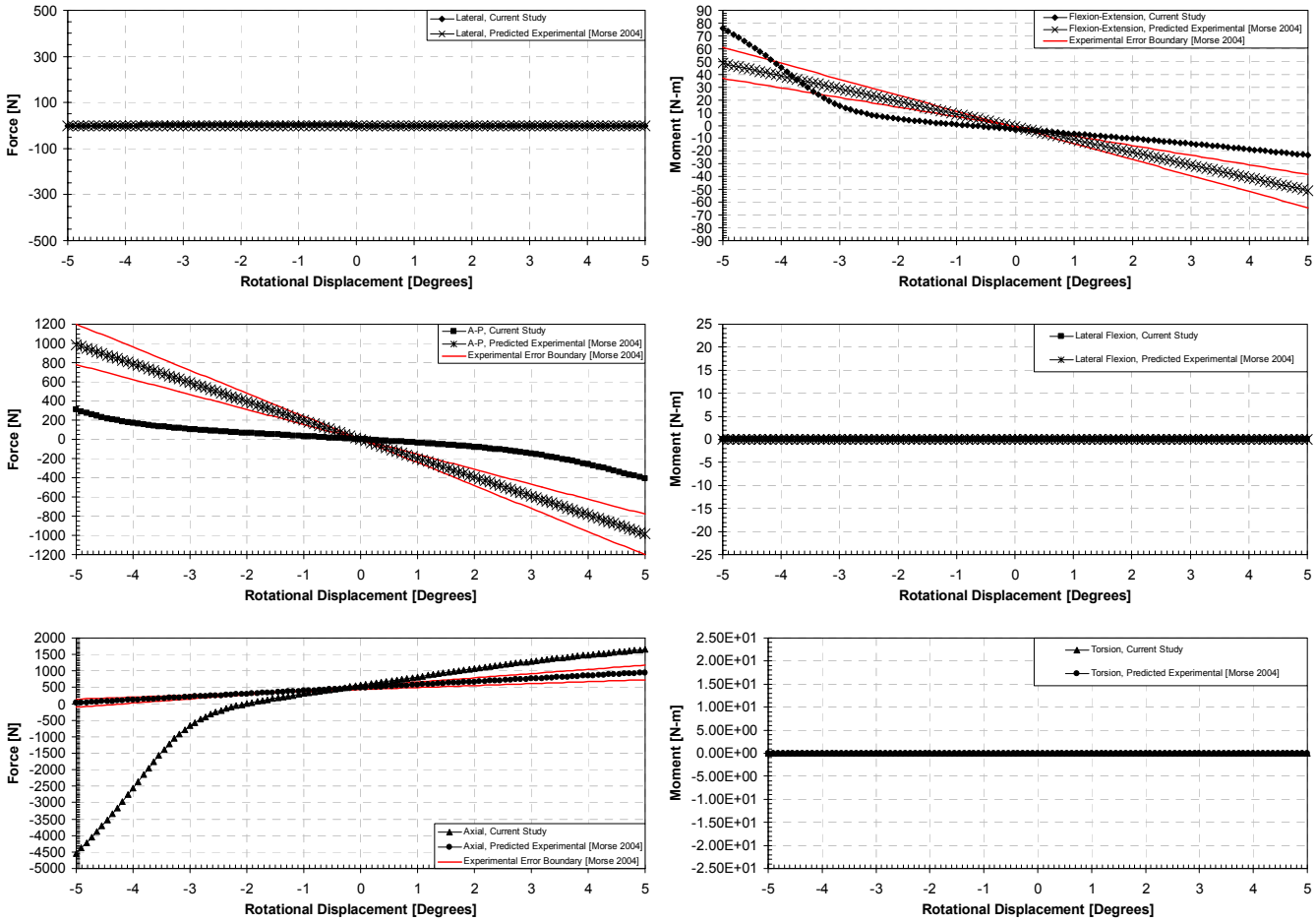

Figure B.2.35. Three-dimensional model's response to flexion/extension under a preload displacement of 0.2066 mm (Posture 2, L4-L5).

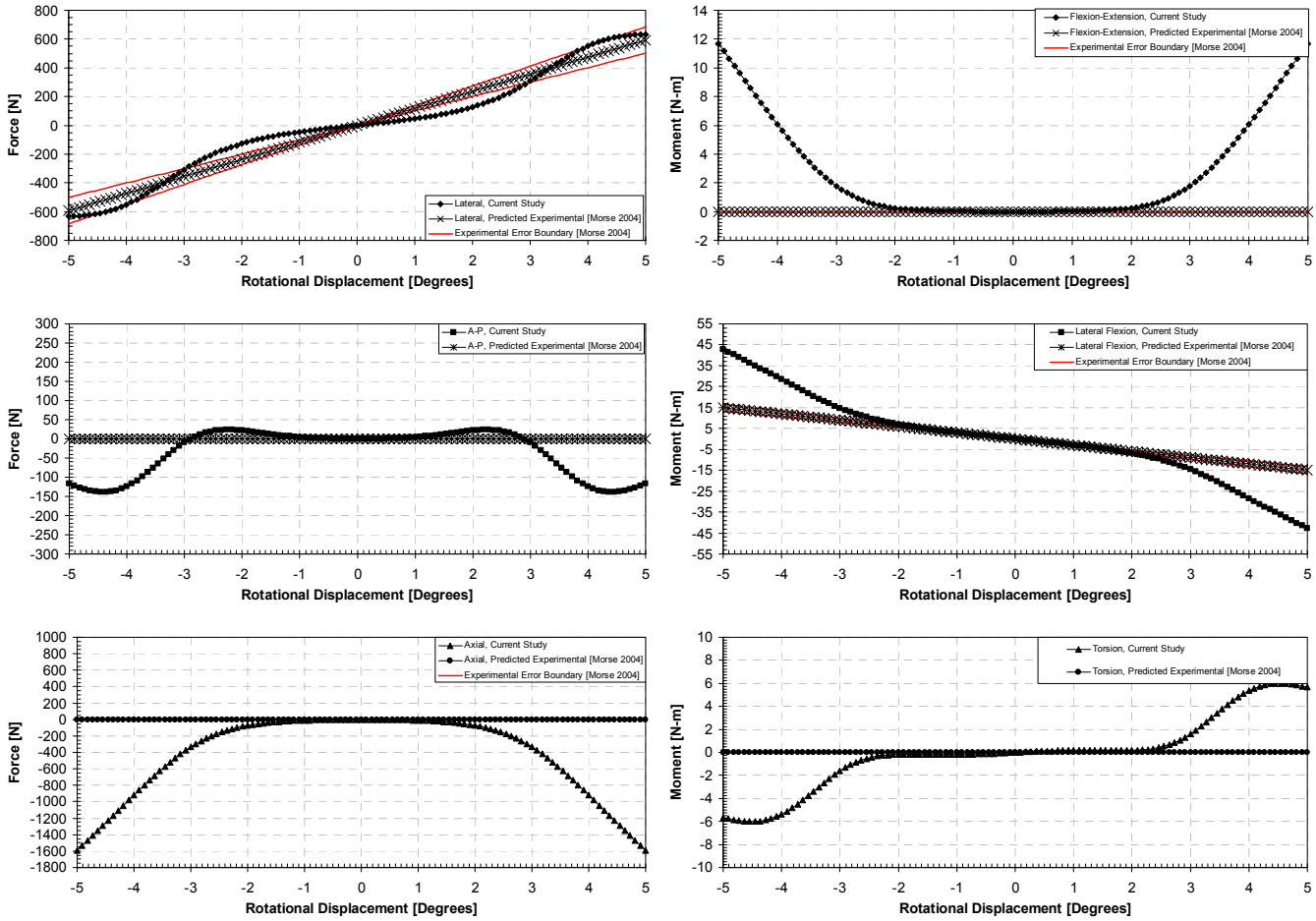

Figure B.2.36. Three-dimensional model's response to lateral flexion under a preload displacement of 0 mm (Posture 2, L4-L5).

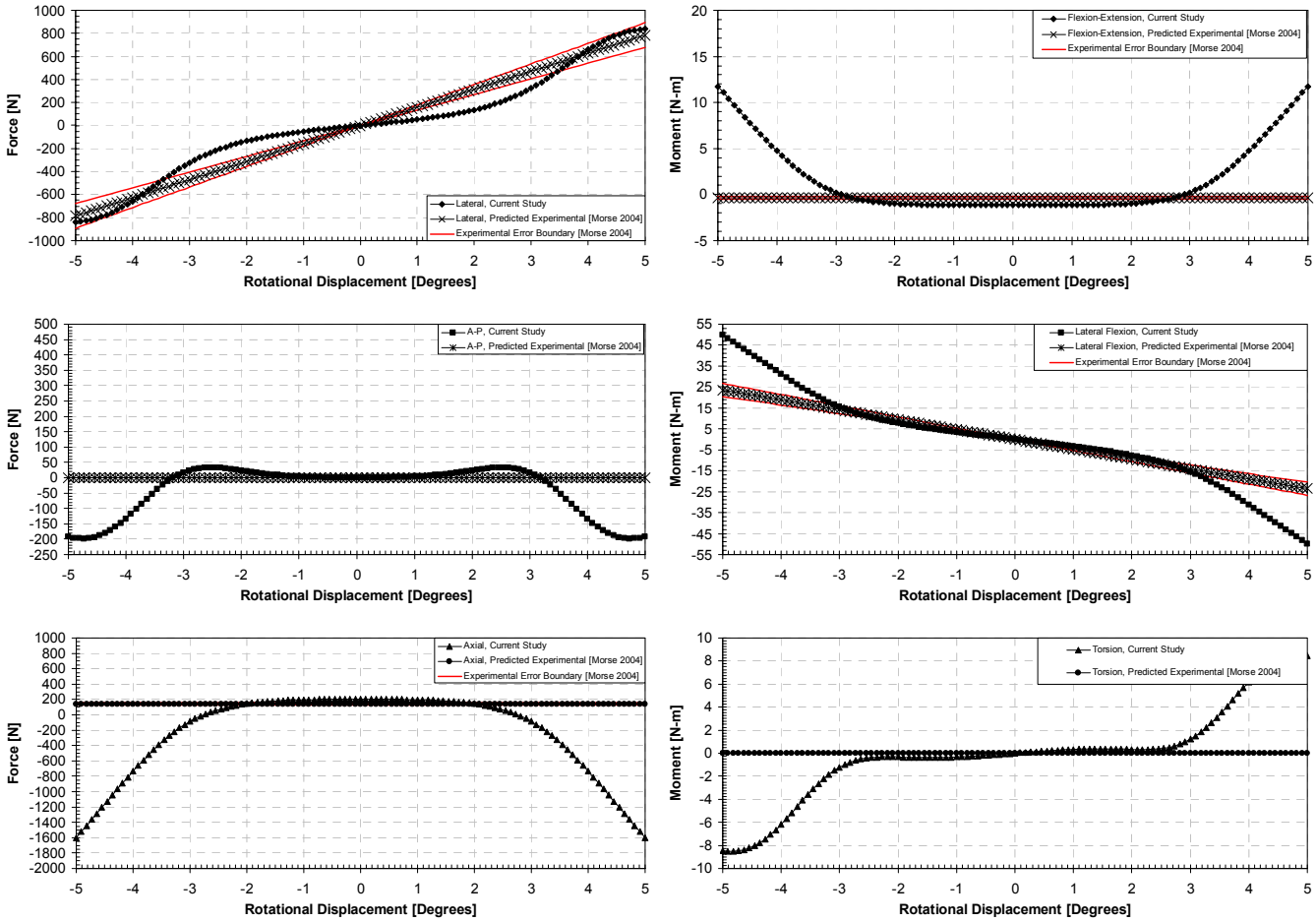

Figure B.2.37. Three-dimensional model's response to lateral flexion under a preload displacement of 0.1033 mm (Posture 2, L4-L5).

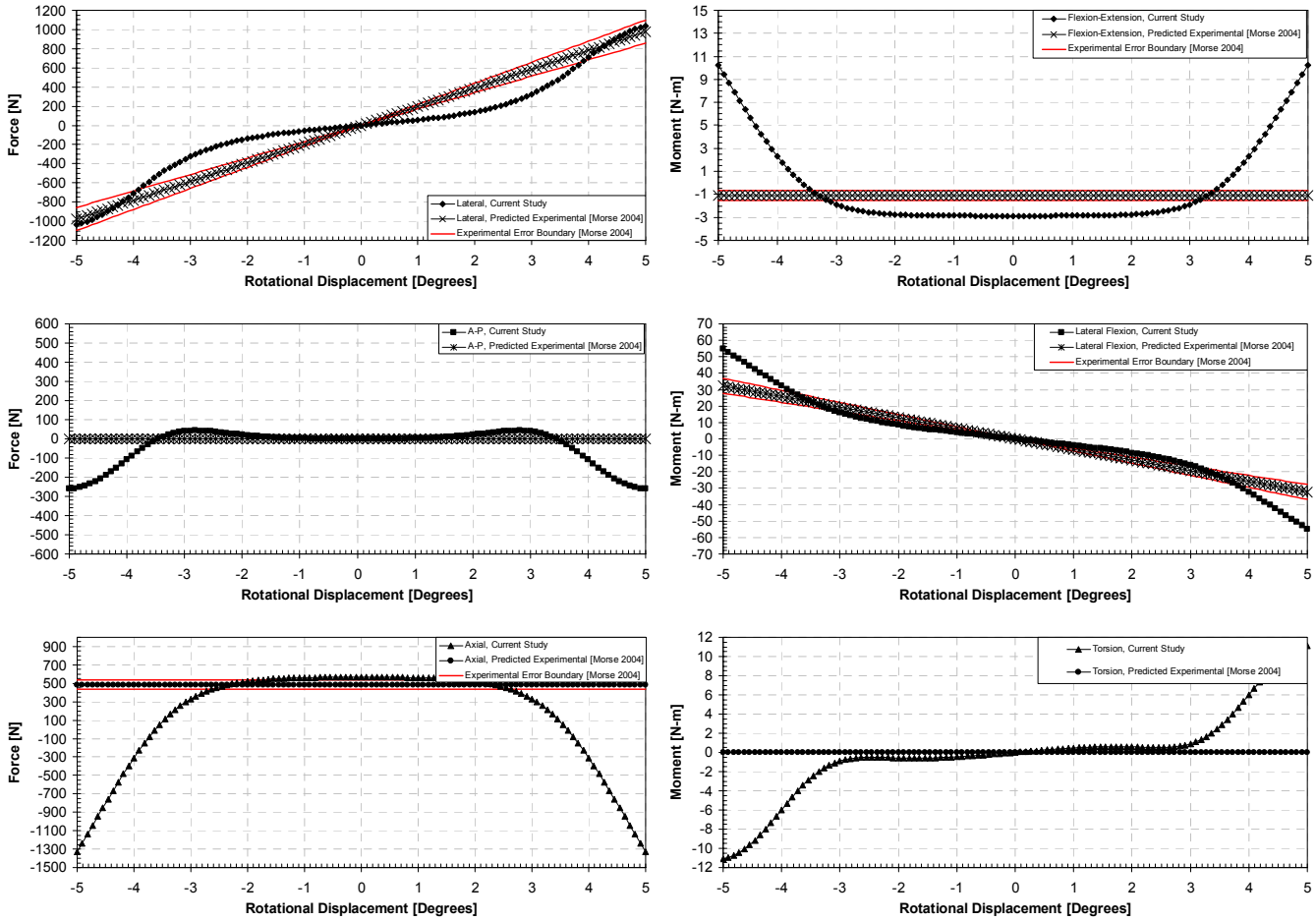

Figure B.2.38. Three-dimensional model's response to lateral flexion under a preload displacement of 0.2066 mm (Posture 2, L4-L5).

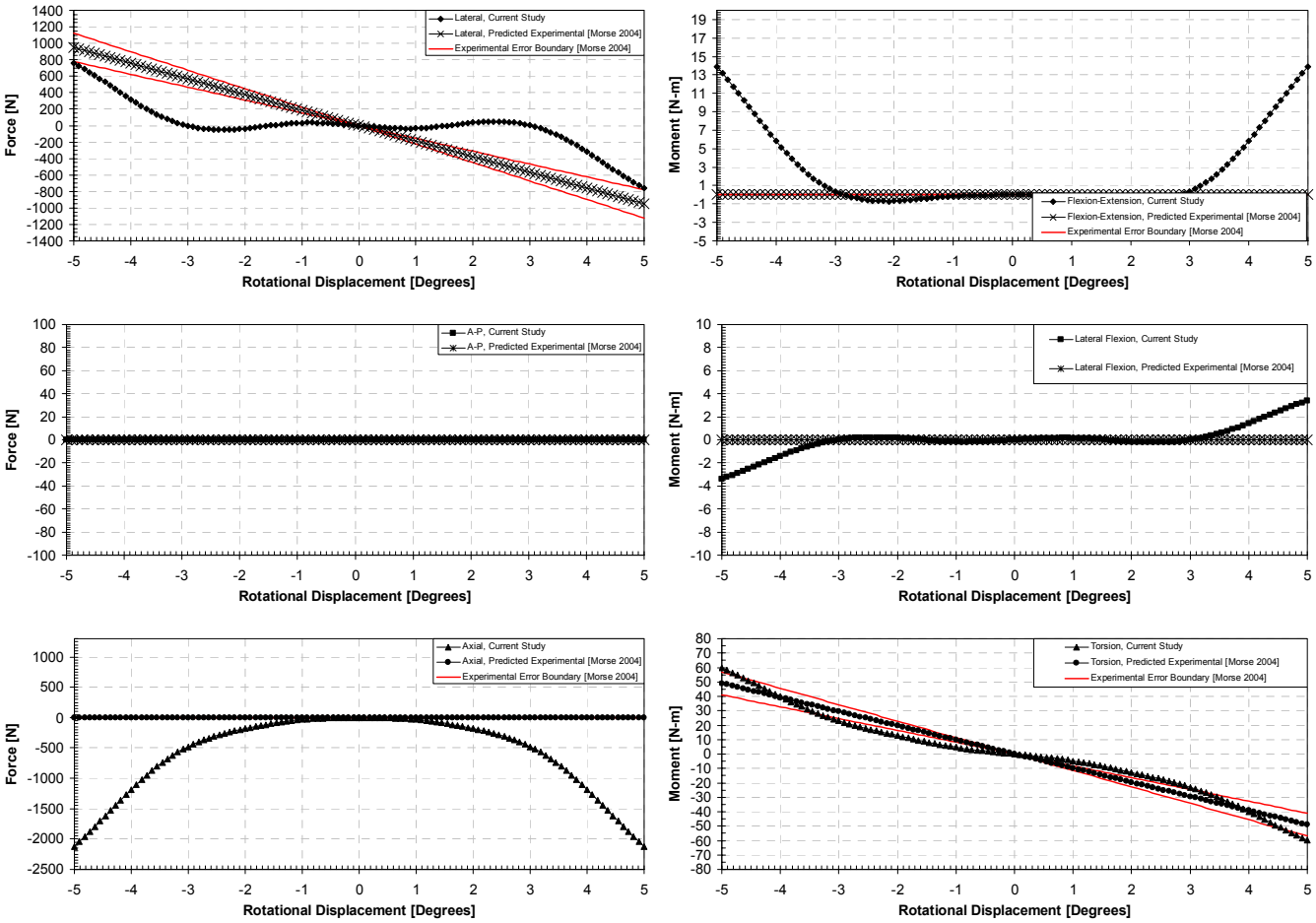

Figure B.2.39. Three-dimensional model's response to torsion under a preload displacement of 0 mm (Posture 2, L4-L5).

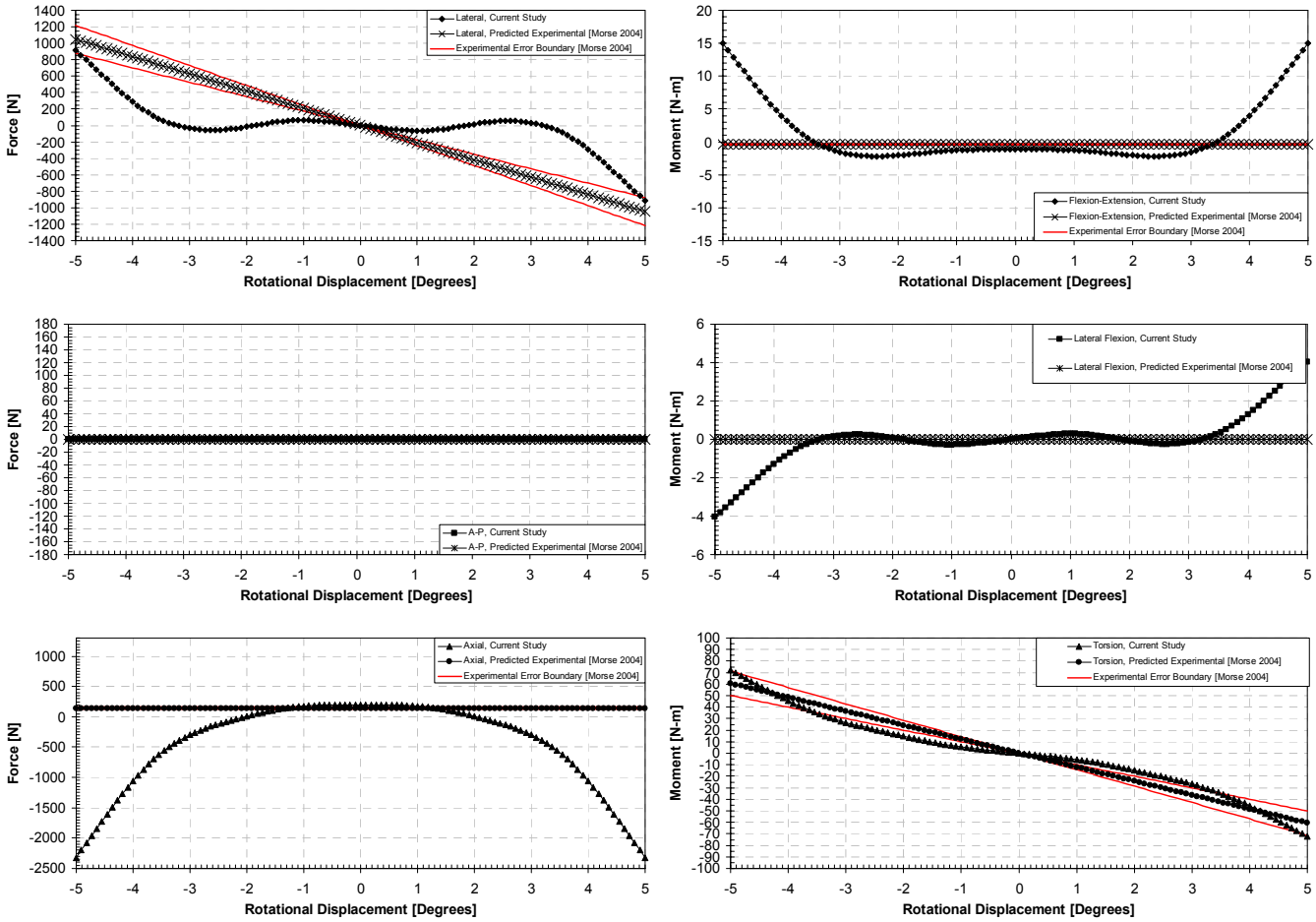

Figure B.2.40. Three-dimensional model's response to torsion under a preload displacement of 0.1033 mm (Posture 2, L4-L5).

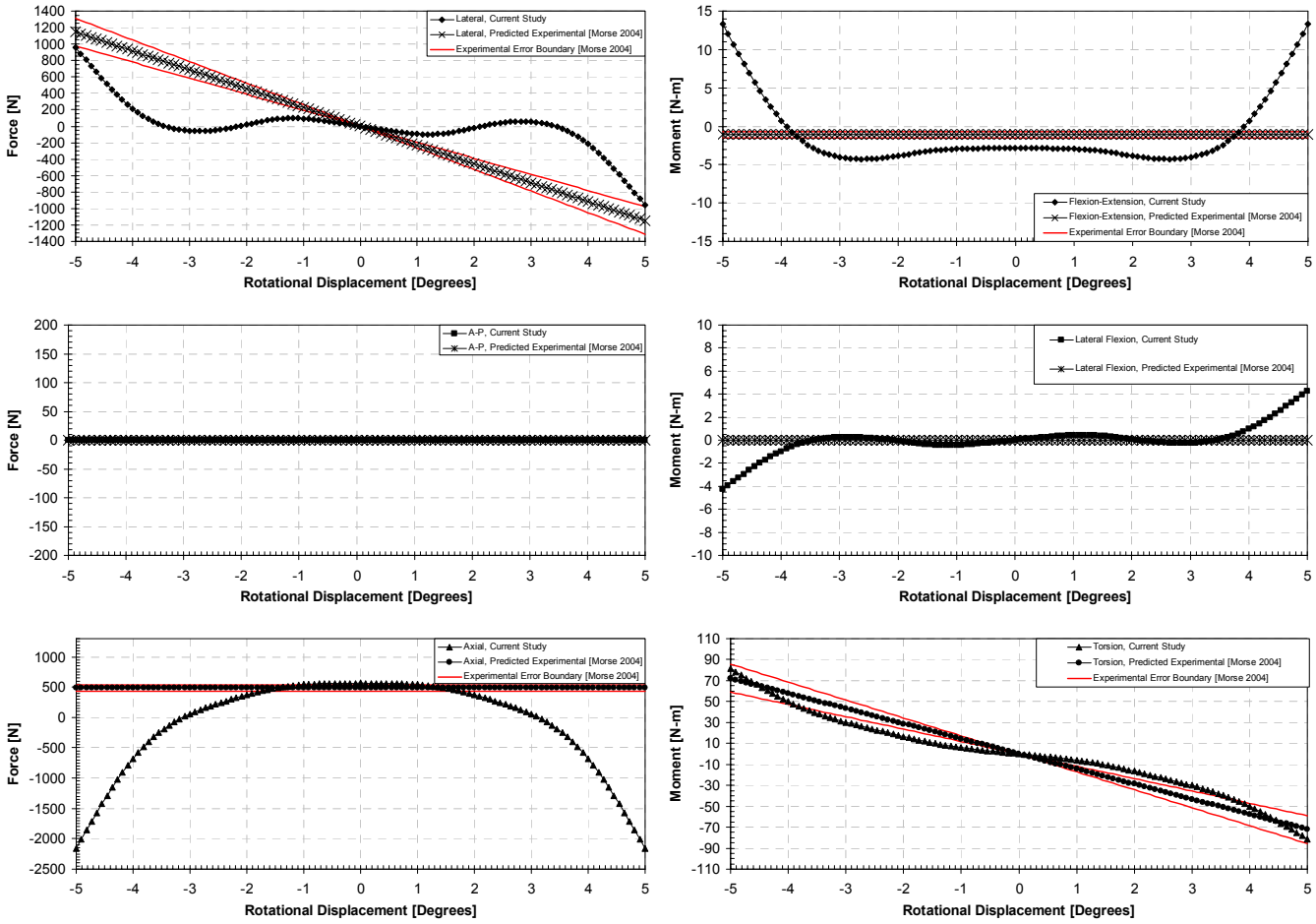

Figure B.2.41. Three-dimensional model's response to torsion under a preload displacement of 0.2066 mm (Posture 2, L4-L5).

Appendix C: Tables

Table C.1. Root mean square error over the physiologic range of motion (L4-L5).

Loading Condition	Preload Displacement [mm]	Root Mean Square (RMS) Error (L4-L5)					
		Lateral [N]		A-P [N]		Axial [N]	
		Posture 1	Posture 2	Posture 1	Posture 2	Posture 1	Posture 2
Axial Compression	0 - 0.2066	0	0	1.87	0	17.7	59.0
Extension/Flexion (±5°)	0	0.001	0	230	186	333	803
	0.1033	0.002	0	320	301	181	1158
	0.2066	0.002	0	424	419	147	1383
Lateral Flexion (±5°)	0	145	73.1	104	70.1	304	656
	0.1033	222	116	184	89.7	362	666
	0.2066	296	177	253	100	434	652
Torsion (±5°)	0	271	384	62.8	0	866	870
	0.1033	321	438	81.7	0	1052	936
	0.2066	373	505	98.9	0	1259	960
		Extension/Flexion [N-m]		Lateral Flexion [N-m]		Torsion [N-m]	
Axial Compression	0 - 0.2066	0.107	0.987	0	0	0	0
Extension/Flexion (±5°)	0	5.92	5.96	0	0	0	0
	0.1033	14.84	10.4	0	0	0	0
	0.2066	23.9	14.4	0	0	0	0
Lateral Flexion (±5°)	0	1.79	4.53	2.32	11.6	2.39	3.15
	0.1033	2.06	4.27	2.90	9.72	3.86	3.98
	0.2066	2.27	3.81	5.21	7.68	5.28	4.51
Torsion (±5°)	0	3.29	4.92	1.93	1.20	6.42	5.66
	0.1033	3.29	4.93	2.39	1.32	8.81	7.43
	0.2066	3.52	4.51	2.76	1.29	10.9	9.65

Table C.2. Root mean square error over the linear range of motion (L4-L5).

Loading Condition	Preload Displacement [mm]	Root Mean Square (RMS) Error (L4-L5)					
		Lateral [N]		A-P [N]		Axial [N]	
		Posture 1	Posture 2	Posture 1	Posture 2	Posture 1	Posture 2
Axial Compression	0 - 0.2066	0	0	1.87	0	17.7	59.0
Extension/Flexion (±1°)	0	0	0	53.0	50.2	26.5	70.2
	0.1033	0	0	74.4	72.6	17.3	102
	0.2066	0	0	95.2	94.9	46.3	124
Lateral Flexion (±1.5°)	0	54.2	61.3	7.30	4.98	9.84	11.2
	0.1033	87.3	90.6	11.7	4.31	11.8	54.9
	0.2066	122	119	12.8	3.44	52.5	76.4
Torsion (±1°)	0	76.8	85.9	0.689	0	9.55	12.8
	0.1033	80.1	79.0	1.40	0	11.82	53.4
	0.2066	82.4	72.7	3.25	0	49.6	74.9
		Extension/Flexion [N-m]		Lateral Flexion [N-m]		Torsion [N-m]	
Axial Compression	0 - 0.2066	0.107	0.987	0	0	0	0
Extension/Flexion (±1°)	0	1.65	1.25	0	0	0	0
	0.1033	3.32	2.58	0	0	0	0
	0.2066	4.99	4.06	0	0	0	0
Lateral Flexion (±1.5°)	0	0.0134	.0264	0.910	0.068	0.265	0.164
	0.1033	0.0707	0.798	2.07	1.08	0.327	0.273
	0.2066	0.291	1.76	3.31	2.17	0.338	0.385
Torsion (±1°)	0	0.0457	0.0582	0.121	0.116	3.02	3.15
	0.1033	0.0991	0.840	0.129	0.192	3.97	4.11
	0.2066	0.274	1.79	0.134	0.270	4.96	5.06